

UNIVERSIDADE FEDERAL DO PARANÁ

LEANDRO JOSÉ LEMES STIVAL

**A STUDY ON WIND ASSESSMENT ON THE WIND POWER
PERFORMANCE: WIND SHEAR AND TURBULENCE INTENSITY
EFFECTS BESIDES THE WAKE MODELING FOR A SINGLE WIND
TURBINE**

CURITIBA
2017

LEANDRO JOSÉ LEMES STIVAL
2017

LEANDRO JOSE LEMES STIVAL

**A STUDY ON WIND ASSESSMENT ON THE WIND POWER
PERFORMANCE: WIND SHEAR AND TURBULENCE INTENSITY EFFECTS
BESIDES THE WAKE MODELING FOR A SINGLE WIND TURBINE**

Master's Dissertation presented for the Final
Exam to the Graduate Program on Water
Resources and Environmental Engineering
of Federal University of Paraná.

Advisor: Prof. Dr. Alexandre Kolodynskie
Guetter

Co-advisor: Prof. Dr. Fernando Oliveira
Andrade

CURITIBA

2017

ST862s

Stival, Leandro Jose Lemes

A study on wind assessment on the wind power performance: wind shear and turbulence intensity effects besides the Wake modeling for a single wind turbine / Leandro Jose Lemes Stival. – Curitiba, 2017.

118 f. : il. color. ; 30 cm.

Dissertação - Universidade Federal do Paraná, Setor de Tecnologia, Programa de Pós-Graduação em Engenharia de Recursos Hídricos e Ambiental, 2017.

Orientador: Alexandre Kolodynskie Guetter.

Coorientador: Fernando Oliveira Andrade.

1. Força do vento. 2. Modelo de Wake. 3. Energia eólica. I. Universidade Federal do Paraná. II. Guetter, Alexandre Kolodynskie. III. Andrade, Fernando Oliveira. IV. Título.

CDD: 621.312136

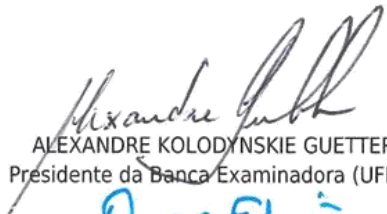



MINISTÉRIO DA EDUCAÇÃO
UNIVERSIDADE FEDERAL DO PARANÁ
PRÓ-REITORIA DE PESQUISA E PÓS-GRADUAÇÃO
Setor TECNOLOGIA
Programa de Pós Graduação em ENGENHARIA DE RECURSOS HÍDRICOS E AMBIENTAL
Código CAPES: 40001016021P0

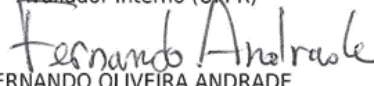
TERMO DE APROVAÇÃO

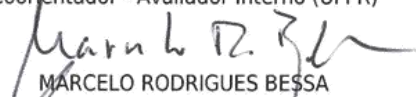
Os membros da Banca Examinadora designada pelo Colegiado do Programa de Pós-Graduação em ENGENHARIA DE RECURSOS HÍDRICOS E AMBIENTAL da Universidade Federal do Paraná foram convocados para realizar a arguição da Dissertação de Mestrado de **LEANDRO JOSÉ LEMES STIVAL**, intitulada: "**A study on Wind assessment on the Wind Power performance**", após terem inquirido o aluno e realizado a avaliação do trabalho, são de parecer pela sua APROVAÇÃO.

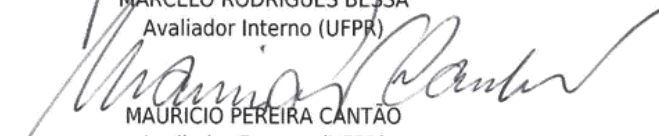
Curitiba, 04 de Abril de 2017.

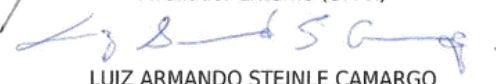

ALEXANDRE KOLODYNISKIE GUETTER
Presidente da Banca Examinadora (UFPR)


ANDRE LUIZ TONSO FABIANI
Avaliador Interno (UFPR)


FERNANDO OLIVEIRA ANDRADE
Coordenador - Avaliador Interno (UFPR)


MARCELO RODRIGUES BESSA
Avaliador Interno (UFPR)


MAURICIO PEREIRA CANTÃO
Avaliador Externo (UFPR)


LUIZ ARMANDO STEINLE CAMARGO
Avaliador Externo (UFPR)

ACKNOWLEDGEMENT

I would first like to express my very profound gratitude to my parents, Luci Lemes and José Stival, also to my partner, Luana Pádua, for providing me with inexhaustible assistance and continuous encouragement during a couple of years of researching and writing this thesis. This accomplishment would not have been possible without them.

I must declare my genuine appreciation to Alexandre K. Guetter, my thesis advisor from Federal University of Paraná, also to Fernando O. Andrade, my co-advisor from Federal University of Technology - Paraná. The gates to Prof. Guetter and Prof. Andrade offices were always open whenever I ran into a volatile situation or had a doubt about my research or writing. They regularly supported this thesis where I had to control the research as my particular aspiration, however guide me in the right the direction whenever he thought I needed it.

I would also like to extend a special thanks to the experts who were interested in the development of this research project: Gareth Brown, Aaron Culver and the whole SgurrEnergy team from Vancouver. Without Sgurr's comprehension to trust and assist the research with data, the survey could not have been successfully validated.

I would also like to acknowledge Prof. Maria Cristina Borba Braga for elucidating me on intellectual formulations, also to Prof. Eloy Kaviski for helping to clarify my codes, both from Federal University of Paraná. Beyond that, the board examination deserves a special acknowledge, composed by Prof. Marcelo Bessa, Prof. André Fabiani, Prof. Maurício Cantão, all from Federal University of Paraná and Doctor Luiz Steinle from BBB Energias Renováveis Ltda.

Finally, a very serious thanks to the Post-Graduate Program on Water Resources and Environmental Engineering at Federal University of Paraná, coordinated by Prof. Cristovão Fernandes and Prof. Tobias Bleninger, by providing me all I need inside the University, also to the Coordenação de Aperfeiçoamento de Pessoal de Nivel Superior, CAPES, for the scholarship during the whole process.

Thank you all.

RESUMO

A energia eólica cresceu significativamente, porém a eficiência de geração da fonte eólica gira em torno de 30% da energia cinética disponível no vento. Por este motivo é de extrema importância que estudos sejam elaborados afim de aumentar a eficiência na geração de energia. Este estudo visa investigar o desempenho da geração de energia eólica em dois parques eólicos situados na América do Norte, através da investigação dos dados de vento e modelagem da esteira turbulenta. Os dados analisados são provenientes da turbina, SCADA, e dados coletados pelo LiDAR. A partir das análises dos dados de vento foram estimados parâmetros como tensão de cisalhamento do vento, rosa dos ventos, perfil de velocidade do vento e intensidade de turbulência. Portanto, aumentando a intensidade de turbulência, a energia gerada é superestimada em moderadas velocidades do vento e subestimada em altas velocidades do vento. Enquanto isso, os coeficientes de cisalhamento do vento variaram entre 0 e 0.2 para altas velocidades. Além disso, coeficientes de cisalhamento com valores elevados, perto de 0.4, foram encontrados em baixas velocidades do vento. Este trabalho visou também comparar modelos de esteira turbulenta de PARK (Jensen), Frandsen, Larsen and Eddy Viscosity (Ainslie) com resultados obtidos pelo LiDAR, além disso foi realizado uma simulação numérica da esteira turbulenta utilizando Fluent CFD com as equações médias de Reynolds (RANS) que resolvem o modelos de duas equações diferenciais para obter a viscosidade turbulenta. A turbulência foi fechada pelo modelo $k - \varepsilon$, sendo o modelo de esteira turbulenta desenvolvido para uma única turbina num terreno plano. O modelo de PARK obteve os melhores resultados para linha de centro longitudinal em relação as velocidades de 6 a 8 ms^{-1} . Entretanto, para velocidade de 9 a 12 ms^{-1} , o modelo de EDDY VISCOSITY apresentou o melhor desempenho. As análises de seção transversal apresentaram o modelo de PARK como melhor resultado para 500 m. Enquanto isso, para 700 m de seção transversal, o melhor desempenho foi obtido pelo modelo de LARSEN.

Palavras-chave: Energia Eólica, Modelo de Esteira Turbulenta, LiDAR, Análises do Vento.

ABSTRACT

Wind power has gained significant share in the global power production. However, the wind power output efficiency is only about 30% of the wind kinetic energy. Because of that, it is essential to study the efficiency of these power generation systems by assessing the effects that wind parameters and wakes will have on the whole system. Hence, a complete assessment of wind resources is crucial to retain full advantage of wind power. This study aims to investigate the efficiency of wind energy generation in two North American Wind Farms, through wind data investigation and wake modeling. The data analyzed are the SCADA data and the data collected by LiDAR measurements. The wind data analysis has estimated parameters as wind shear, wind rose, wind speed profile and turbulence intensity. Therefore increasing turbulence intensity the power output is overestimated at moderate wind speeds and underestimated at higher wind speeds. Meanwhile, the wind shear coefficients were found to vary between 0 and 0.2 at higher inflow velocities. High wind shear values, close to 0.4, were recorded for lower inflow velocities. The goal of the wake models is to simulate the turbine induced wind speed deficits and the ratio of restoration to the free stream velocity. This work has compared the PARK (Jensen), Frandsen, Larsen and Eddy Viscosity (Ainslie) models with LiDAR wake measurements, besides that it has performed a numerical simulation of the wind turbine wake using the Fluent CFD with the Reynolds Averaged Navier Stokes (RANS) equations that solves two differential equation model to obtain turbulent viscosity. The turbulence was closed by the $k - \varepsilon$ model, where the wake modeling has been developed for a single turbine on a flat terrain. In terms of centerline wake analysis, the PARK wake model yielded the best velocity simulations for inflow winds from 6 to 8 ms^{-1} . However, the EDDY VISCOSITY wake model yielded the best performance for wind speed bins from 9 to 12 ms^{-1} . The cross section wake analysis presented for the 500 m cross section, the domination by the PARK model. Meanwhile, along the 700 m cross section, the LARSEN wake model produced the best simulations.

Key-words: Wind Power, Wake Modeling, LiDAR, Wind Analysis.

LIST OF FIGURES

FIGURE 1: STREAM TUBE POSITIONS WHEN USING BETZ ANALOGY.....	7
FIGURE 2: DERIVING WIND SPEED FROM DOPPLER SHIFTS OBSERVED BY LIDAR.....	12
FIGURE 3: JENSEN WAKE MODEL	19
FIGURE 4: GALION LIDAR USED IN SITES A AND B	27
FIGURE 5: LIDAR SCAN GEOMETRY OF 5 BEAMS ON SITE A	28
FIGURE 6: GALION POSITIONING IN THE WTG FOR PPI SCAN	29
FIGURE 7: SITE B GALION PPI SCAN OF 29 BEAMS.....	30
FIGURE 8: FLOWCHART OF METHODOLOGIES FOR SITE A AND B	30
FIGURE 9: SCHEMATIC VIEW OF THE PARK MODEL WAKE EXPANSION	35
FIGURE 10: WIND VELOCITY DISTRIBUTION AT SITE A.....	43
FIGURE 11: WIND ROSE FOR SITE A	43
FIGURE 12: POWER CURVE SCATTER PLOTS FOR WIND SHEAR RANGES	45
FIGURE 13: WIND SPEED HISTOGRAM CONDITIONED ON WIND SHEAR COEFFICIENTS .	46
FIGURE 14: POWER CURVE CONDITIONED ON WIND SHEAR COEFFICIENTS.....	47
FIGURE 15: VARIABILITY OF POWER CURVES WITH RESPECT TO TURBULENCE INTENSITY (TI)	48
FIGURE 16: WIND SPEED HISTOGRAM CONDITIONED ON TURBULENCE INTENSITY	49
FIGURE 17: POWER CURVES CONDITIONED ON TURBULENCE INTENSITY (TI)	50
FIGURE 18: WIND SPEED HISTOGRAM AND FITTED WEIBULL DISTRIBUTION FOR SITE B	52
FIGURE 19: WIND ROSE FOR THE METEOROLOGICAL MAST DATA OF SITE B.....	53
FIGURE 20: LIDAR CENTERLINE VELOCITY RECOVERY FOR 5 TO 12 MS ⁻¹ FREESTREAM BINS	54
FIGURE 21: LIDAR 500 M CROSS SECTION VELOCITY RECOVERY FOR 5 TO 12 MS ⁻¹ FREESTREAM BINS	56

FIGURE 22: LIDAR 700 M CROSS SECTION VELOCITY RECOVERY FOR 5 TO 12 MS ⁻¹	
FREESTREAM BINS	57
FIGURE 23: LIDAR 1000 M CROSS SECTION VELOCITY RECOVERY FOR 5 TO 12 MS ⁻¹	
FREESTREAM BINS	58
FIGURE 24: MESH FOR CFD WAKE SIMULATION.....	60
FIGURE 25: 5 MS ⁻¹ VELOCITY RECOVERY ALONG THE WAKE CENTERLINE	64
FIGURE 26: 5 MS ⁻¹ VELOCITY RECOVERY ALONG THE WAKE CROSS SECTIONS.....	66
FIGURE 27: 6 MS ⁻¹ VELOCITY RECOVERY ALONG THE WAKE CENTERLINE	67
FIGURE 28: 6 MS ⁻¹ VELOCITY RECOVERY ALONG THE WAKE CROSS SECTIONS.....	69
FIGURE 29: 7 MS ⁻¹ VELOCITY RECOVERY ALONG THE WAKE CENTERLINE	70
FIGURE 30: 7 MS ⁻¹ VELOCITY RECOVERY ALONG THE WAKE CROSS SECTIONS.....	72
FIGURE 31: 8 MS ⁻¹ VELOCITY RECOVERY ALONG THE WAKE CENTERLINE	73
FIGURE 32: 8 MS ⁻¹ VELOCITY RECOVERY ALONG THE WAKE CROSS SECTIONS.....	74
FIGURE 33: 9 MS ⁻¹ VELOCITY RECOVERY ALONG THE WAKE CENTERLINE	75
FIGURE 34: 9 MS ⁻¹ VELOCITY RECOVERY ALONG THE WAKE CROSS SECTIONS.....	77
FIGURE 35: 10 MS ⁻¹ VELOCITY RECOVERY ALONG THE WAKE CENTERLINE	78
FIGURE 36: 10 MS ⁻¹ VELOCITY RECOVERY ALONG THE WAKE CROSS SECTIONS.....	79
FIGURE 37: 11 MS ⁻¹ VELOCITY RECOVERY ALONG THE WAKE CENTERLINE	81
FIGURE 38: 11 MS ⁻¹ VELOCITY RECOVERY ALONG THE WAKE CROSS SECTIONS.....	82
FIGURE 39: 12 MS ⁻¹ VELOCITY RECOVERY ALONG THE WAKE CENTERLINE	83
FIGURE 40: 12 MS ⁻¹ VELOCITY RECOVERY ALONG THE WAKE CROSS SECTIONS.....	84

LIST OF TABLES

TABLE 1: MEAN WIND AND METEOROLOGICAL PARAMETERS AT SITE A.....	42
TABLE 2: WIND SHEAR RANGES FOR SITE A	44
TABLE 3: TURBULENCE INTENSITY STATISTICS	49
TABLE 4: METEOROLOGICAL MAST VARIABLES	51
TABLE 5: PARAMETERS OF THE SIMPLIFIED MODELS	59
TABLE 6: PRESSURE DROP RELATED TO FREESTREAM VELOCITY	62
TABLE 7: SPONGE POROUS ZONE PARAMETERS.....	62
TABLE 8: ROOT MEAN SQUARE ERROR ALONG THE WAKE CENTERLINE	86
TABLE 9: RMSE ANALYSIS ALONG THE CROSS SECTION, 500 M BEHIND THE TURBINE	87
TABLE 10: RMSE ANALYSIS ALONG THE CROSS SECTION, 700 M BEHIND THE TURBINE	87
TABLE 11: RMSE ANALYSIS ALONG THE CROSS SECTION, 1000 M BEHIND THE TURBINE	88

ACRONYMS

BEM	Betz's Blade Element
CFD	Computational Fluid Dynamics
GWEC	Global Wind Energy Council
LES	Large Eddy Simulation
LiDAR	Light Detection and Ranging
LOS	Line of Sight
LST	Least Squares Technique
RANS	Reynolds-averaged Navier-Stokes
RMSE	Root Mean Square Error
SCADA	Supervisory Control and Data Acquisition
SODAR	Sound Detection and Ranging
WTG	Wind Turbine Generator

SYMBOLS

T	Absolute temperature	K
ρ	Air density	kgm ⁻³
I_a	Ambient turbulence	%
ε_a	Ambient turbulence input	
TI	Ambient turbulence intensity	
A	Area	m ²
p_{atm}	Atmospheric pressure	Pa
θ	Azimuth angle	degree
f	Body force	N
u_c	Centerline velocity deficit	ms ⁻¹
l	Characteristic length	m
C_μ	Constant of k equation	
λ	Constant related to gas constant and specific heat	
x	Distance behind the turbine	m
s	Distance from the LiDAR ahead LOS	m
ε	Eddy viscosity	m ² s ⁻¹
D_e	Effective rotor diameter	m
φ	Elevation angle	degree
R_{nb}	Empirical expression related to the ambient turbulence	m
Ψ	Face permeability	m ²
ρ	Fluid density	kgm ⁻³
F	Function dependent of the downstream distance	
F_{st}	Function depending on stability	
z	Height	m
ω	Induction factor	
D_m	Initial velocity deficit	ms ⁻¹
E_c	Kinetic Energy	J
m	Mass	kg

\dot{m}	Mass flux	kg s^{-1}
S	Mean strain rate tensor	$\text{m}^2 \text{s}^{-3}$
U	Mean velocity vector	ms^{-1}
\bar{V}	Mean wind speed	ms^{-1}
p	Modified mean pressure	Pa
γ	Non dimensional parameter of the Frandsen Model	
c_1	Non-dimensional mixing length	
V_0	Non-waked wind speed	ms^{-1}
n	Number of bins	
PP	PARK wake model profile	
Δm	Porous medium thickness	m
T_p	Potential temperature	K
P	Power	W
C_p	Power coefficient	
p	Pressure	Pa
p_s	Pressure that would be at sea level	Pa
C_2	Pressure-jump coefficient	m^{-1}
r	Radial distance	m
v	Radial velocity	ms^{-1}
y_i	Real measured data	
Z_r	Reference height	m
V_r	Reference wind speed	ms^{-1}
x_0	Relative position of the WTG	m
$\overline{u'v'}$	Reynolds stress	$\text{m}^2 \text{s}^{-2}$
D	Rotor Diameter	m
τ	Specific Reynolds stress tensor	$\text{m}^2 \text{s}^{-2}$
σ	Standard deviation of wind speed	ms^{-1}
z_0	Surface roughness altitude	m
C_T	Thrust coefficient	
F_T	Thrust force	N
p_t	Total Pressure	Pa

ε_{dr}	Turbulence dissipation rate	m^2s^{-3}
I	Turbulence intensity	
K	Turbulence kinetic energy	J
v_t	Turbulence velocity	ms^{-1}
μ_t	Turbulent viscosity	m^2s^{-1}
d	Unit direction vector	
v	Velocity	ms^{-1}
κ	Von Karman constant	
A_w	Wake Area	m^2
k	Wake decay constant	
D_w	Wake Diameter	m
β	Wake expansion parameter	
l_w	Wake length	m
w_i	Wake model analyzed	
R_w	Wake radius	m
$R_{9.5}$	Wake Radius at 9.5 rotor diameters	m
b	Wake width	m
u	Waked wind speed	ms^{-1}
$F(u)$	Weibull cumulative distribution function	
$f(u)$	Weibull distribution function	sm^{-1}
c	Weibull scale parameter	
k	Weibull shape parameter	ms^{-1}
α	Wind shear coefficient	
u_x	Wind velocity deficit	ms^{-1}
E_c	Kinetic Energy	J
m	Mass	kg
V	Wind speed	ms^{-1}
P	Power	W
ρ	Air density	kgm^{-3}
A	Area	m^2
\dot{m}	Mass flux	kgs^{-1}
F_T	Thrust force	N

ω	Induction factor	
p	Pressure	Pa
p_t	Total Pressure	Pa
p_{atm}	Atmospheric pressure	Pa
v	Velocity	ms ⁻¹
C_p	Power coefficient	
z	Height	m
z_0	Surface roughness altitude	m
F_{st}	Function depending on stability	
Z_r	Reference height	m
V_r	Reference wind speed	ms ⁻¹
α	Wind shear coefficient	
I	Turbulence intensity	
σ	Standard deviation of wind speed	ms ⁻¹
\bar{V}	Mean wind speed	ms ⁻¹
D	Rotor Diameter	m
D_w	Wake Diameter	m
V_0	Non-waked wind speed	ms ⁻¹
u	Waked wind speed	ms ⁻¹
k	Wake decay constant	
x	Distance behind the turbine	m
C_T	Thrust coefficient	
v	Radial velocity	ms ⁻¹
r	Radial distance	m
A_w	Wake Area	m ²
u_x	Wind velocity deficit	ms ⁻¹
$\overline{u'v'}$	Reynolds stress	m ² s ⁻²
U	Mean velocity vector	ms ⁻¹
p	Modified mean pressure	Pa
ρ	Fluid density	kgm ⁻³
f	Body force	N
τ	Specific Reynolds stress tensor	m ² s ⁻²

S	Mean strain rate tensor	m^2s^{-3}
v_t	Turbulence velocity	ms^{-1}
l_w	Wake length	m
ε_a	Ambient turbulence input	
D_m	Initial velocity deficit	ms^{-1}
TI	Ambient turbulence intensity	
PP	PARK wake model profile	
μ_t	Turbulent viscosity	m^2s^{-1}
l	Characteristic length	m
K	Turbulence kinetic energy	J
ε_{dr}	Turbulence dissipation rate	m^2s^{-3}
C_μ	Constant of k equation	
k	Weibull shape parameter	ms^{-1}
c	Weibull scale parameter	
$f(u)$	Weibull distribution function	sm^{-1}
$F(u)$	Weibull cumulative distribution function	
T_p	Potential temperature	K
T	Absolute temperature	K
p_s	Pressure that would be at sea level	Pa
λ	Constant related to gas constant and specific heat	
β	Wake expansion parameter	
γ	Non dimensional parameter of the Frandsen Model	
R_w	Wake radius	m
c_1	Non-dimensional mixing length	
x_0	Relative position of the WTG	m
D_e	Effective rotor diameter	m
$R_{9.5}$	Wake Radius at 9.5 rotor diameters	m
R_{nb}	Empirical expression related to the ambient turbulence	m
I_a	Ambient turbulence	%

b	Wake width	m
u_c	Centerline velocity deficit	ms ⁻¹
κ	Von Karman constant	
F	Function dependent of the downstream distance	
ε	Eddy viscosity	m ² s ⁻¹
y_i	Real measured data	
w_i	Wake model analyzed	
n	Number of bins	
C_2	Pressure-jump coefficient	m ⁻¹
Ψ	Face permeability	m ²
Δm	Porous medium thickness	m
s	Distance from the LiDAR ahead LOS	m
d	Unit direction vector	
φ	Elevation angle	degree
θ	Azimuth angle	degree

SUMMARY

ACKNOWLEDGEMENT	V
RESUMO.....	VI
ABSTRACT.....	VII
LIST OF FIGURES.....	VIII
LIST OF TABLES	X
ACRONYMS	XI
SYMBOLS.....	XII
1 INTRODUCTION.....	1
1.1 JUSTIFICATION	3
1.2 OBJECTIVE	4
1.3 GOALS	4
1.4 MASTER THESIS CHAPTERS	4
2 REVIEW.....	6
2.1 PHYSICAL ASPECTS.....	6
2.1.1 THE ACTUATOR DISC CONCEPT	7
2.2 WIND ASSESSMENT	9
2.2.1 WIND MEASUREMENT AND LIDAR.....	10
2.2.2 ATMOSPHERIC BOUNDARY LAYER	12
2.2.3 STABILITY	13
2.2.4 WIND SHEAR	14
2.2.5 TURBULENCE	15
2.2.6 POWER PERFORMANCE ANALYSIS	16
2.3 WAKE MODELS	17
2.3.1 SIMPLIFIED MODELS	18
2.3.1.1 PARK (JENSEN) MODEL	19
2.3.1.2 FRANDSEN WAKE MODEL	21
2.3.1.3 LARSEN WAKE MODEL.....	22
2.3.1.4 EDDY VISCOSITY WAKE MODEL	22

2.3.2	NUMERICAL SIMULATION (CFD).....	24
3	CASE STUDY	27
3.1	STUDY AREA	27
3.2	DATA	27
3.3	FLOWCHART OF METHODOLOGIES APPLIED IN SITE A AND B	30
4	METHODOLOGY.....	31
4.1	DATA QUALITY CONTROL.....	31
4.2	WIND ROSE	31
4.3	WIND SPEED DISTRIBUTION	32
4.4	WIND ANALYSIS PARAMETERS FOR SITE A	33
4.4.1	WIND SHEAR	33
4.4.2	TURBULENCE INTENSITY	33
4.4.3	POWER PERFORMANCE	34
4.5	MODELING FOR SITE B	34
4.5.1	PARK WAKE MODEL	35
4.5.2	FRANSEN WAKE MODEL	36
4.5.3	LARSEN WAKE MODEL.....	37
4.5.4	EDDY VISCOSITY WAKE MODEL.....	38
4.5.5	WAKE NUMERICAL SIMULATION USING CFD	40
4.5.6	WAKE MODELS ACCURACY	41
5	RESULTS AND DISCUSSION	42
5.1	WIND AND POWER GENERATION ANALYSES FOR SITE A	42
5.1.1	ATMOSPHERIC AND WIND CHARACTERISTICS AT SITE A ..	42
5.1.2	WIND SHEAR	44
5.1.3	TURBULENCE INTENSITY	47
5.2	WAKE MODELING ANALYSIS FOR SITE B.....	51
5.2.1	METEOROLOGICAL MAST DATA CHARACTERISTICS FOR SITE B.....	51
5.2.2	LIDAR DATA CHARACTERISTICS FOR SITE B	53
5.2.3	SIMPLIFIED WAKE MODELS PARAMETERS	59
5.2.4	CFD WAKE MODEL CONFIGURATION.....	60
5.2.4.1	MESH AND BOUNDARY CONDITIONS.....	60

5.2.4.2	TURBULENCE MODEL	62
5.2.5	COMPARISON OF WAKE MODELS AND LIDAR MEASUREMENTS	63
5.2.5.1	5 ms ⁻¹ WIND SPEED BIN	64
5.2.5.2	6 ms ⁻¹ WIND SPEED BIN	67
5.2.5.3	7 ms ⁻¹ WIND SPEED BIN	70
5.2.5.4	8 ms ⁻¹ WIND SPEED BIN	73
5.2.5.5	9 ms ⁻¹ WIND SPEED BIN	75
5.2.5.6	10 ms ⁻¹ WIND SPEED BIN	78
5.2.5.7	11 ms ⁻¹ WIND SPEED BIN	80
5.2.5.8	12 ms ⁻¹ WIND SPEED BIN	83
5.2.6	WAKE MODEL ACCURACY ASSESSMENT	85
5.2.6.1	RMSE ANALYSIS FOR THE WAKE CENTERLINE	85
5.2.6.2	RMSE ANALYSIS FOR THE WAKE CROSS	86
6	CONCLUSIONS AND RECOMMENDATIONS.....	89
	REFERENCES.....	91

1 INTRODUCTION

The demand for energy has been increasing in the last decade due to the global economic growth. Such development has risen quickly over the past three decades. Fossil fuels have become a point of environmental concern. Increasing energy consumption not only results in depletion of energy resources but also gives rise to problems like global warming and greenhouse effect through emissions generated by burning of fossil fuels. As result of that, some countries were driven to prospect and adjust to renewable resources to maintain the expanding energy requirement.

Therefore, the development of several sources of renewable energies, such as solar, hydropower and wind energy is extremely important and timely. Amid these renewable resources, wind energy has offered a range of advantages, as technology already developed along with a prospection on the market (Leung & Yang, 2012).

Wind power has gained respect in terms of progress and potential as a clean resource. This selective evolution is explained due to the global availability of such resource, reason that has brought a growing success and has pushed the development of the wind farms. Moreover, beyond its recognition as one of the cleanest energy, its cost has been falling and becoming financially more feasible by many reasons such as tax breaks. As consequence, a large number of farms have been developed at onshore and offshore locations over the past years.

Many countries have accomplished high standards of wind power application, such as 21% of electricity production in Denmark, 18% in Portugal, 16% in Spain, 14% in Ireland and 9% in Germany in 2010. By the end of 2013, 90 countries around the world operated commercial wind power installations with total installed capacity of 318 GW, providing about 3% of global electricity supply at the end of 2013. Wind power production has gained an exceptionally fast growth in the past 20 years, being a sophisticated and efficient technology for electricity production (Bhattacharyya & Timilsina 2009; GWEC 2014).

The most significant regions of new expansion are in Brazil, Mexico and South Africa. Brazil is the leader in wind power installed capacity. The wind resources in the country represent an enormous potential. After a reluctant start

to wind power growth in the beginning of the 2000 decade, the Brazilian wind market has now advanced significantly. In 2011, Brazil reached 1.5 GW of installed capacity, and by the end of 2013, the total installed capacity exceeded 3.4 GW. The country reached over 10 GW in February of 2017, representing a huge cumulative growth, which has not being seen frequently, apart from China in the period 2005-2010 (GWEC, 2014; Abeeólica, 2017).

Wind energy projects endure the disadvantage of the wind resource intermittency; thus, the wind turbines do not run steadily because the wind does not blow constantly over time. Therefore, wind energy projects are treated as energy-replacement instead of capacity-replacement resources. The quantity of energy that can be provided by layouts of wind turbines rely upon the wind resource availability and on the character of the load being supplied. Because of that, it is essential to study the efficiency of these power generation systems by assessing the effects that wind parameters and wakes will have on the whole system and on its reliability.

A complete assessment of wind resources is crucial to retain full advantage of wind power. For instance, accurate and correct measurements of wind speed decrease the needs of massive investments. In site, the wind measurements are commonly made at different heights, but not coinciding with the hub height of the rotor. The wind velocity at a given site increases with height by a power factor called the wind shear coefficient. This coefficient is extremely variable to the site where the measurements are performed. The other two crucial parameters that influence the energy production evaluation are the turbulence kinetic energy and turbulence intensity, which are related to atmospheric stability that could affect the power performance (Rehman and Al-Abbadi, 2005; Wharton and Lundquist, 2012).

Wind turbines generate wakes, which are areas of flow with lowered momentum and enlarged turbulence. Such phenomena is induced by the energy extraction from the wind, where each wind turbine produces a turbulent region with slower wind velocities downstream, thus leading to decreased energy yield for the downstream wind turbine. The development of wake surely affects power output and, because of that it is essential for wind power plants developers to be capable to both quantify and estimate the magnitude of the uncertainties and

characteristics of the flow behind the turbine. Attending to study and project large wind farms layouts, modeling of wake effects is a crucial element of the energy yield. Looking to diminish power losses and increase the lifetime of the blades, it is essential to have a valuable understanding of the behavior of wakes in wind power plants. Such knowledge can be obtained by modeling the wake effects in wind turbines (Mo et al., 2013; Vermeer et al., 2003; Tsalicoglou, 2012).

With the development of the computational technology, CFD is expanding into complex problems involving fluid-structure interaction. However, in most situations, a simplistic modeling is satisfactory to evaluate the effects of turbulence on the flow. Although, the application of large scale simulation (LES) has gradually increased for wind power simulations, but a large part of the simulations is represented by the Reynolds Average Navier-Stokes (RANS) equations, derived from the fundamental assumptions of mass conservation and momentum (Yildirim et al., 2013; Rapaka and Sarkar, 2016).

This work has developed a verification of the aerodynamics of a wind turbine, including analysis of how wind characteristics parameters affect the energy power production. Moreover, it has compared semi empirical existing wake models with wake results obtained by Light Detection and Ranging (LiDAR) measurements, which are used to understand the physics concepts behind wind turbine wakes. At the end, a Computational Fluid Dynamics (CFD) model has been implemented for simulating flows around a single wind turbine, by solving the Reynolds Averaged Navier-Stokes (RANS) equations.

1.1 JUSTIFICATION

Wind energy is one of the most promising renewable energy sources around the world, this is mostly due the recent significant enhancement on wind energy conversion technologies efficiency. Therefore, in order to achieve optimal technology performance, it is pivotal to develop specialized studies on the wind flow through wind turbines.

1.2 OBJECTIVE

This study has a general objective to evaluate the performance of wind energy generation by vertical wind profile analysis seeking to determine the influence of wind characteristics parameters in wind energy production and compare existing wake models with wake measurements by LiDAR, as well as, a numerical simulation of aerodynamics of the turbine using CFD.

1.3 GOALS

The goals of this research are:

1. Basic statistical analysis of LiDAR data.
2. Identify and determine parameters of importance for the project, such as: wind shear, wind diurnal profile, turbulence intensity, wind speed distribution and wind rose;
3. Comparison among power performance generation with parameters of importance and identification of ranges are generating the best results.
4. Applying wakes models that are useful to the industry and compare with LiDAR measurements data to different boundary conditions.
5. Numerical simulation of aerodynamics around a wind turbine generator through CFD.

1.4 MASTER THESIS CHAPTERS

Chapter I presents the introduction of the research, where defines the justification, objectives and goals.

Chapter II develops the review of principles aspects that are retreated at the dissertation, divided by physical aspects, wind assessment and wake models.

Chapter III presents the case study, reporting the study area subdivided by site A and B, alongside with the data.

Chapter IV describes the methodology applied in the research, which is divided by data quality control, wind rose, wind speed distribution, wind analysis parameters and wake modeling.

Chapter V details the results and discussion obtained by the evaluated analysis at this work, the subsections are the wind and power generations analysis for site A and wake modeling analysis for site B.

Chapter VI finishes with the conclusion and recommendations for future studies in the area.

2 REVIEW

This chapter presents a literature review by discussing the main concepts and considerations about wind power generation, wind parameters and wake modeling that have been applied to develop the wind energy system.

2.1 PHYSICAL ASPECTS

Wind turbines generate electricity by taking the raw power of the wind to induce a generator. Wind turbines convert the kinetic energy of the flow that passes the swept area of the wind turbine to mechanical torque on the rotor hub. Such torque is transformed into electrical energy by an electromagnetic conversion with the assistance of an electric generator.

The kinetic energy related to the inflow wind over the wind turbine blades that rotate on a cross section A is given by

$$E_c = \frac{1}{2}mv^2, \quad (2.1)$$

where E_c is the kinetic energy (Joules); m is the airflow mass (kg); V is the wind speed (ms^{-1}).

Therefore, the power produced from wind speed is defined as the time rate of kinetic energy, and then the power of an air mass with density ρ flowing at wind speed V through an area A can be expressed as

$$P = \frac{1}{2}\rho Av^3. \quad (2.2)$$

However, according to Betz's theory, the maximum value that the efficiency of a wind turbine can reach is 59.3%, as the air decelerated when it approaches the rotor plane. Though the efficiency of current wind turbines is around to half of this optimal value (Çengel and Cimbala, 2006).

2.1.1 THE ACTUATOR DISC CONCEPT

The basic theory of rotor aerodynamics is based on Betz's Blade Element Momentum (BEM) theory that models an optimal one-dimensional flow through a rotor disc. The rotor obtains mechanical energy from the flow by reducing its kinetic energy and thus its velocity (Tsalicoglou, 2012)

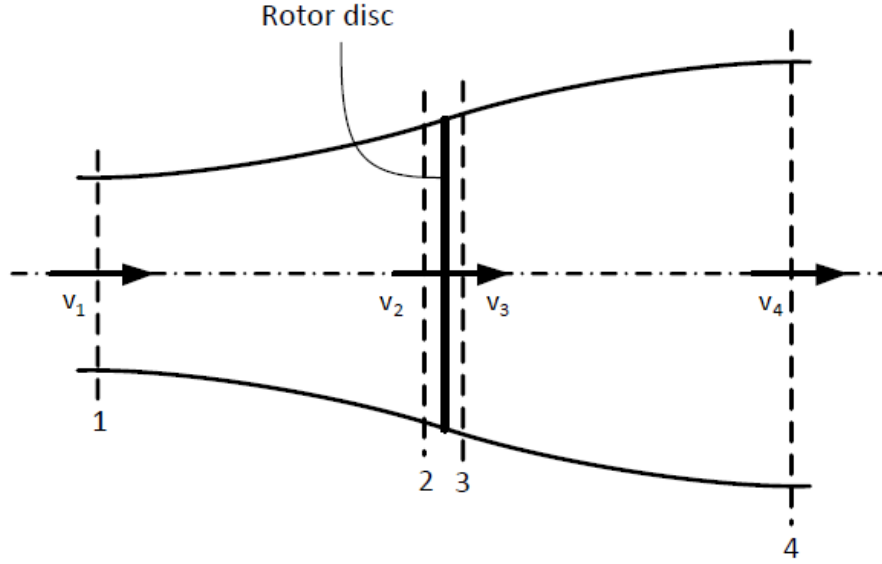


Figure 1: Stream tube positions when using Betz analogy

Source: adapted from Tsalicoglou (2012)

Consequently, if a stream tube is considered, the cross-sectional area through which the flow passes has to increase to ensure the conservation of mass. To better describe these considerations four locations of the flow are defined as: 1: free flow; 2: flow just upstream of the turbine rotor; 3: flow just downstream of the turbine rotor; and 4: flow far downstream of the turbine rotor (Manwell et al., 2009). If v_1 is the velocity of the undisturbed flow and v_4 the reduced velocity of the flow far behind the rotor, the area A_4 downstream of the rotor needs to be larger than A_1 in order to maintain a constant mass flow rate \dot{m} :

$$\dot{m} = \rho v_1 A_1 = \rho v_4 A_4. \quad (2.3)$$

The obtained mechanical power is then given by

$$P = \frac{1}{2} \rho (v_1^3 A_1 - v_4^3 A_4) = \frac{1}{2} \dot{m} (v_1^2 - v_4^2), \quad (2.4)$$

and the thrust force on the rotor is

$$F_T = \dot{m}(v_1 - v_4). \quad (2.5)$$

Assuming the point that no work is done on either side of the rotor, the Bernoulli equation can be applied in the transition from 1 to 2 and 3 to 4, then the total pressure, p_t of the flow still consistent in these regions, thus $p_{t,1} = p_{t,2}$ and $p_{t,3} = p_{t,4}$, with p_t given as:

$$p_t = p + \frac{1}{2}\rho v^2. \quad (2.6)$$

Assumptions have to be made to derive a new equation from equation (2.5). Those assumptions take in consideration the fact that sections 1 and 4 are sufficiently far from the turbine then $p_{t,1} = p_{t,4} = p_{atm}$ and $v_2 = v_3$. The sum of the forces on either sides of the turbine is $F_T = A_2(p_2 - p_3)$. Then:

$$F_T = \frac{1}{2}\rho A_2(v_1^2 - v_4^2). \quad (2.7)$$

The velocity at the hub height can then be derived by equaling the equations (2.5) and (2.7), resulting in:

$$v_2 = v_3 = \frac{(v_1 + v_4)}{2}. \quad (2.8)$$

Thus the conclusion is that the average velocity of a fluid through a turbine is the arithmetic average of the upstream and downstream velocities. The validity of this result is limited by the applicability of the Bernoulli equation (Çengel and Cimbala, 2006).

The decline of wind velocity between sections 1 and 2, associated to the velocity of the free stream is defined as the axial induction factor, ω :

$$\omega = \frac{(v_1 - v_2)}{v_1}. \quad (2.9)$$

As the axial induction factor increases from 0, the wind speed behind the rotor slows continuously. If $\omega = 1/2$, the wind has slowed to zero velocity behind the rotor and the simple theory is no longer applicable.

Manipulating the given equation above, the power can be written as:

$$P = \frac{1}{2} \rho A_2 v_2^3 4\omega(1 - \omega)^2, \quad (2.10)$$

where the control volume area at the rotor, A_2 , is replaced by A , the rotor area, and the free stream velocity v_2 is replaced by V .

Wind power performance is generally characterized by its power coefficient, C_p :

$$C_p = 4\omega(1 - \omega)^2. \quad (2.11)$$

That can also be written as function of power

$$C_p = \frac{P}{\frac{1}{2} \rho A V^3} = \frac{\text{Rotor power}}{\text{Power in the wind}}. \quad (2.12)$$

The non-dimensional power coefficient represents the fraction of the power in the wind that is extracted by the rotor (Manwell et al., 2009). In a similar way to the power, the thrust can be established by a dimensionless thrust coefficient:

$$C_T = \frac{F_T}{\frac{1}{2} \rho A V^2} = \frac{\text{Thrust force}}{\text{Dynamic force in the wind}}. \quad (2.13)$$

Therefore, the thrust coefficient related to an ideal wind turbine is equivalent to eq. (2.11), where C_p turns C_T and has its highest value in $\omega = 0.5$, which reaches $C_T = 1$. However, for maximum power where $\omega = 1/3$, the thrust coefficient reaches value of around 0.89 (Manwell et al., 2009).

2.2 WIND ASSESSMENT

Wind turbines are operating in the lowest part of the atmospheric boundary layer. This complicates the calculation of the flow around the turbines. Though wind speed is a dependent variable parameter that optimizes the power

generation for a wind turbine, thus the maximum efficiency can be achieved at all wind velocities. In addition, the power output primarily depends on the mean speed of the inflow wind. However, this system requires high quality parameters for calculation of the optimum wind turbine power generation. The effectiveness of maximum power control with the identified parameters can be verified through simulations of the wind power generation system. The power output primarily depends on the mean speed of the inflow wind.

2.2.1 WIND MEASUREMENT AND LIDAR

Obtaining a good estimate of wind speed is crucial in a wind farm project. For large installations, a good deal of expert assessment of wind speeds will be of highest importance to the efficiency of the project. However when it comes to smaller projects, there is often lack of analysis of the aerodynamics characteristics of the wind.

High-quality site wind speed measurements are therefore important to reduce the uncertainty of the energy produced estimation of a project. Nowadays there are some equipment that are able to measure wind speeds, such as, anemometer, LiDAR and SODAR (Moore, 2010; Lang and McKeogh, 2011; Wandinger, 2005; Carsewell, 1983).

A typical anemometry mast will have several anemometers installed at different heights on the mast, and vanes, which are devices that measure wind direction. These devices will be connected to a data logger, via cables. Remote sensing has gained space and the technology available for this is being refined quickly. The devices are basically ground-based, which can measure at a range of heights externally the use of mat masts (Clive, 2012).

SODAR (Sound Detection and Ranging) emits and receives sound waves which yield wind speed through the Doppler Shift principle (Vogt and Thomas, 1995; Lang and McKeogh, 2011).

LiDAR (Light Detection and Ranging), which also works with the Doppler Shift principle, emits light waves from a laser and receives the signal back from airborne particulate matters. In addition, LiDAR devices are currently quite expensive to purchase, but suitable wind measurements can be acquired using it. This offers an opportunity to make significant savings on the cost of data

acquisition and as a result boost the return on investment associated with these data (Clive, 2011; Wandinger, 2005).

LiDARs identify the Doppler shift in the laser emissions frequency, which is back-spread by aerosol particles heading in the wind. Such movement establishes a Doppler shift on the frequency of the back-spread discharge expressly equivalent to the element of the wind speed vector ahead the line of sight (LOS) wherever the laser discharges radiates. Interpreting a wind velocity from Doppler shifts and equivalent LOS radial wind speed vector elements, the difference acquired by changing the direction of the beam in relation to the wind direction have to be checked (Clive, 2016).

LiDAR measurements frequently include the operating function with a scan geometry to collect radial speeds from three elementary directions and assessing wind speed in accordance with the following equation (2.14) (Wang et al., 2016, Sathe et al., 2011):

$$v(s) = d^T u, \quad (2.14)$$

where $d^T = [\cos\varphi \sin\theta, \cos\varphi \cos\theta, \sin\varphi]$ and $u = [v_x, v_y, v_z]$. The radial velocity v is the prolongation of the wind speed u on the line of sight (LOS) at the position $s = sd$ for which s is the distance from the LiDAR ahead the LOS and d is the unit directional vector driven by the elevation angle φ and the azimuth angle θ of the LOS from north. Equation (2.14) can be written as (Werner, 2005):

$$v(s) = v_x \cos\varphi \sin\theta + v_y \cos\varphi \cos\theta + v_z \sin\varphi \quad (2.15)$$

If we fit Figure 2 to a function that displays the amplitude behavior (A) of the sinusoidal gradient in radial velocity is equivalent to the wind speed supporting flow homogeneity, which the hypothesis that every LiDAR beam authenticates the identical wind speed vector (V_H) is genuine. The scan geometry present the opportunity to obtain wind data from a volume of air, which is not limited to the volume instantly superior the device, using low elevation angle (Clive, 2016; Werner, 2005).

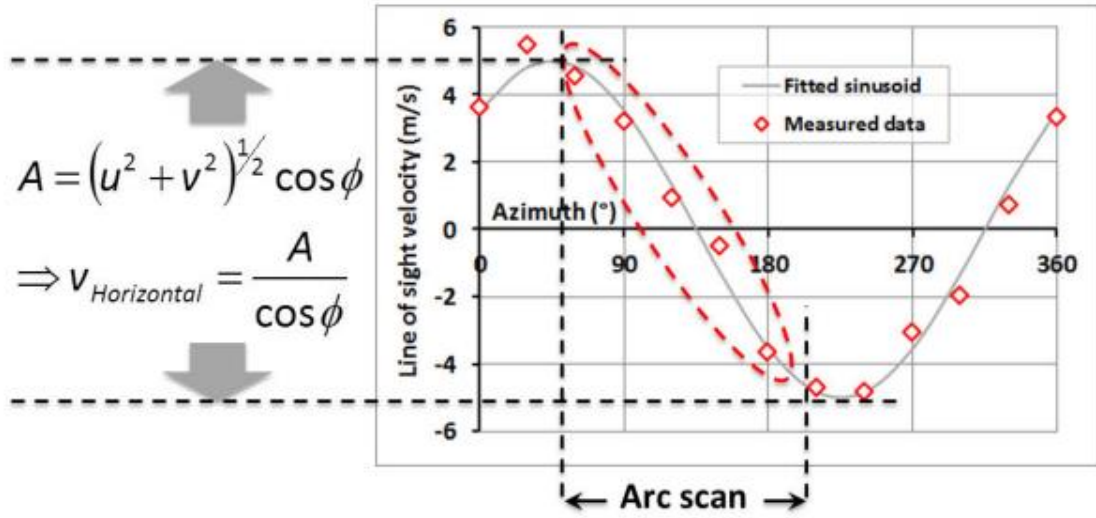


Figure 2: Deriving wind speed from Doppler shifts observed by LiDAR

Source: Clive, 2016

Therefore, horizontal wind speed vector (V_H) can be written by:

$$V_H = (v_x^2 + v_y^2)^{1/2} = \frac{A}{\cos \phi} \quad (2.16)$$

The Arc Scans or PPIs contain the asset by sampling exclusively the area of attraction, which the total collection repetitions in a given period can increase.

2.2.2 ATMOSPHERIC BOUNDARY LAYER

The winds have their origins in the effects of differential solar heating on the earth's surface. The resulting temperature and pressure differences, with the addition of Coriolis forces, are responsible for the large scale motion of air masses along the lines of constant pressure as indicated in weather maps (Manwell et al., 2009). At altitudes of the order of 1000 m, the effects of earth's surface friction can be neglected, and the wind is determined mainly by these large scales pressure patterns. However, at lower altitude, where occurs the utilization of wind energy, the wind is limited by surface friction.

The wind over the earth's surface may be assumed as composed by two time-dependent terms: average velocity and fluctuating velocity. The average wind speed is proportional to the "wind gradient". The fluctuating wind is the unsteady, continuously unstable and varying randomly (Rohatgi & Barbezier,

1999). These variations are responsible for the vertical transport of horizontal momentum by which surface shear stress is transmitted through the atmospheric boundary layer.

The wind speed profile in the atmospheric boundary layer is frequently designed by a logarithmic function (Sanderse, 2009):

$$v(z) \propto \ln\left(\frac{z}{z_0}\right) + F_{st}, \quad (2.17)$$

with z_0 the surface roughness length, a quantity that expresses how the atmospheric boundary layer interacts with the surface, ranging from 0.01 m very flat terrain to 0.7 m for forests and urban areas. F_{st} is a function which depends on stability (Burton et al., 2001). For neutral atmospheric conditions, the function is small and the equation (2.13) reduces to:

$$v(z) \propto \ln\left(\frac{z}{z_0}\right). \quad (2.18)$$

2.2.3 STABILITY

The tendency to endure vertical motion or to restrain existing turbulence is defined by stability, which is a crucial characteristic of the atmosphere. The boundary layer turns its stratification stable on any occasion of the elemental surface has lower temperature compared to the air. The effects of stability on turbulence and wind shear are relevant to wind power applications. Turbulence is highly associated with stability and also wind shear, that is developed in the early stages of the first kilometer above the ground, is particularly influenced by the stability of the atmospheric boundary layer, which is general classified as stable, neutrally stable, or unstable (Manwell et al., 2009). Subject to the condition that turbulence is induced due shear and dissipated due negative tendency to float and viscosity. Because of this conflict, the turbulence intensity in stables boundaries is a lot vulnerable than the neutral and unstable boundary layers. Resulting in hollow and identified by tinier eddy movements at stable conditions (Basu and Porté-Agel, 2006).

Turbulence produced under unstable conditions may influence turbine load and performance, due the development of mixing between air portions at distinct

heights, by that diminishing the vertical variability of wind (Roy & Sharp, 2013). For that reason, a stable atmosphere that presents small turbulence drives to high wind shear, while an unstable atmosphere generates the minimum quantity of wind shear. High wind shear indicates a faster variation in wind velocities with height. Therefore, in stable conditions hub height wind velocities point to be greater than the under winds, thus its huge gradient generates torque across the rotor which could be the source of the fatigue (Sathe et al. 2012; Rohatgi & Barbezier, 1999).

Improving the knowledge involving environmental atmospheric stability, its effect on turbulence and wind shear is crucial for assisting wind farms developers in achieving efficiency optimization. Studies of stability effects on a single wind farm's production can support greater management for long-term operation and maintenance designs. Developing better stability models may essentially raise the power output production (Roy & Sharp, 2013).

2.2.4 WIND SHEAR

Wind shear might be defined as the local variation of wind vector. Such variation can be measured as the spatial change in any direction of the wind speed. For practical purposes in industry, wind shear is generally assumed to be the variation of wind speed with height above ground level (Mclaughlin 2012).

Over rough terrain, the wind shear decreases near the ground, but there is a compensated increase in higher layers. Unstable air tends to rise, intensifying the vertical mixing and reducing vertical wind shear in grand part of the layers. However, in stable conditions, the vertical motion slows down and consequently vertical wind shear might become extremely high. Vertical wind shear is a crucial parameter in wind energy projects, because it is directly correlated to the productivity of wind turbine output and it reduces the lifetime of the turbine rotor blade (Honrubia et. al., 2009).

A power law is usually used to represent vertical wind profiles. The basic equation of wind shear power law is as follows (Chehouri et. al., 2015):

$$V(z) = V_r \left(\frac{z}{z_r} \right)^\alpha, \quad (2.19)$$

where z is the elevation above the ground level; z_r is the reference altitude; α the wind shear exponent; V_r is the wind speed at the reference altitude. The exponent α often ranges from 0.1 to 0.4, varying according to the terrain roughness and the air temperature variation (Manwell et al., 2009). A power law, characterized by an exponent, is a reasonable approximation to the logarithmic law and has the advantage that it is much more straightforward to find an analytical solution for an exponent.

2.2.5 TURBULENCE

Atmospheric turbulence is the set of random and continuously changing air motions that are superimposed on the average of the wind motion. Its impact can influence the power performance, and also cause effects as turbine loads, fatigue, wake effects and noise propagation. Turbulence is related to the topography of the site and also depend on of the atmospheric stratification (Gottschall & Peinke, 2008; Prospathopoulos et al., 2011) Low turbulence conditions are linked with stable conditions, which describes the persistence or consistence of wind speeds, whereas in unstable conditions the wind speed strongly changes with height therefore the turbulence intensity is high (Kaiser et. al., 2007).

Turbulence intensity is, following the International Electrotechnical Commission (IEC) standard for wind turbine power performance measurements, IEC 61400-12-1, estimated in wind power as the ratio of the standard deviation, σ , of 10 minute wind speed dataset by its mean wind speed, \bar{V} , according to the equation (Wharton & Lundquist, 2012)

$$I = \frac{\sigma}{\bar{V}}. \quad (2.20)$$

Steady wind flows deliver lower turbulence intensity, on the contrary, the turbulence is high when wind fluctuates fast. Hence, often the literature reports values of horizontal turbulence intensity in the range from 3% to 20% (Wharton and Lundquist, 2010).

Sheinman and Rosen (1992) demonstrated that neglecting the effect of wake turbulence in the incoming wind speed can lead to an overestimation of turbine output slightly over 10%. In particular, the velocity deficit, which is highly related to power losses in wind farms, recovers faster when the turbulence intensity level of the incoming flow is higher, which usually occurs near to the high turbulence turbine zone (Wu and Porté-Agel, 2012). Turbulence from the upwind turbines affects the power performance of the downwind turbines whenever the wind direction gets aligned with the wind farm turbines.

2.2.6 POWER PERFORMANCE ANALYSIS

Environmental external forces have to be considered for the study of wind turbines loading and fatigue. Primarily due to the interaction of wind with different components of the wind turbine, result not only the reduction of energy output, but also reduce the lifetime of the constituent materials.

Fatigue affects the lifetime of wind turbine components that are expected to withstand continuously varying loads. Rotor blade fatigue life is influenced by the cyclic loads resulting from rotation through a wind field that varies in the vertical direction (Manwell et al., 2009). This is particularly the case if they are located in a very turbulent wind climate associated with relative wind shear variation, which is strongly correlated with turbine produced wakes. Kim *et al.* (2015) reported that the wind variation caused by wake effect, which produces high fluctuation on mechanical loads, can be estimated through both turbulence intensity and wind shear gradient. The study was based using steady and dynamic power curves. The authors found that for the low wind velocities, the power curves had different behavior even though the high turbulence intensity profile was incorporated. However, the authors understood that when a site has a low mean wind speed, the energy improvement for low wind velocities would compensated for the power losses for higher velocities, due to the high turbulence intensity effect. Therefore, the study concluded that high turbulence intensity significantly increases the fatigue load. Adaramola and Krogstad (2011) showed that the power losses for a turbine operating in the wake of the upstream wind turbine are important; with the maximum loss in

the downstream turbine varying from 20 to 45% depending on the distance between the turbines and their operating conditions. The power losses for the downstream wind turbines are directly linked with the velocity deficit in the wake area, which means that inferior quantity of energy is available in the downstream turbine. The authors found that the improvement of the power coefficient of the downstream turbine, is about 29% higher for yaw angle corrected upstream wind turbine than the non-yawed upstream turbine.

2.3 WAKE MODELS

Due to the fast growth in the number and size of installed wind farms around the world, wind-turbine wakes have become an important topic of study. As many wind turbines in wind farms have to operate in the wakes of upwind turbines, they are exposed to incoming wind velocities that are smaller than those under unperturbed (without wake) conditions; as a result, turbine wakes are responsible for significant power losses in wind farms (Bastankhah and Porté-Agel, 2014). Barthelmie *et al.* (2007) reported that wake losses, for a given wind direction, can be as much as 10–20% of the power when no wakes are present. The comprehension of power losses expected to wind turbine wake on wind plants is vital to improve the wind farm display. However, power losses detected by a single wind turbine due to wakes are closely to 10% generally. Although, the wind farm output energy reduction may range from 5% to 8% of the annual energy yield.

Therefore, it is necessary for wind park developers to be able to estimate quantitatively and with small uncertainties the extent and characteristics of the flow downstream of wind turbines (Tsalicoglou, 2012). Extensive analytical, numerical and experimental efforts have been carried out to better understand and estimate turbine wake flows. Although numerical and experimental techniques have become increasingly sophisticated and accurate in recent years, simple analytical models are still useful tools to estimate wind-turbine wake flows and their effect on power production. Analytical models are widely used due to their simplicity and low computational cost (Bastankhah and Porté-Agel, 2014; Crespo *et al.*, 1999; Katic, *et al.* 1986; Kiranoudis and Maroulis, 1997).

In order to reduce computational costs, analytical models assume that wake geometry and intensity are functions of both the inflow conditions and the turbine's operating point. Vermeer *et al.* (2003) reviewed several analytical models that estimate wake development, interaction and superposition. However, an accurate understanding of the effects of unsteady flow regime is of huge significance, as turbines generally perform in unsteady environment that may be produced by yaw, wind shear, the tower shadow and dynamic wind flow (Leishman, 2002).

The wake is normally represented in two zones; a near wake, where the induced wake of the isolated rotor blades can be identified; and a far wake, whose properties are reported in experimental studies and simulations in the literature (Renkema, 2007; Vermeer *et al.*, 2003). The near wake is distinguished by the existence of edge vortices that trail a spiral course, separating the fluid with lower velocity within the wake from the faster fluid external to the wake. The free shear layer, that develops between the lower and larger velocity regions, widens as the vortices combine and expands downstream, which characterizes the far wake (Crespo *et al.*, 1999; Politis *et al.*, 2015).

The analytical models that are used by the industry are terse in the physical representation of the phenomena in comparison to most of the advanced methods based on CFD models. An advantage of the analytical models to point out is the lower cost compared to the more computationally expensive models that not always represents the wake with better accuracy (Crespo *et al.*, 1999). However, there are cases where the analytical models represent reality poorly; then CFD models are employed aiming a higher accuracy description as example of complex topography (Nedjari *et al.*, 2017; Prospathopoulos *et al.*, 2010).

2.3.1 SIMPLIFIED MODELS

Many wake models are established on the fundamental assumption of conservation of mass and momentum. The goal of wake models employed in energy yield estimation software is to represent the turbine induced wind speed deficits and the ratio of restoration to the free stream velocity.

The simplified models neglect some terms of the Navier-Stokes Equations and consider the wake to be consistent and axisymmetric for

increasing solving velocity. The quickest methods are developed to model the wake expansion directly rather the turbulence, as the models of: Jensen, Frandsen, Larsen and Ainslie (eddy viscosity model). They fundamentally simulate momentum conservation at wake area that is expanded in agreement with a factual wake development function (Rethore, 2009).

2.3.1.1 PARK (JENSEN) MODEL

One of the first wake models is the one proposed by Jensen (1983). The model, illustrated in Figure 3, is a simplification of the reality, which assumes a top-hat shape for the velocity deficit in the wake, then taking into consideration a gradually developing wake with a velocity deficit that is only relative to the distance behind the rotor, which means that expands radially at the rate $(k x)$. This model is deficient for the far wake, but it is a fairly good representation for the near wake (Janssen, 2012).

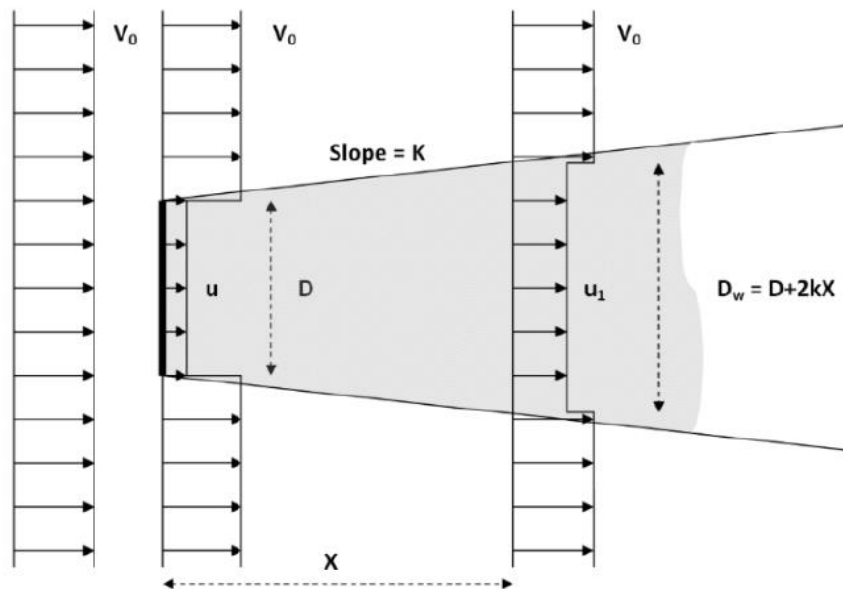


Figure 3: Jensen wake model

Source: Janssen, 2012

The mass balance for the control volume of Figure 3 is given by equation (2.21):

$$D^2 u + (D_w^2 - D^2) V_0 = D_w^2 u_1, \quad (2.21)$$

where D is the rotor diameter; D_w is the wake diameter; V_0 is the free stream wind velocity; u_1 is the wind velocity deficit. Then assuming the wind speed just after the wind turbine rotor, u , is $\frac{1}{3} V_0$, the equation (2.21) can be written as equation (2.22) for an ideal wind turbine:

$$\frac{u_1}{V_0} = 1 - \frac{2}{3} \left(1 + \frac{2kx}{D} \right)^{-2}, \quad (2.22)$$

Where k is the wake decay constant; x is the wake distance downstream of the wind turbine. The equation (2.22), can also be rewritten by using the “ ω ”, induction factor (equation 2.9), not considering a ideal wind turbine anymore, yielding equation (2.23),

$$\frac{u_1}{V_0} = 1 - 2\omega \left(1 + \frac{2kx}{D} \right)^{-2}. \quad (2.23)$$

The induction factor (ω) can also be written as function of the thrust coefficient, C_T , which is a coefficient applied to indicate the maximum thrust force resulting from the energy conversion equipment,

$$\omega = \frac{1 - \sqrt{1 - C_T}}{2}. \quad (2.24)$$

These assumptions yield the Jensen wake model, that can be used to calculate the wind speed deficit as,

$$1 - \frac{u_1}{V_0} = \frac{1 - \sqrt{1 - C_T}}{\left(1 + \frac{2kx}{D} \right)^2}. \quad (2.25)$$

The wake development can be computed as,

$$D_w = D + 2kx. \quad (2.26)$$

The equation (2.23) states k as the wake decay constant, which represents the dissipation of the wake as the wake width increases. The large wake decay means a rapid decrease of the wake and a large rate of wake width increase. The value of k is usually adopted to be 0.075, which is adequate for onshore wind farms, but for offshore the use of a 0.04 – 0.05 value is recommended.

The Jensen model hypothesis requires that, $C_t < 1$, the thrust coefficient of the rotor must be lower than one (Renkema, 2007).

2.3.1.2 FRANDSEN WAKE MODEL

In order to estimate the wake in wide wind farms, Frandsen et al. (2006) developed a wake model that was initially used for offshore wind turbines, which use could be extended for onshore conditions, if they were similar to offshore, that is very low roughness. The kinematics energy deficit downstream of the turbine is determined and sustained as the wake develops downstream. The wind speed deficit is computed taking into consideration a circular wake area, which develops until hitting the terrain or sideways wakes, thus considering a circular control volume with stable cross-sectional region equivalent to the wake sector. When one considers a single wake in a wind farm, the velocity deficit for Frandsen model is given by

$$u = \frac{V_0}{2} \left(1 \pm \sqrt{1 - 2 \frac{A}{A_w} C_T} \right), \quad (2.27)$$

where u is the velocity deficit, V_0 is the freestream velocity, $\frac{A}{A_w}$ is the ratio between the rotor and wake area and C_T is the thrust coefficient.

The model assumes three distinct wake zones: in the first zone a single wake is produced with no synergy among adjacent wakes. The second zone begins when two adjacent wake streams merge; the wake development is restricted to an enlargement just in the vertical direction, when represented in 2D. The third zone occurs when the wake flow is in equilibrium with the atmospheric

boundary layer, which only can happen when the wind farm is sufficiently and extremely large.

2.3.1.3 LARSEN WAKE MODEL

The Larsen wake model is based on Prandtl's turbulent boundary layer equations, being recognized as *EWTS* (European Wind Turbine Standards II). The wake expansion in terms of wake radius and wind velocity profile have a closed form solution, which means that in order to gather that class of solution a self-similar wind speed profile is required. The model also assumes the Prandtl's mixing length theory, thus the wind flow is presumed to be incompressible, stationary and axisymmetric (Larsen, 1988; Larsen et al., 1996).

The wind speed deficit, count on both the radius (r) and the downstream length from the wind turbine (x). The equation used to calculate the wind speed deficit at the radial location r and at the downwind location x is

$$V_0 - u_x = -\frac{V_0}{9} (C_t A (x + x_0)^{-2})^{1/3} \left\{ r^{3/2} (3c_1^2 C_t A (x + x_0))^{-1/2} - \left(\frac{35}{2\pi} \right)^{3/10} (3c_1^2)^{-1/5} \right\}^2, \quad (2.28)$$

where V_0 is the freestream velocity at rotor, u_x is the wind velocity, A the rotor area, c_1 the non-dimensional mixing length. Thus, the equation used to calculate the wake radius is:

$$R_w = \left(\frac{35}{2\pi} \right)^{1/5} (3c_1^2)^{1/5} (C_t A (x + x_0))^{1/3}. \quad (2.29)$$

2.3.1.4 EDDY VISCOSITY WAKE MODEL

Ainslie (1988) developed a wake model based on the numerical solution of the flow differential equations using an eddy viscosity model for system's closure. The eddy viscosity wake model is related to the shear layer estimation of the Navier-Stokes equation.

The model assumes the hypothesis of an axisymmetric, stationary, entirely turbulent wake with no circumferential velocity and insignificant pressure gradients external to the wake area. The axisymmetric assumption allows a two-dimensional characterization of the wake (Van Luvanee, 2006).

The model goal was to develop a physically based representation of the flow system, its description and governing equations can be found in Ainslie (1988). The eddy viscosity turbulence closure aims a more accurate simulation of the turbulent mixing in the wake shear layer (Janssen, 2012). Hence Navier-Stokes can be replaced by the simplified shear layer estimation which, neglecting viscosity in cylindrical coordinates. The shear layer estimation is linked with the axisymmetric assumption for the incompressible fluid continuity equation to build the differential equations system that simulates the wake. The mass conservation equation can be written as:

$$\frac{1}{r} \frac{\partial(rv)}{\partial r} + \frac{\partial u}{\partial x} = 0, \quad (2.30)$$

and the momentum equation in freestream direction by

$$u \frac{\partial u}{\partial x} + v \frac{\partial u}{\partial r} = -\frac{1}{r} \frac{\partial(r \overline{u'v'})}{\partial r}, \quad (2.31)$$

where u is the downstream velocity (ms^{-1}), v the radial velocity (ms^{-1}), the x downstream distance coordinate from the turbine (m) and r the radial distance coordinate from the wake centerline (m). The right side of the equality describes the alteration in acceleration, thus momentum transport crosswise the flow. $\overline{u'v'}$ is the Reynolds stress characterized as the cross-correlation of the turbulent elements of mean velocities u and v . The constant momentum transfer between adjacent fluid elements occurs due to the orthogonal fluctuating velocities, hence diminishing velocity gradients (Fox et al., 2004).

The turbulent viscosity approach is used to explain the Reynolds stress with an eddy viscosity (ε), determined by the following equations:

$$-\overline{u'v'} = \varepsilon \frac{\partial U}{\partial r} \quad (2.32)$$

$$\varepsilon = l_w(x) \cdot u_w(x) + \varepsilon_a \quad (2.33)$$

where, l_w is the wake length; u_w is the velocity deficit and both are responsible for characterizing the wake shear layer, ε_a expresses the ambient turbulence input to eddy viscosity (Janssen, 2012). Then the velocity gradient covering the shear layer, being a representation of the downstream distance, x , and not the radial distance, r .

2.3.2 NUMERICAL SIMULATION (CFD)

Computational fluid dynamics (CFD) is the branch of fluid dynamics that simulates real flows by means of the numerical solution of the governing equations. The objective is to reduce the effects of the assumptions limitations used in simplified methods.

The early usage of CFD in the framework of wind power performance studies was correlated with the estimation of two-dimensional airfoil characteristics. However, with technology growth in terms of computing capacity, the CFD has become a useful tool for the solution of many problems, ranging from a simple airfoil to the atmospheric boundary layer. Turbulent flows are so complex, that a direct solution is inaccessible, particularly for large Reynolds numbers (Sumner et al., 2010). However, in most situations a closure turbulence assumption is satisfactory to simulate the effects of turbulence on the flow stream.

In the past years, wake effects had been reported in CFD applications. Simulating the wind turbine rotation, which gives the most detailed information that is necessary to understand the behavior of the flow behind the wind turbine and in the swept area. However, the processing time of the simulation turns large when a high quality grid cells are used to accurately capture the rotational motion of the fluid though swept area (Nedjari et al., 2017).

Two common turbulence closure assumptions are: (1) large eddy simulation (LES) and (2) Reynolds-Averaged Navier-Stokes (RANS) equations derived from the fundamental assumptions of conservation of mass and momentum, which are described by (Pope, 2001):

$$\nabla \cdot \vec{U} = 0 \quad (2.34)$$

$$\frac{\partial \vec{U}}{\partial t} + \nabla \cdot \vec{U} \vec{U} = -\frac{1}{\rho} \nabla p + \nabla \cdot \vec{\tau} + \vec{f}, \quad (2.35)$$

where U represents the mean velocity vector, p is mean pressure, ρ is the fluid density, f represents a body force (i.e., Coriolis, buoyancy, gravity, etc.) and τ is the specific Reynolds stress tensor. To close the RANS equations, the Boussinesq linear isotropic eddy-viscosity hypothesis is often applied

$$\tau = 2\nu_t S, \quad (2.36)$$

where S is the mean strain rate tensor and the turbulent viscosity (ν_t). The choice of turbulence model depends on the problem and it is chosen to obtain a balance between desired accuracy and computational resources. Within this basic framework, a wide range of theoretical and practical problems can be investigated (Sumner et al., 2010).

Numbers of distinctive methods have been proposed to compute (ν_t), generally named zero-equation, one-equation and two-equation models. The $k - \varepsilon$ model is fitted into a two-equation model pattern, frequently applied in wind energy purpose. This approach is defined by adding two partial differential equations, one related to turbulent kinetic energy k and one for the turbulent dissipation ε . General approaching have been applied by simulating the flow characteristics in order to determine many different constants that the model carried, such as flow over a flat terrain or isotropic turbulence dissipation (Sanderse et al., 2011).

Current challenges related to CFD simulations are found when considered wakes behind a wind turbine, particularly when contrasting with experimental data. One of those challenges is the determination of inflow conditions that is representative in all significant characteristics of the environmental conditions (Sanderse et al., 2011). Prevenient studies of CFD simulations, the uniform and laminar inflow profiles were applied, however posterior works showed that both the appearance of the shear profile, (Wu and

Porté-Agel, 2012), likewise turbulence application in the inflow conditions (Troldborg et al., 2007) admitted a notable effect on the downstream wind flow behind the turbine.

The hypothesis of modeling the turbulence effect adding viscosity is well known applied for turbulent flows. Such theory is very useful, being dependent computationally on the Reynolds number. However, the efficacy of the Boussinesq hypothesis is relative restricted. Nevertheless, the CFD results are more accurate than simplified methods. The complexity of turbulent flows suggests that functional CFD developments will be the standard for the wind energy industry.

3 CASE STUDY

3.1 STUDY AREA

The study area comprises two sites, both in North America. Due to confidentiality requirements of the data providing company, SgurrEnergy¹, site locations and its detailed information were not described. Therefore the sites were described as site “A” and site “B”, hereinafter.

3.2 DATA

Data for this master’s dissertation was provided by SgurrEnergy, company that developed the feasibility study for both sites. Provided data are the supervisory control and data acquisition (SCADA), which is these devices/systems make use of data processing techniques in order to detect, predict faults and is installed into the wind turbine, and the data collected by the company using the Galion LiDAR, which an example of LiDAR installation is depicted in Figure 4.



Figure 4: Galion LiDAR used in sites A and B
Source: SgurrEnergy, 2015

¹ SgurrEnergy, www.sgurrenergy.com

The aim of the first campaign, on site A that consists in a flat terrain with annual average temperature of the region close to 22°C and approximately 10m above sea level, was to measure wind inflow conditions in order to characterize the atmospheric conditions around the swept area of a WTG, where the hub height is 80m above the ground. For the measurement campaign it was used a G4000 Galion unit installed on the ground, which is capable to range up to 4000m with 30m spatial resolution, the accuracy is close to 0.1 ms⁻¹ that permits to capture a maximum velocity up to 70 ms⁻¹. The measurement campaign lasted for 9 months in 2014, and the measurement characteristics, depicted in Figure 5, were: (1) scan geometry of 5 beams, incremented at 30° intervals in azimuth, and (2) angle of 18.32° on the vertical plane.

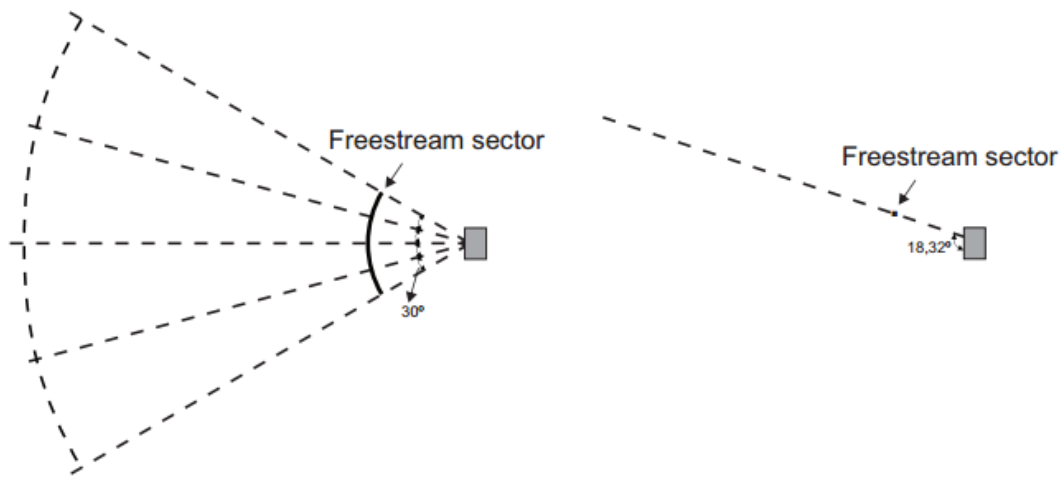


Figure 5: LiDAR Scan Geometry of 5 beams on site A

The second campaign, on site B, a flat plateau over 1500 m above sea level with annual average temperature close to 10°C that is also aimed the wake modeling study. For site B, the Galion LiDAR was mounted in a specific wind turbine generator (WTG), which was located at the first row of WTGs in the southern portion of the wind plant (Figure 6).



Figure 6: Galion positioning in the WTG for PPI Scan
Source: SgurrEnergy, 2012

The measurement campaign lasted for six weeks with a long range Galion LiDAR that took place from September 14th, 2011 until October 26th, 2011. A nacelle mounted deployment was selected at the site due to the retractable back door on WTG at 80m above ground, which enabled relatively easy installation and concurrent measurements through the horizontal plane of the wake. The Plane Position Indicator (PPI) scan collected data for a single wake analysis. The PPI scan mode consisted in a constant elevation angle and varying azimuth angles, such that data could be projected on a horizontal plane. It was carried out a scan with 84° width in $\pm 3^\circ$ azimuth increments centered on the 180° axis straight out behind of the WTG, as depicted in Figure 7. Thereby the 29-beam scan would take nearly four minutes to finish a scan period (SgurrEnergy, 2012).

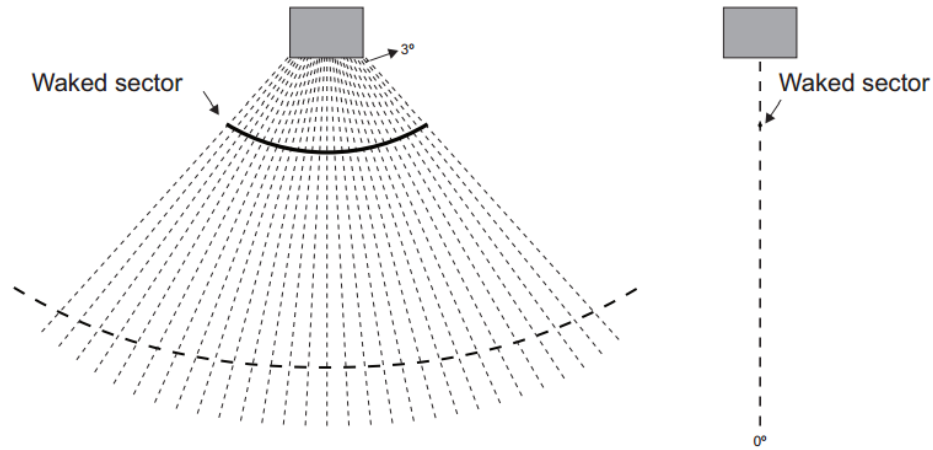


Figure 7: Site B Galion PPI Scan of 29 beams

Close to 300 m west of the WTG, a meteorological mast was installed in order to have the concurrent wind measurement data for both wind direction calibration pertinent to the WTG yaw angle, and freestream wind speed. The wind direction of interest for site B ranged from 90° to 270° , in order to evaluate a single wake.

3.3 FLOWCHART OF METHODOLOGIES APPLIED IN SITE A AND B

This section describes the separation of methodologies applied for site A and B, as presented in Figure 8.

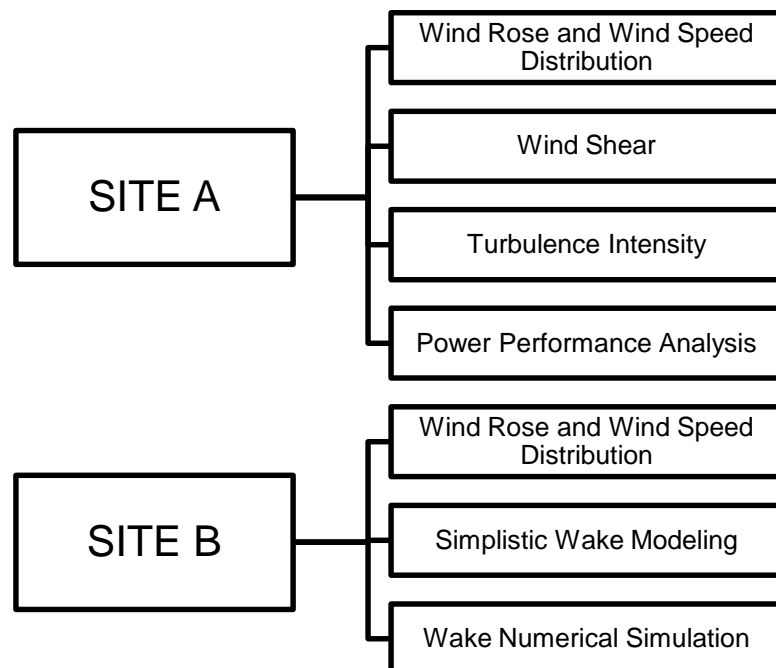


Figure 8: Flowchart of methodologies for Site A and B

4 METHODOLOGY

4.1 DATA QUALITY CONTROL

Data quality control aimed to eliminate redundancy or insufficient record samples. The first step was an initial screening to identify the indicators of poor quality samples, which are:

- Extreme wind speed values;
- Same wind speed for extended periods of time;
- Same wind direction on several subsequent measurements;
- Sectors with large wind gradient exponents, related to abrupt changes in wind speed between two measurement heights.

The quality control second step has required single case verification of suspect values. Suspect data were either maintained or discarded based on the knowledge of the wind resource pattern and local weather conditions. Therefore the outliers were removed. Despite of that, the Site A had the system operating for approximately 93% of the time and the LiDAR deployment with 61% of the data available to analyze. The Site B achieved a Met Mast recovery data around 76%, while the LiDAR presented the average recovery of 74% of the available data.

4.2 WIND ROSE

Attaining a valid data set of the wind direction during the period of production is very important due to the large variation in wind farm production over just a few degrees. Wind rose diagrams help to visualize the site wind patterns, being the most common instrument to display wind data in terms of either wind velocity distribution or frequency distribution.

This work analyzed both wind roses (wind speed and frequency distribution) through the Windographer² software.

² Windographer - Wind Resource Assessment Software, www.windographer.com

4.3 WIND SPEED DISTRIBUTION

Since one of the goals of this study is the evaluation of the influence of the wind characteristics parameters on wind turbine performance, sets of wind profiles samples were required. Therefore, the statistical analysis of wind speed was performed with several sets of wind profiles, considering the diurnal variation of wind characteristics in terms of frequency and wind speed distribution. The wind profile sets were produced through LiDAR measurements, in order to assess the importance of wind shear and stability on power production.

The Weibull distribution was applied for wind speed analysis, in which the parameters k and c represent the dimensionless shape parameter and the scale parameter (ms^{-1}), respectively. 10-min wind speed averages obtained by Galion LiDAR were the input for wind analyses. The k and c parameters of Weibull's distribution were obtained through the wind velocity Least Squares Technique (LST).

The Weibull distribution density function for $u \geq 0$ is given by the equation:

$$f(u) = \left(\frac{k}{c}\right) \left(\frac{u}{c}\right)^{k-1} \exp \left[-\left(\frac{u}{c}\right)^k \right], \quad (4.1)$$

where $f(u)$ is the wind velocity probability density function, k is the dimensionless Weibull's shape parameter and c is the Weibull's scale parameter in units of velocity (for instance, Spera, 1998).

Then the Weibull cumulative distribution function, for $u \geq 0$ is:

$$F(u) = 1 - \exp \left[-\left(\frac{u}{c}\right)^k \right]. \quad (4.2)$$

4.4 WIND ANALYSIS PARAMETERS FOR SITE A

The parameters selected to understand how wind characteristics can affect power generation were: wind shear, turbulence intensity and power performance, which were discussed in the following sections.

4.4.1 WIND SHEAR

The dimensionless wind shear exponent (Chehouri et al., 2015) was estimated from wind speed at two heights, 1 and 2, using the simple power law of equation (4.3):

$$V_2(z) = V_1 \left(\frac{Z_2}{Z_1} \right)^\alpha, \quad (4.3)$$

where Z_2 and Z_1 are heights, in (m), above the ground level; $V_2(z)$ is the mean horizontal wind speed (ms^{-1}) at height Z_2 (m); V_1 is the horizontal wind speed (ms^{-1}) at the reference height Z_1 (m); α is the wind shear exponent.

The wind shear exponent is an indicator of atmospheric stability, but it is not a straightforward measure of stability (Wharton and Lundquist, 2010). Different wind shear exponents were calculated at three distinct heights of the LiDAR measurements, such heights were the bottom tip, hub height and the top tip of the wind turbine.

4.4.2 TURBULENCE INTENSITY

Turbulence intensity, obtained from straight measurements of horizontal turbulence fluctuations at the site, was also considered in this analysis. Turbulence measurements are frequently done by employing equipment placed within the flow, such as: either cup or propeller anemometers, sonic anemometers and LiDAR. The last was used in this study. The new version of 2017 of the International Electrotechnical Commission (IEC) standard for wind turbine power performance measurements, IEC 61400-12-1, accepts the LiDAR technology to measure hub height wind speeds in combination with the mast. Another detail to point out that the IEC demands the measurement of only wind

horizontal component, therefore the turbulence intensity can be analyzed from the horizontal component of the velocity.

Turbulence intensity involves straight measurements of horizontal turbulence fluctuations at the site and is estimated by the ratio of the standard deviation, σ , in (ms^{-1}) of the wind speed for a 10-minute period time step and the corresponding mean wind speed, \bar{V} , in (ms^{-1}) at the 80 m-height (Wharton and Lundquist, 2012):

$$TI = \frac{\sigma}{\bar{V}}. \quad (4.4)$$

4.4.3 POWER PERFORMANCE

Power performance parameters are estimated in order to assess differences between observed power curves and the wind turbine manufacturer power curve. The manufacturer power performance curve assumes standard atmospheric conditions.

Power curves from the manufacturer traditionally relate power to the hub-height wind speed. Since the last decade, studies have presented the advantage of considering a wind velocity representative of the whole rotor disk (Antoniou et al., 2007; Wagner et al., 2009; Kim et al., 2016; Kumer et al., 2016).

The power performance analysis is carried out through scatter plots to examine if the turbine is generating under or overpower. The wind characteristics parameters selected for the scatter plots are:

- Normalized power as function of wind speed;
- Normalized power as a function of wind shear coefficient;
- Normalized power as a function of turbulence intensity;

4.5 MODELING FOR SITE B

The quality assessment of wake models was developed for site B, in which the wake was measured. The wake profile data comprised the mean wind speed for every downstream distance, where each interval distance was normalized by the rotor diameter (D); the mean wind speed was normalized for each 1 ms^{-1} wind speed bin.

4.5.1 PARK WAKE MODEL

The PARK wake model, developed by Jensen (1983), models a gradually extending wake with a velocity deficit varying with distance, as depicted in Figure 9.

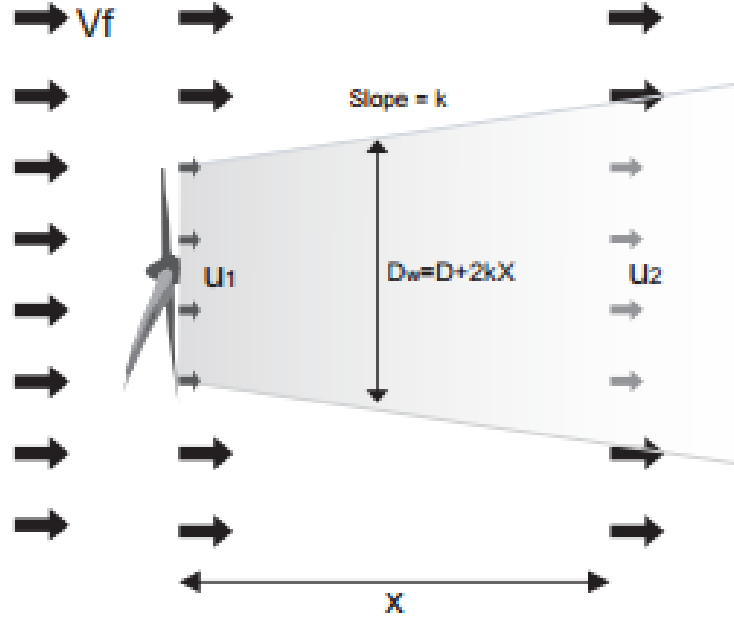


Figure 9: Schematic view of the PARK model wake expansion

First of all, the local atmospheric stability evaluation is required for model application. Atmospheric stability is a function of potential temperature; therefore, it requires the ratio of potential temperature gradient over the height gradient.

Potential temperature T_p is given by equation (4.5):

$$T_p = T \left(\frac{p_s}{p} \right)^\lambda, \quad (4.5)$$

where the T stands for absolute temperature, p is local pressure, p_s is the sea level pressure, which is equal to 1000 mb, and the exponent λ is equal to 0.286. After estimating the ratios $\Delta T_p / \Delta Z$ and computing their average, neutral atmospheric stability at the site can be assumed, if the average ratio is close to zero. Then one can apply the wake decay (k) equation (Peña and Rathmann, 2014; Frandsen, 1992):

$$k = \frac{1/2}{\ln(\frac{h}{z_0})}, \quad (4.6)$$

where h is the WTG hub height; z_0 is the surface roughness.

The wake width (D_w) is a function of rotor diameter (D), wake decay (k) and the downstream distance (x), according to equation (2.23)

$$D_w = D + 2kx. \quad (2.23)$$

The PARK model wake profile (PP) is a function of wake width (D_w), thrust coefficient (C_t) and rotor diameter (D), according to equation (4.7):

$$PP = 1 - \left[\left(1 - \left((1 - C_t)^{\frac{1}{2}} \right) \right) \right] \cdot \left[\frac{D}{D_w} \right]^2. \quad (4.7)$$

The thrust coefficient values are dependent on the power curve and should be retrieved for each inflow wind speed.

4.5.2 FRANDSEN WAKE MODEL

Frandsen et al. (2006) based their model on both mass and momentum conservation at the WTG control volume. The model assumed a top-hat shape for the wind speed deficit in the control volume. Then wake diameter of a single wake is given by equation (4.8),

$$D_w = D(\beta^{\frac{3}{2}} + \gamma x)^{\frac{1}{3}}, \quad (4.8)$$

where D_w is the wake diameter, D is the rotor diameter, x is the downstream distance in rotor diameter (D), γ is a non dimensional parameter dependent on C_t , which is computed through the equation (4.9),

$$\gamma = 1 - \sqrt{1 - C_t}, \quad (4.9)$$

and β that corresponds to the wake expansion parameter, which is determined as:

$$\beta = \frac{1 + \sqrt{1 - C_t}}{2\sqrt{1 - C_t}}. \quad (4.10)$$

The wind speed deficit in the wake is computed by the equation (2.24):

$$u = \frac{V_0}{2} \left(1 \pm \sqrt{1 - 2 \frac{A}{A_w} C_t} \right), \quad (2.24)$$

where u is the velocity deficit, V_0 is the freestream velocity, A_w is the cross-sectional wake area, A is the cross-sectional region just after the beginning of the wake expansion. Therefore, it is accepted that the downstream length of a rotor, which the wind demands to attain the pressure of the freestream is negligible, then to reach the pressure of the free flow is negligible, so A is considered to be the cross-sectional wake area at $x = 0$, which is the rotor area.

4.5.3 LARSEN WAKE MODEL

The model developed by Larsen (1988) simulate the wake through two parameters the wake width and the velocity variation behind the WTG. The Larsen simplified model can be considered as a first order solution, which main advantage is its straightforward implementation. Larsen assumed that the Prandtl's boundary layer theory was an adequate representation of the turbulent phenomenon after the WTG. As a first order approach, Larsen's Model takes into account just the dominant terms of the boundary layer expressions, assuming an incompressible fluid and steady flow.

The two main parameters of Larsen's model are: (1) wake radius (R_w), and (2) wind speed deficit inside the wake ($V_0 - u_x$), described by equations (2.26) and (2.25), respectively,

$$R_w = \left(\frac{35}{2\pi} \right)^{1/5} (3c_1^2)^{1/5} (C_t A (x + x_0))^{1/3}. \quad (2.26)$$

$$V_0 - u_x =$$

$$-\frac{V_0}{9} (C_t A (x + x_0)^{-2})^{1/3} \left\{ r^{3/2} (3c_1^2 C_t A (x + x_0))^{-1/2} - \left(\frac{35}{2\pi} \right)^{3/10} (3c_1^2)^{-1/5} \right\}^2, \quad (2.25)$$

where V_0 is the freestream velocity at rotor u_x is the wind velocity in the wake, A the rotor area, C_t is the thrust coefficient. The constant c_1 is associated to the Prandtl mixing length and is given by:

$$c_1 = \left(\frac{D_{eff}}{2}\right)^{5/2} \left(\frac{105}{2\pi}\right)^{-1/2} (C_t A x_0)^{-5/6}, \quad (4.11)$$

c_1 is a function of x_0 , which is the normalized position of the WTG:

$$x_0 = \frac{9.5D}{\left(\frac{2R_{9.5}}{D_e}\right)^3 - 1}. \quad (4.12)$$

The x_0 parameter is a function of the effective rotor diameter (D_e) and the wake radius at a downstream distance of 9.5 rotor diameters ($R_{9.5}$) from the hub, which was defined by EWTSII (1999) and given by:

$$R_{9.5} = 0.5[R_{nb} + \min(H, R_{nb})], \quad (4.13)$$

in which R_{nb} is defined by

$$R_{nb} = \max(1.08D, 1.08D + 21.7D(I_a - 0.05)), \quad (4.14)$$

The parameter D_e , in equation (4.12), is only function of the thrust coefficient (C_t), according to equation (4.15)

$$D_e = D \sqrt{\frac{1 + \sqrt{1 - C_t}}{2\sqrt{1 - C_t}}}. \quad (4.15)$$

4.5.4 EDDY VISCOSITY WAKE MODEL

The EDDY Viscosity Wake Model, described by Ainslie (1988), simulates the wake using numerical solutions to the governing differential equations with eddy viscosity turbulence closure. The differential equations, introduced at section (2.3.1.4), are numerically integrated using the Crank-Nicolson method. Since the goal is to estimate the velocity deficit at the centerline of the wake

expansion, a simplified solution of the EDDY Viscosity model is carried out. The boundary conditions were described in detail by Ainslie (1988). The boundary condition close to the hub is considered at two rotor diameters downstream of the wind turbine generator:

$$1 - \frac{u_1}{v_0} = D_m e^{-3.56 \left(\frac{r}{b}\right)^2}, \quad (4.16)$$

where D_m is the initial velocity deficit, r is the radius of the point of interest and b is the wake width (or radius).

D_m was experimentally estimated on wind tunnels and fitted to the equation (4.17):

$$D_m = C_t - 0.05 - (16C_t - 0.5) I_a / 1000, \quad (4.17)$$

in which I_a is the ambient turbulence intensity (%) and (C_t) the turbine thrust coefficient.

Based on momentum conservation, one obtains the relation between velocity deficit and thrust coefficient, which yields equation (4.18) for, b , the wake width (or wake diameter):

$$b = \sqrt{\frac{3.56 C_t}{8 D_m (1 - 0.5) D_m}}. \quad (4.18)$$

The model assumes that the wind speed deficit is self-similar, following an Gaussian curve with its peak located at the wind turbine axis (Ainslie, 1988), starting at two rotor diameters downstream of the hub. Solution of the above system of equations yield self-similar wake profiles for all distances downwind; in other words the initial Gaussian shape is preserved and only its width and the corresponding centerline velocity deficit change with downwind distances. As the wake width is related to the wake deficit through conservation of momentum, one is left with only the wake centerline velocity deficit to solve for.

Taking into consideration only the centerline velocity deficit u_c , for $r = 0$, equation (4.16) becomes:

$$u_c = V_0 (1 - D_m) \quad (4.19)$$

Substitution of both equations (4.19) and (2.26) into equation (2.29) and noting that the only requirement is to solve for the centerline velocity, one obtains:

$$\frac{\partial u_c}{\partial x} = 16\varepsilon \frac{(u_c^3 - u_c^2 - u_c + 1)}{u_c C_t} \quad (4.20)$$

Therefore, the eddy viscosity (ε) is determined by:

$$\varepsilon = F (0.015b(V_0 - u_c) + K_m) \quad (4.21)$$

$$K_m = \kappa^2 \frac{I_a}{100}, \quad (4.22)$$

where κ is the Von Karman constant, I_a is the ambient turbulence, which can be computed as a percentage, b is a measure of the wake width and x is normalized by rotor diameters (D).

Parameter F in equation (4.21) varies with x according to the equation

$$\begin{cases} F = 1 \text{ for } x \geq 5.5 \\ F = 0.65 + \left(\frac{x-4.5}{23.32}\right)^{\frac{1}{3}} \text{ when } x < 5.5 \end{cases} \quad (4.23)$$

Equation (4.20) is a first order ordinary differential equation that can be solved efficiently using a numerical integration scheme such as Runge Kutta.

4.5.5 WAKE NUMERICAL SIMULATION USING CFD

In this study the wind turbine wake simulation has used the concept of the actuator disc in CFD (Computational Fluid Dynamics) assuming a flat terrain geometry. The implementation had been applied in the Fluent software (ANSYS®, 2017) due the student free license that ANSYS® provided for a period of time. The Reynolds Averaged Navier Stokes (RANS) equations were solved with a two differential equation model for the turbulent viscosity. Turbulence was

closed by the $k - \varepsilon$ model, which solves two differential equations for turbulent kinetic energy, k , and for dissipation rate, ε . The characteristic velocity is represented by \sqrt{k} , meanwhile the characteristic length, l , is obtained through equation (4.24) function of advective energy production and dissipation rate:

$$l = \frac{k^{3/2}}{\varepsilon} . \quad (4.24)$$

The turbulent viscosity is represented by equation (4.25):

$$\mu_t = \rho l \sqrt{k} . \quad (4.25)$$

Then substituting equation (4.24) into equation (4.25), and utilizing a constant, C_μ , the equation can be written as:

$$\mu_t = C_\mu \frac{\rho k^2}{\varepsilon} . \quad (4.26)$$

This study has implemented CFD simulations of the wake for a single turbine on a flat terrain. The wind turbine rotor was modeled by an actuator disc with porous jump sponge, supporting a resisting force which was computed from the thrust coefficient of the wind turbine generator. Therefore, a wake was simulated downstream of the wind turbine generator, with the wake velocity deficit and corresponding turbulence.

4.5.6 WAKE MODELS ACCURACY

The performance assessment of the wake models in comparison to the Galion LiDAR data used the root mean square error statistic (RMSE), according to equation:

$$RMSE = \sqrt{\frac{\sum_{i=1}^n (y_i - x_i)^2}{n}} , \quad (4.27)$$

where, y_i is the measured data in a certain bin; x_i is the model output and n is the number of bins.

The lowest RMSE value is associated with the most accurate wake model.

5 RESULTS AND DISCUSSION

This chapter reports first the Site A results, focusing on the analyses of wind and power generation, followed by the Site B results, focusing on the wake modeling analysis.

5.1 WIND AND POWER GENERATION ANALYSES FOR SITE A

The next sub-sections report site A's results; beginning with a description of the atmospheric field conditions, followed by the investigation of the wind shear ranges. The intercomparison of turbulence, presented in terms of power curves, is discussed at the end of this section.

5.1.1 ATMOSPHERIC AND WIND CHARACTERISTICS AT SITE A

Both, the data collected by the LiDAR, and the meteorological mast were used as an input to the Windographer software, in order to describe the wind attributes over the Site A field campaign.

The mean wind velocity from the LiDAR dataset was 7.76 ms^{-1} . The dominant wind direction was 139° corresponding to the southeastern quadrant. The mean temperature was 21°C , associated with a mean air density of 1.221 kgm^{-3} , which was a little higher than the normal temperature and pressure at sea level (20°C). The variables measured by LiDAR and the meteorological mast are presented on Table 1.

Table 1: Mean wind and meteorological parameters at Site A

Parameters	Unit	Value
Mean wind speed	(ms^{-1})	7.8
Wind speed standard deviation	(ms^{-1})	3.0
Maximum wind speed	(ms^{-1})	19.5
Mean wind direction	$(^\circ)$	138.7
Mean temperature	$(^\circ\text{C})$	20.9
Mean air density	(kgm^{-3})	1.221

The wind temporal variability is shown in Figure 10, through the comparison of the wind velocity histogram with the fitted Weibull distribution.

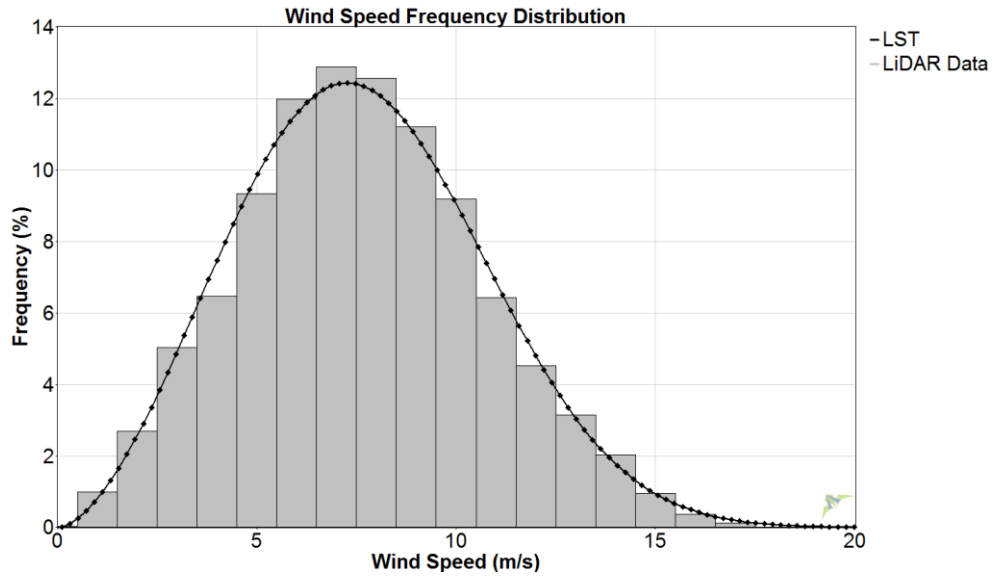


Figure 10: Wind velocity distribution at Site A

The Weibull fit produced by the Windographer software is based on the Least Squares Technique (LST); where the two parameters of the Weibull distribution (k is the shape parameter and c is the scale parameter) are fitted to the measured velocity histogram. The shape parameter was $k=2.70$ and the scale parameter was $c=8.63 \text{ ms}^{-1}$.

The wind rose obtained from LiDAR measurements data is shown in Figure 11.

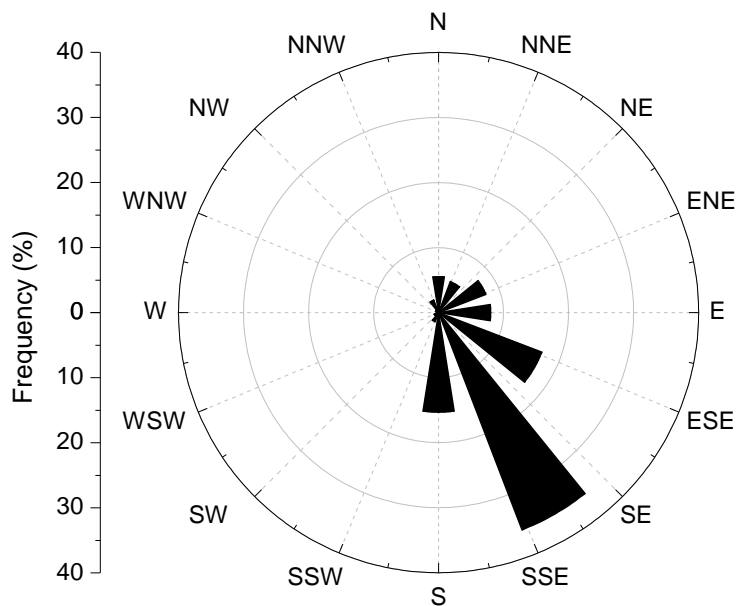


Figure 11: Wind rose for Site A

Winds from the southeast sector were dominant, corresponding to 78% of the events. The highest frequency was 35% for the 150° direction, followed by 15% for 120° and 180° directions.

5.1.2 WIND SHEAR

The wind shear coefficients (α) were determined according to the equation (4.3) for three different heights, corresponding to the 32.5, 80 and 127.5 m above ground, which yielded the event mean shear coefficient. Such coefficients have been binned in six ranges in order to have enough data to plot the power performance. Those ranges are presented in Table 2, alongside to the number of occurrences and the median wind shear.

Table 2: Wind shear ranges for Site A

Wind Shear Bin	Number of Occurrences	Median Wind Shear
< 0.0	1655	-0.053
0.0 to 0.1	6806	0.059
0.1 to 0.2	4701	0.144
0.2 to 0.3	3563	0.246
0.3 to 0.4	2668	0.346
> 0.4	2782	0.483

As seen from the table, the band with the lowest number of events corresponded to $\alpha < 0$ and the range with the largest number of events corresponded to [0.0 - 0.1] bin, which means that most events had low wind shear values. Such density of data counts for each range of wind shear can also be seen at Figure 12, which depicts scatter plots of the power generation curves over the wind speed at the hub height for distinct band of wind shear exponents.

Figure 12 also show that the events are concentrated on lower wind speeds. Most of the high wind speeds ($V > 14 \text{ ms}^{-1}$) produced shear coefficients in the [0.1 - 0.2] range, whereas the negative shear coefficient has almost not occurred for high speed winds.

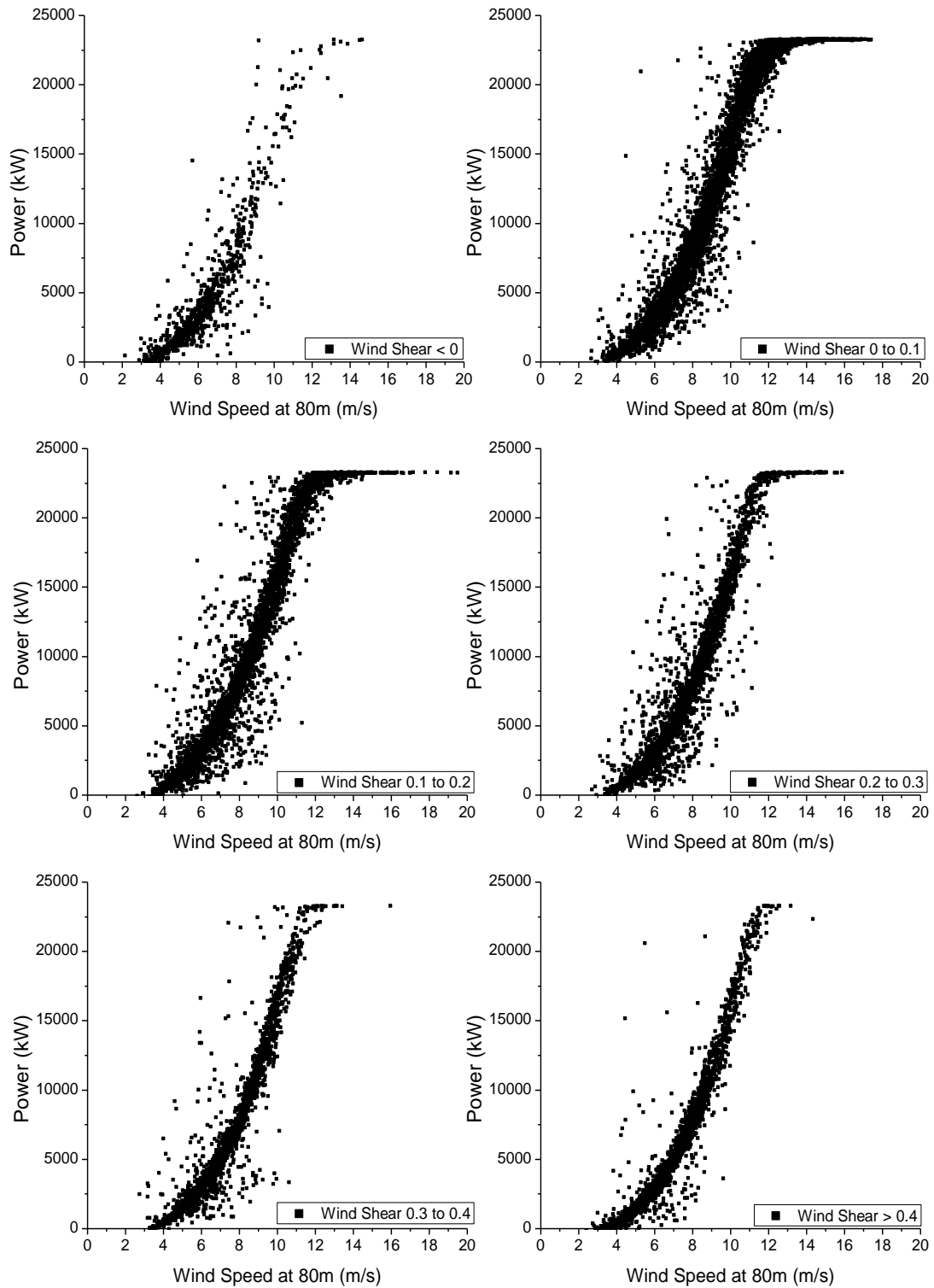


Figure 12: Power curve scatter plots for wind shear ranges

Figure 13 is the wind speed histogram conditioned on wind shear coefficients, which was designed to enhance the understanding of the wind shear coefficients behavior for different wind speeds.

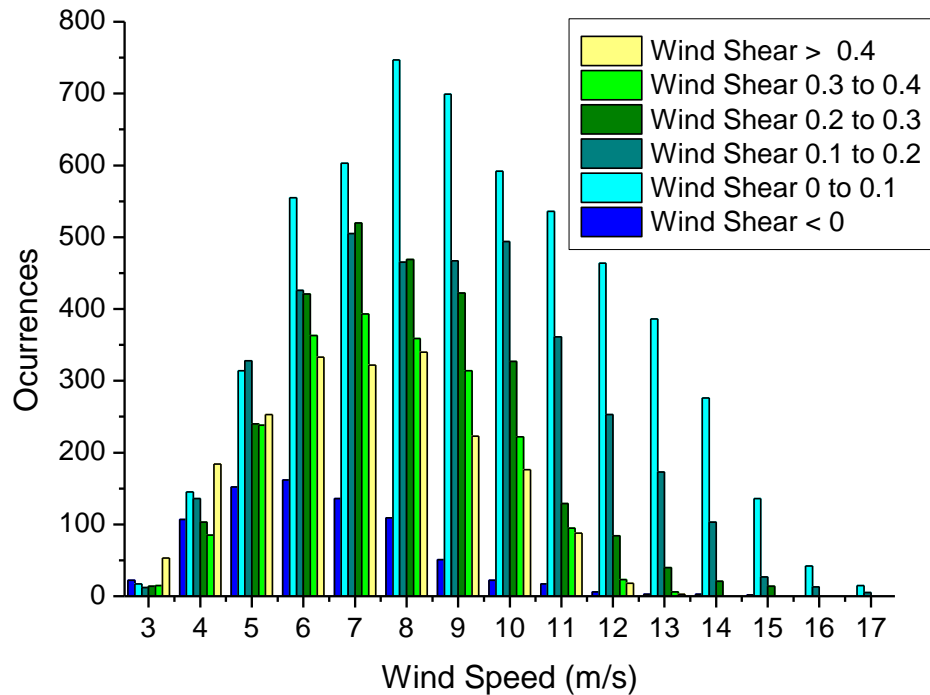


Figure 13: Wind speed histogram conditioned on wind shear coefficients

The wind speed bins of 5 to 10 ms^{-1} , comprised 65% of the events, which were mostly associated with the [0.0 - 0.1] shear coefficient range. The largest shear coefficients [>0.4] were registered mostly for the 6 to 8 ms^{-1} wind speeds, whereas they were almost not registered for speeds over 12 ms^{-1} .

Finally, Figure 14 compares how the power curve varies with respect to wind shear. Large shear coefficients reduce power production for wind speeds lower than 10 ms^{-1} , and enhance power production for wind speeds on the 11-13 ms^{-1} range. The negative shear range underestimates power production for 11 ms^{-1} winds, while shear greater than 0.4 seems to overestimate the power production.

Therefore, the wind shear range of [0.0 - 0.1] was taken as the power curve base, due to the highest data counts in general and its better representation for every single wind speed bin.

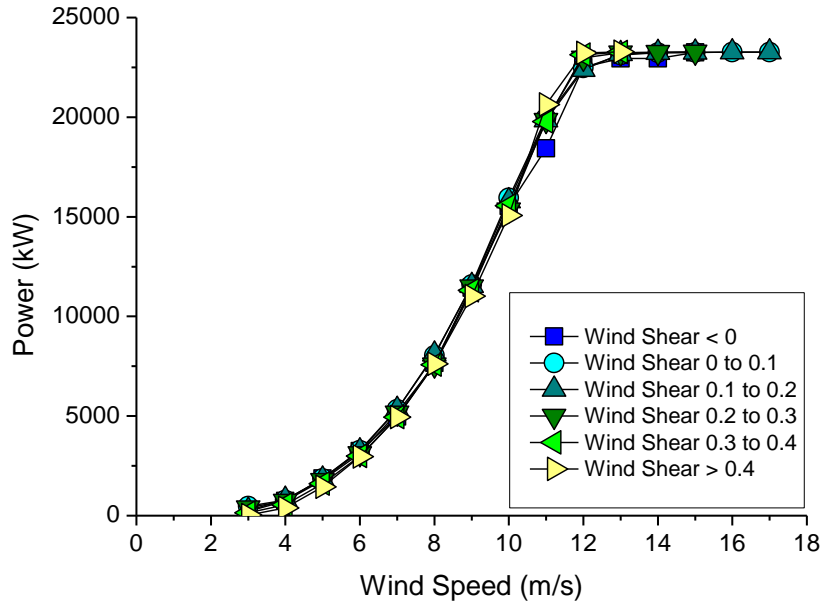


Figure 14: Power curve conditioned on wind shear coefficients

In addition, for wind speeds higher than 3 ms^{-1} , the power curve conditioned on negative shear performed similarly to the base curve. However, wind shear ranges of $[0.3 - 0.4]$ and $[>0.4]$ displayed two wind speed bins in which there was at least 14% power underestimation with respect to the base curve. Both bins, at lower wind speeds of 4 and 5 ms^{-1} , were associated with power underestimation of 30% and 14%, respectively, for shear between $[0.3 - 0.4]$, and power underestimation of 50% and 23% respectively for wind shear coefficients $[>0.4]$.

5.1.3 TURBULENCE INTENSITY

Turbulence intensity can be estimated as a function of the wind temporal variability, through its standard deviation, according to equation (4.4). Kaiser *et al.* (2007) stated that as velocity oscillates around the rated velocity, the power output is restricted to the rated power. Power oscillation occurs only when the instantaneous velocity gets below the rated velocity. As a consequence, for a certain time interval in which the power produced with a certain degree of turbulence intensity is typically lower than the power output with hypothetical turbulence intensity equals to 0%, for the same wind speed.

Figure 15 compares the power curve variability with respect to turbulence intensity (TI) ranges.

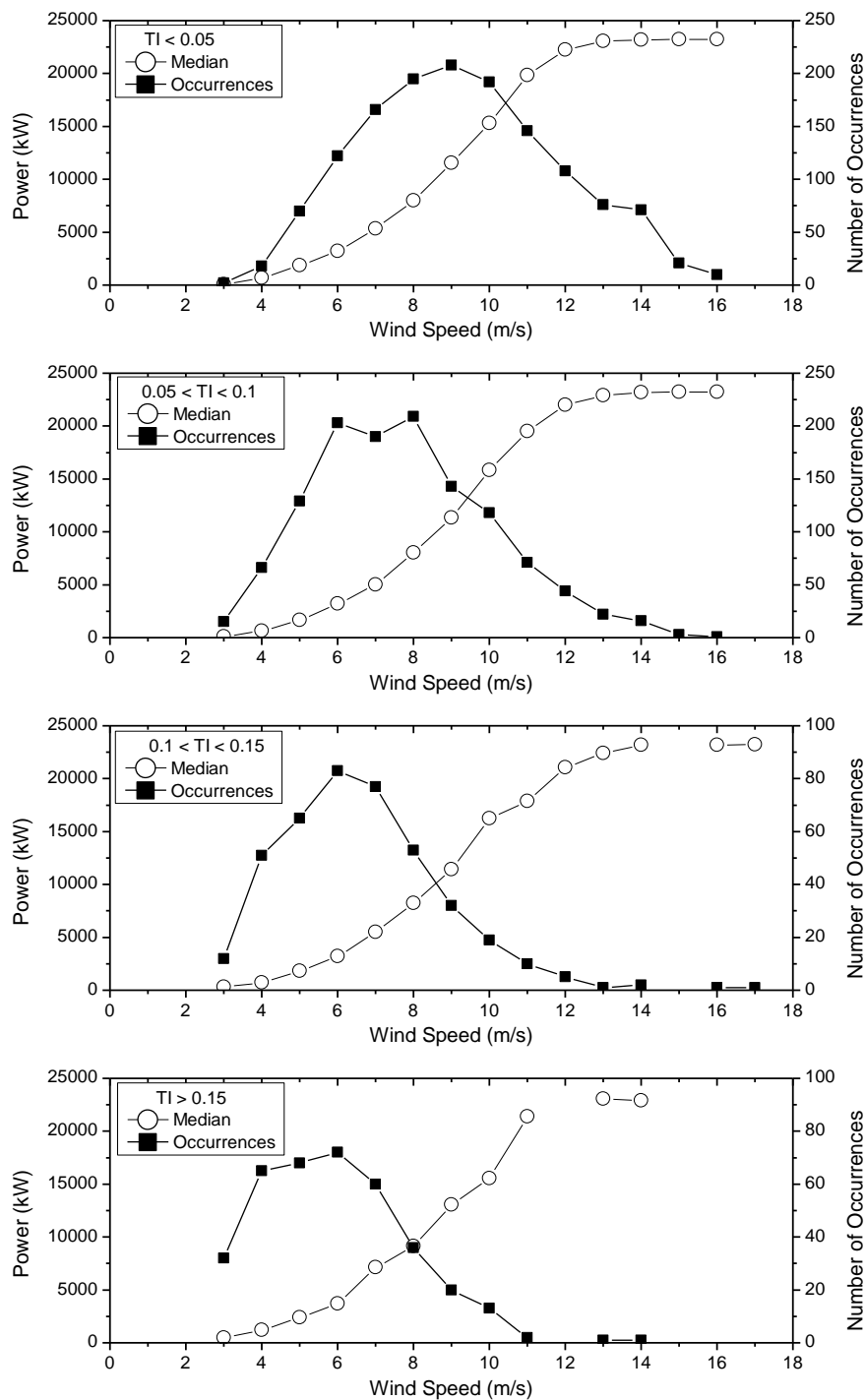


Figure 15: Variability of power curves with respect to turbulence intensity (TI)

Table 3 summarizes the statistics of turbulence intensity ranges used in Figure 15.

Table 3: Turbulence intensity statistics

TI range	Number of Occurrences	Median TI
< 0.05	1405	0.033
0.05 to 0.1	1230	0.070
0.1 to 0.15	412	0.121
> 0.15	370	0.200

Figure 15 and Table 3 show that low turbulence events occur more often (77% of time) than high turbulence events (23% of time).

Figure 16 shows the wind speed histogram conditioned on turbulence intensity for four turbulence ranges.

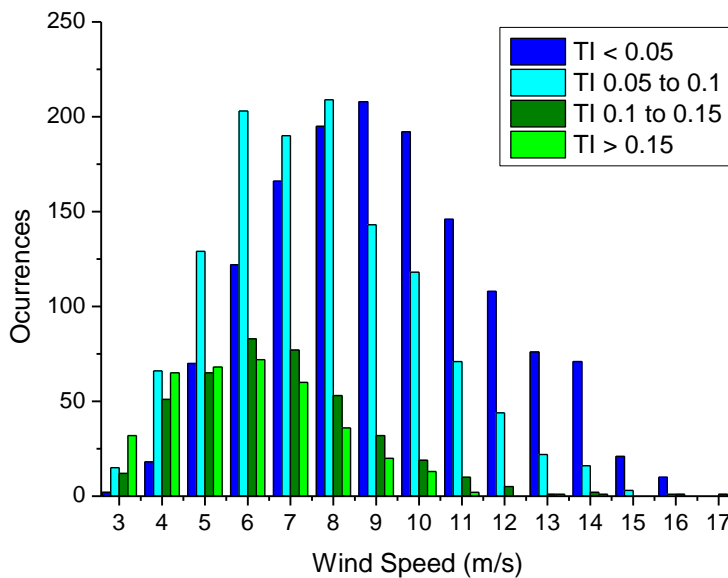


Figure 16: Wind speed histogram conditioned on turbulence intensity

High velocities are associated with low turbulence, as one can see for the wind speed bins from 9 to 17 ms^{-1} , in which TI lower than 0.05 is dominant. Low velocities are associated with enhanced turbulence intensity, shown by [0.05 - 0.10] dominant events for wind speed bins from 4 to 8 ms^{-1} . High turbulence events TI [>0.15] were registered only for the 3 to 10 ms^{-1} velocity range.

Lastly, Figure 17 depicts the power curves conditioned on turbulence intensity, in order to assess the effect of turbulence intensity on power output.

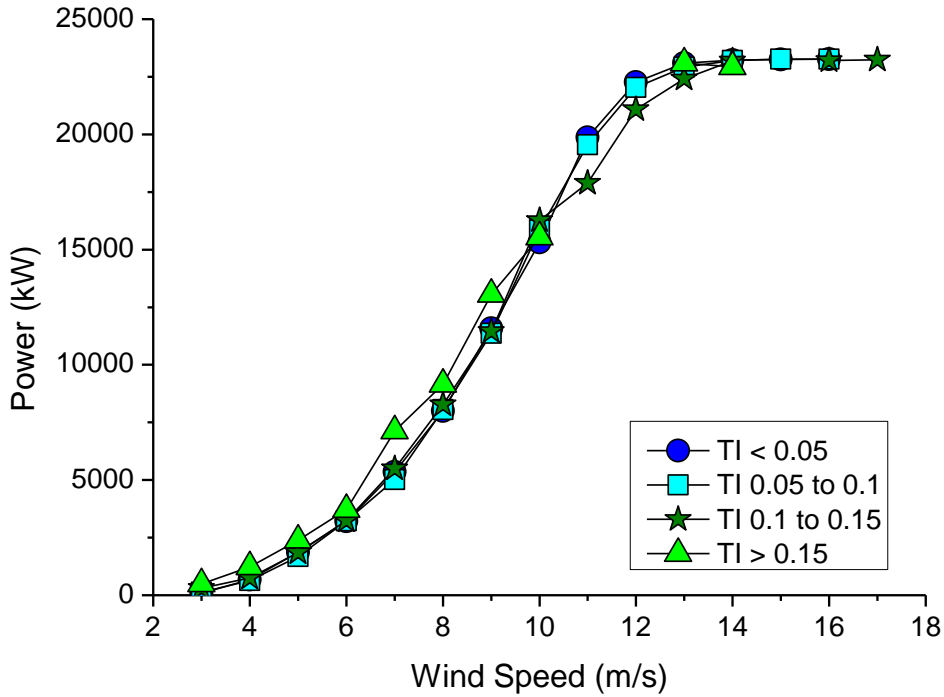


Figure 17: Power curves conditioned on turbulence intensity (TI)

The power curve base was assumed as the one obtained for turbulence intensity lower than 0.05, which is dominant for a wide velocity range.

For wind velocity ranging from cut in to 10 ms^{-1} the power output is enhanced by turbulence intensity. However, the power output drops with high turbulence intensities, for high wind speeds ($V > 10 \text{ ms}^{-1}$). It is important to point out that there were no events of TI [> 0.15] for the 12, 15, 16, 17 ms^{-1} wind speed bins. Also at the 17 ms^{-1} wind speed bin there were no events for the TI [< 0.05] and [0.05 - 0.1] ranges.

For the wind speed bin of 7 ms^{-1} and turbulence intensity greater than 0.15 the power output exceeded in 33% to the base curve. However, for the 11 ms^{-1} wind speed bin the power for high turbulence [0.1 – 0.15] underestimates more than 10% the base power.

Therefore increasing turbulence intensity the power output is overestimated at moderate wind speeds and underestimated at greater than 10 ms^{-1} wind speeds, in agreement to Langreder *et al.* (2004). The only exception for that occurred at 11 ms^{-1} to [> 0.15] turbulence intensity range, which is attributed to the low data count at the range.

5.2 WAKE MODELING ANALYSIS FOR SITE B

The following sub-sections have reported the results for Site B's field campaign and wake modeling. Initially there is a description of Site B's wind and meteorological data. After that, a sub-section with the inputs estimation for the simplified wake models, followed by a CFD model configuration sub-section. Next, the comparison of wake models against LiDAR data was presented. At the end, the accuracy of the wake models was analyzed in terms of RMSE.

5.2.1 METEOROLOGICAL MAST DATA CHARACTERISTICS FOR SITE B

The data obtained by the meteorological mast was used as input to the Windographer software, which produced the wind characteristics (wind mean, frequency distribution and wind rose) for the campaign period.

The mean wind speed at 80m from the meteorological mast data was 5.1 ms^{-1} , whereas the operational wind speed range of the WTG varied between 4 ms^{-1} (cut in) to 25 ms^{-1} (cut off). During the field campaign the largest wind speed was 24.1 ms^{-1} , although wind speeds below 15 ms^{-1} occurred 99.9% of the campaign. The dominant wind direction was 183° , representing the southern sector. The mean temperature was 15.3°C .

Table 4 summarizes the statistics of the variables measured by the sensors of the meteorological mast.

Table 4: Meteorological mast variables

Parameters	Unit	Value
Mean wind speed	(ms^{-1})	5.09
Wind speed standard deviation	(ms^{-1})	0.64
Wind speed variance	$(\text{m}^2\text{s}^{-2})$	0.41
Maximum wind speed	(ms^{-1})	24.1
Mean turbulence intensity		0.13
Mean wind direction	$(^\circ)$	183.2
Mean temperature	$(^\circ\text{C})$	15.3
Mean pressure	(kPa)	83.94
Mean air density	(kgm^{-3})	1.21

The histogram of the meteorological mast wind speed and the fitted Weibull distribution are presented in Figure 18. The Weibull fit used the maximum likelihood algorithm to estimate the two parameters of the distribution function, namely: shape parameter, k , and the scale parameter, c .

The estimated shape parameter was $k=1.30$, which indicates an asymmetrical distribution, skewed toward low wind velocities.

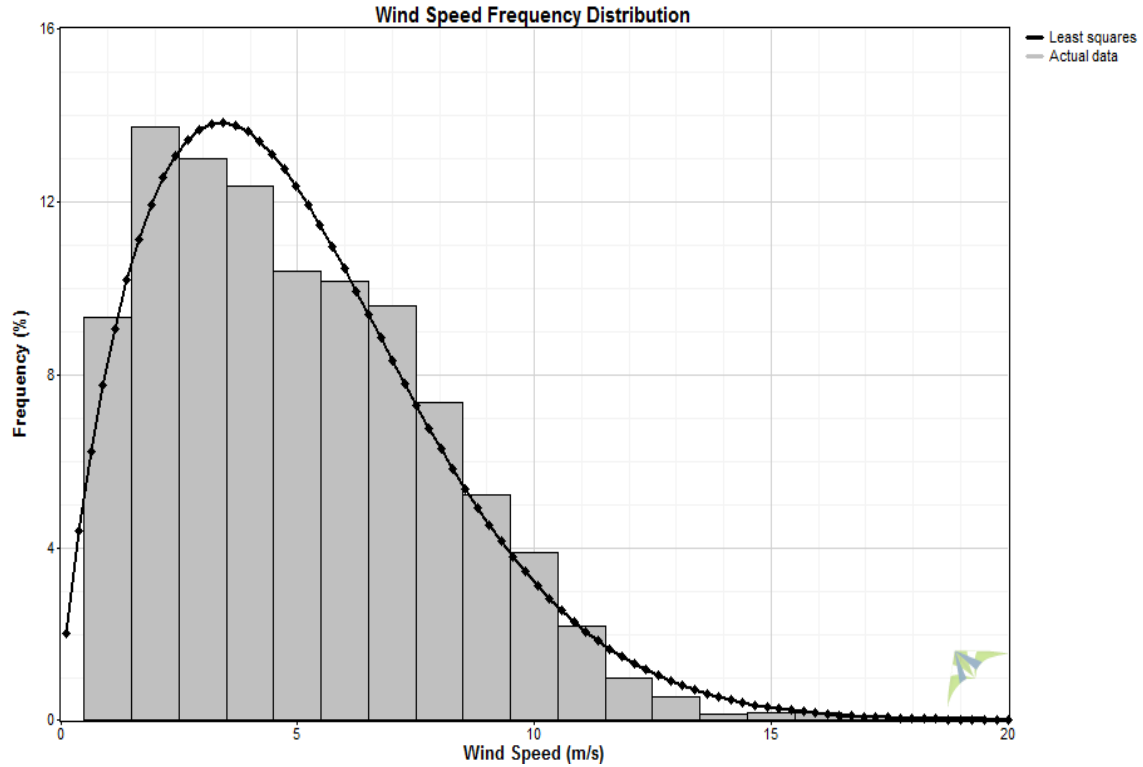


Figure 18: Wind speed histogram and fitted Weibull distribution for site B

The Weibull scale parameter was $c = 5.04 \text{ ms}^{-1}$. Increasing c , the distribution peak moves to the right and the peak magnitude also declines.

Figure 19 depicts the wind rose obtained from the met mast dataset. Winds from the southern sectors were prevalent, dominating 65% of the occurrences, which attended the wind direction requirement for LiDAR measurements that ranged from 90° to 270° . Southern winds frequency reached 70% of the sample, for winds above the cut in velocity (4 ms^{-1}).

Once the wind data from the meteorological mast were analyzed, the dataset was used as initial and boundary conditions for wake modeling. The parameter used as the model inflow condition was the freestream wind speed.

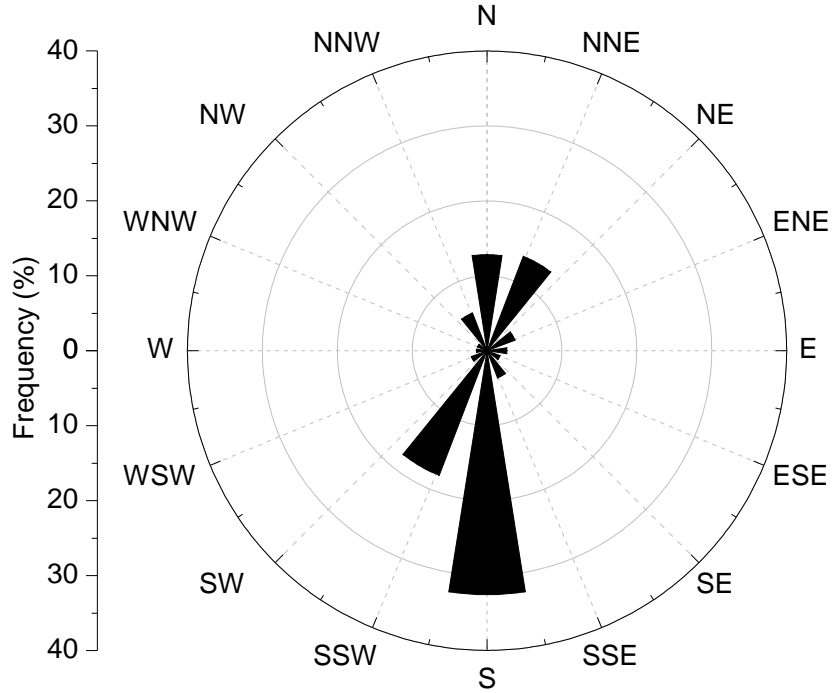


Figure 19: Wind rose for the meteorological mast data of Site B

5.2.2 LIDAR DATA CHARACTERISTICS FOR SITE B

For the wake modeling simulations, the inflow conditions were chosen for 1 ms^{-1} bins, within the range of interest varying from 5 ms^{-1} to 12 ms^{-1} . The downstream distance, x , was normalized by the rotor diameter, D . The wake diameter, D_w , was normalized by D , as well. The wake characteristics are shown in x - y graphical format, in which the vertical axis represents the normalized freestream velocity recovery (also named as velocity deficit). The horizontal axis shows the downstream distance behind the wind turbine in the wake centerline.

Before presenting the comparison between wake models and LiDAR measurements,

Figure 20 points out LiDAR results for the freestream velocity recovery on the wake centerline. The plots show the median values as small circles and the bars show bin data scattering (usually named as error bars). Each bar corresponds to ± 1 standard error for the bin sample.

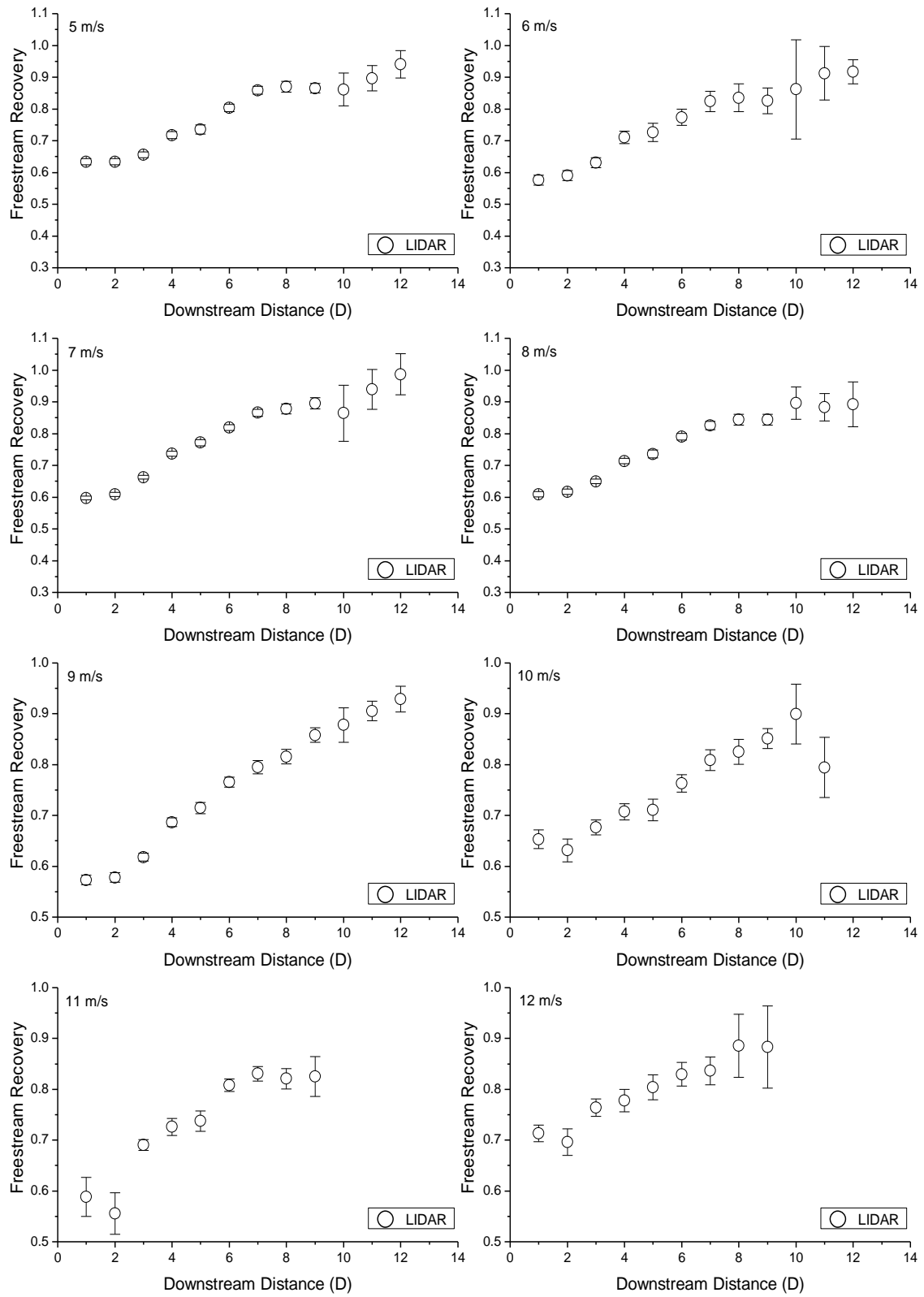


Figure 20: LiDAR centerline velocity recovery for 5 to 12 ms^{-1} freestream bins

Velocity at the downstream distance of one diameter from the hub varied from 0.55 to 0.70 of the freestream velocity, and it has taken a downstream distance of six diameters to recover 0.80 of the freestream velocity.

High velocity recovery variability has started at the downstream distance of ten rotor diameters, for freestream velocities ranging from 5 ms⁻¹ to 10 ms⁻¹. Increasing the freestream velocity to either 11 ms⁻¹ or 12 ms⁻¹, the velocity recovery variability has started at the distance of eight rotor diameters.

The variation of the freestream velocity recovery over the wake cross-section has been analyzed for three cross section locations, corresponding to downstream distances of 500 m (Figure 21), 700 m (Figure 22) and 1000 m (Figure 23).

For all three cross sections 21 points have been chosen, being one point in the centerline and ten points on each side of the centerline. The cross section points were equally spaced, with 20 m between adjacent points. The total cross section width corresponded to 400 m, took into consideration the LiDAR quality recovery, which began to have lower recovery over 400 m width.

The last section, which is at 1000 m downstream of the wind turbine is marked by low LiDAR data counts. For instance, although the cross section sampled 21 points, there were data counts in only 16 points for the 5, 8, 9 ms⁻¹ bins, 15 points for 6 and 7 ms⁻¹ bins, 14 points for 10 ms⁻¹ bin, 11 points for 11 ms⁻¹ bin and by the end only one point at 12 ms⁻¹ bin.

The reason for that could be attributed to LiDAR limitations to acquire high velocities at distances farther than 1000 m. Adding that the Galion was deployed during a low wind speed period which will impact on the validity of the results, suffering range issues due to low aerosol content.

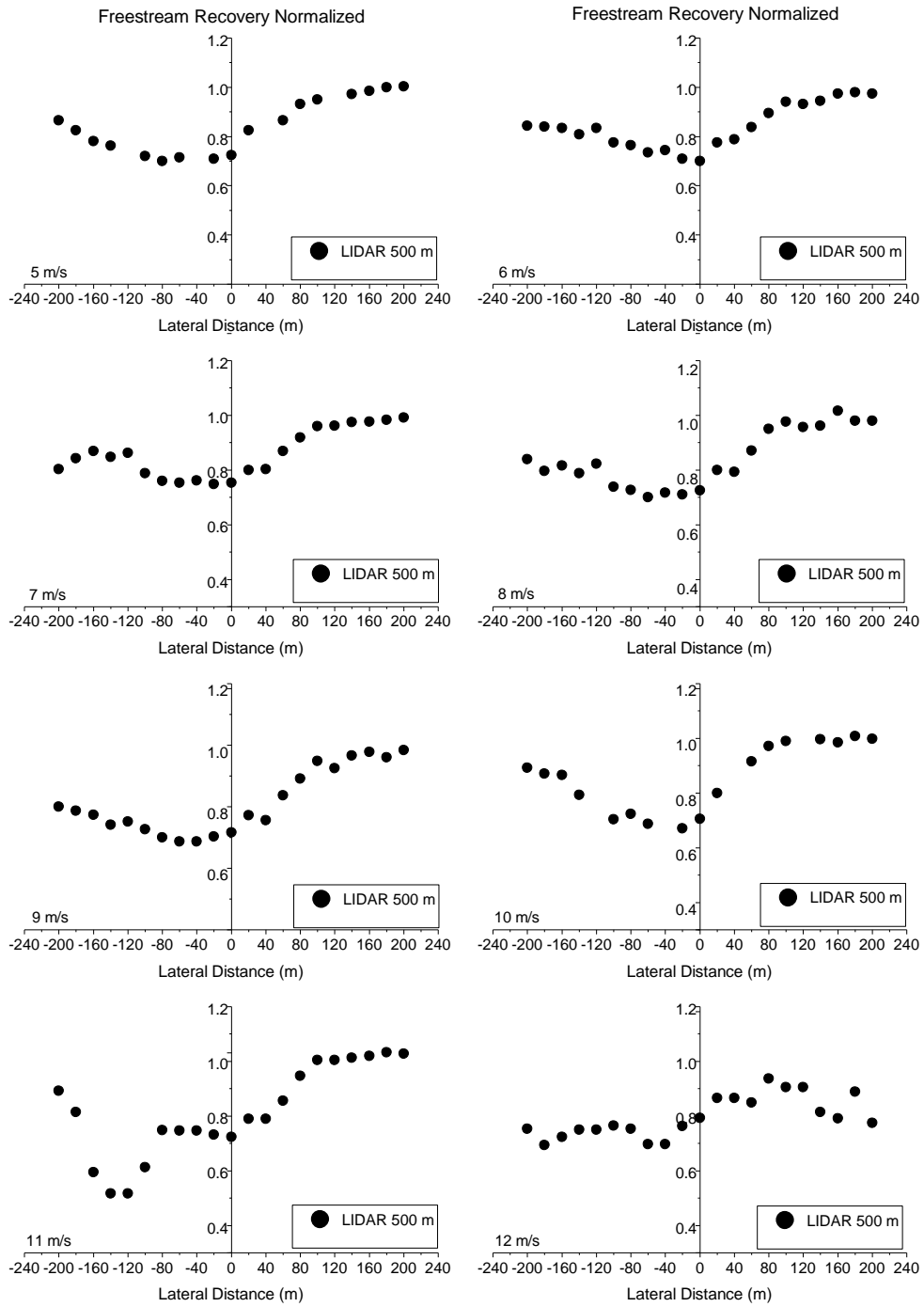


Figure 21: LiDAR 500 m cross section velocity recovery for 5 to 12 ms^{-1} freestream bins

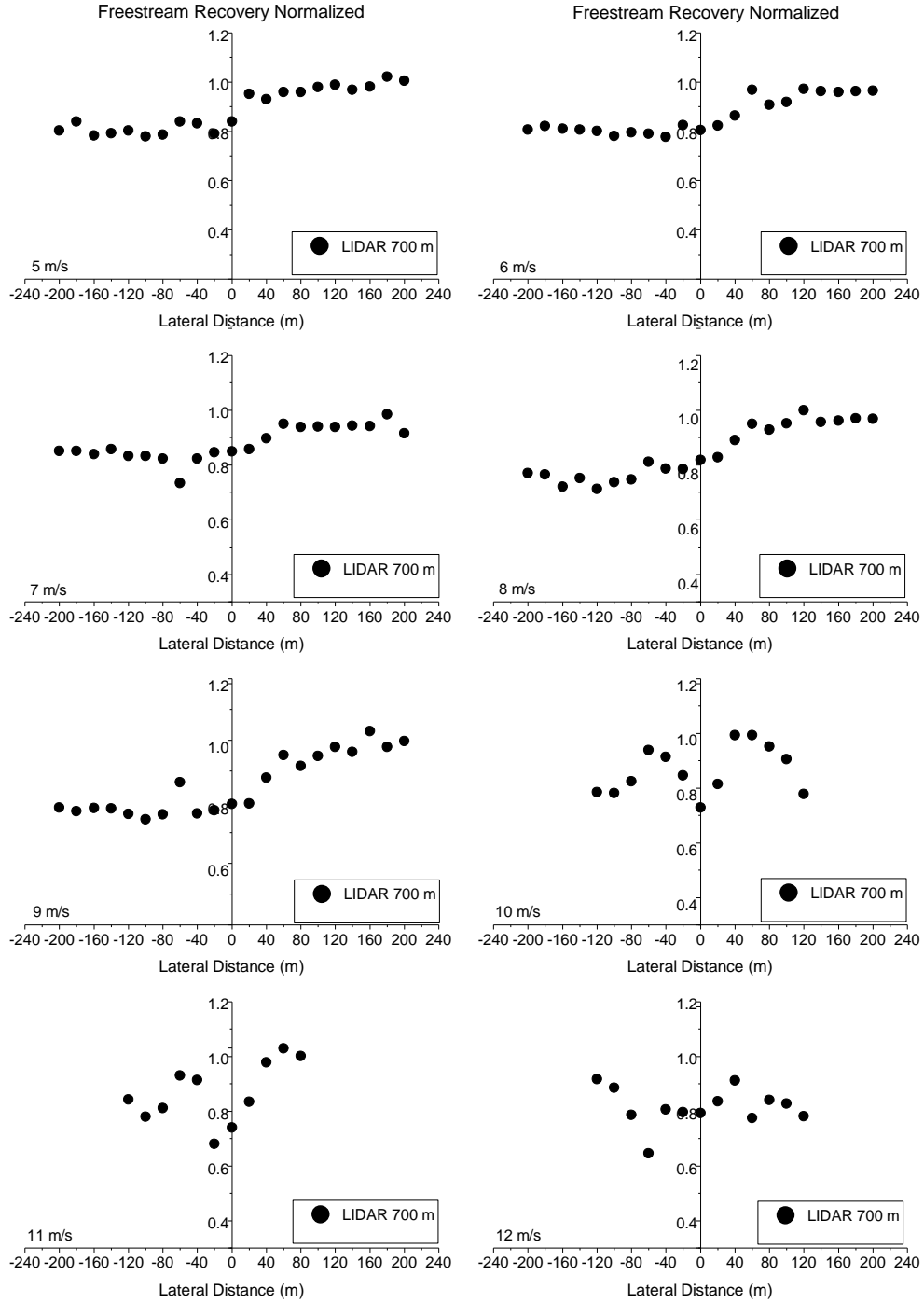


Figure 22: LiDAR 700 m cross section velocity recovery for 5 to 12 ms^{-1} freestream bins

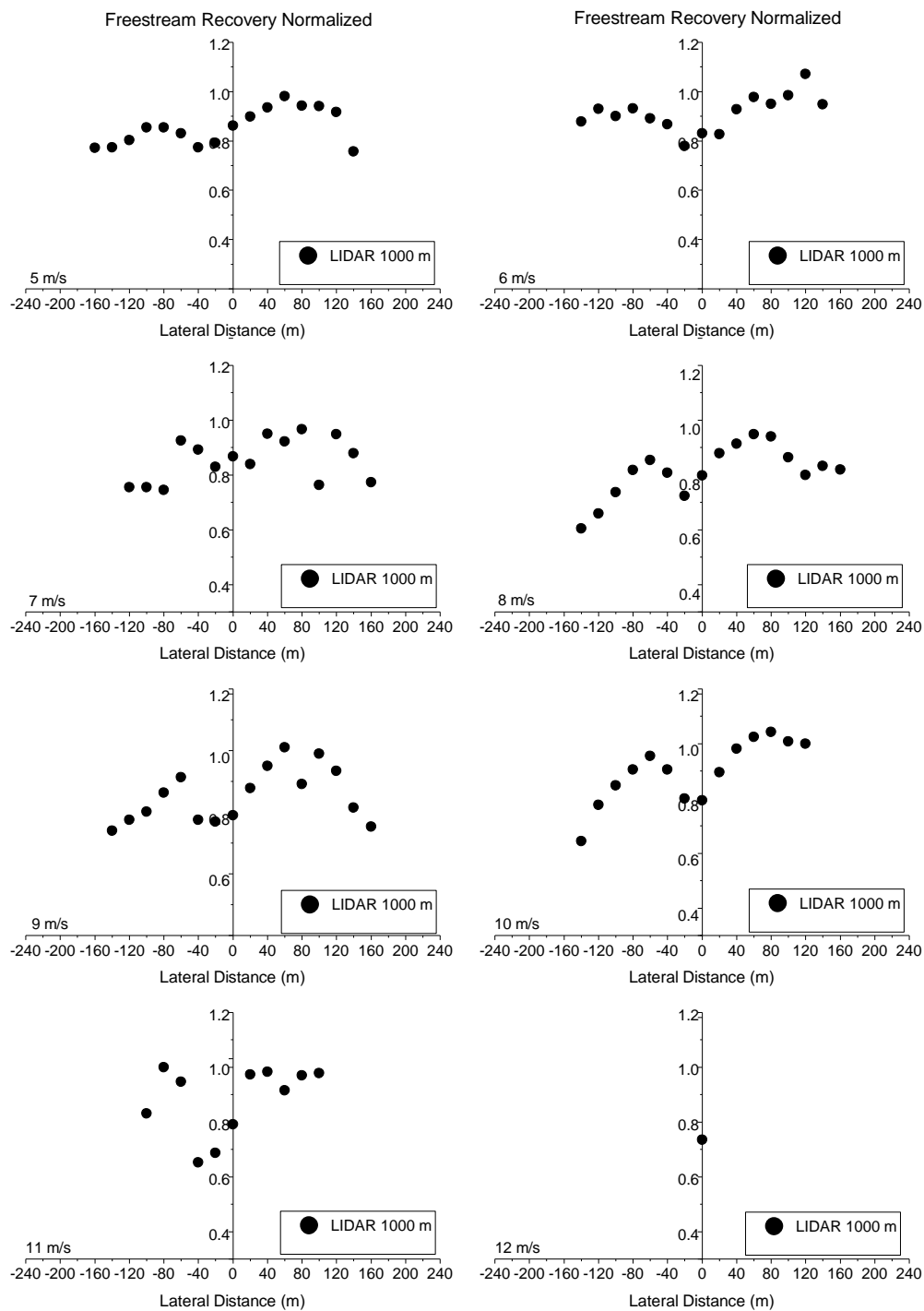


Figure 23: LiDAR 1000 m cross section velocity recovery for 5 to 12 ms^{-1} freestream bins

5.2.3 SIMPLIFIED WAKE MODELS PARAMETERS

In this section, the parameters of the four simplified models selected for this study were defined and computed to be used as model inputs. It is pointed out that the models which use parameters derived from thrust coefficients have such parameters omitted due to contractual restrictions of the data provider.

The PARK model considers the wake decay constant (k), through the equation (4.6), in which $h = 80$ m, $z_0 = 0.03$ m for open flat terrain (WMO, 2008) and $\omega = 0.5$ (SgurrEnergy, 2012), resulting in $k = 0.063$ and considering $D = 99$ m. The FRANDSEN model required the parameters: $D = 99$ m, therefore the swept area $A = 7697.7$ m². The model parameters γ and β are based on the thrust coefficient for each wind speed bin; therefore, their values cannot be presented. The LARSEN model required the parameters: $z_0 = 0.03$ m (WMO, 2008), $D = 99$ m, $A = 7697.7$ m², $I_a = 0.13$, $R_{nb} = 278.8$ m, $R_{9.5} = 179.4$ m, $D_{eff} = 128.3$ m, $x_0 = 45$ m and $c_1 = 0.23$. The thrust coefficients, for each wind speed bin, were not presented. The EDDY VISCOSITY model parameters are: $\kappa = 0.40$ and $I_a = 0.13$, then D_m and b could not be presented. Table 5 summarizes the model parameters of the simplified models.

Table 5: Parameters of the simplified models

Model Parameter	Value	Unit
z_0	0.03	m
ω	0.5	
k	0.063	
D	99	m
A	7697.7	m ²
I_a	0.13	
R_{nb}	278.8	m
$R_{9.5}$	179.4	m
D_{eff}	128.3	m
x_0	45	m
c_1	0.23	
κ	0.40	
γ	N/A*	
β	N/A*	
D_m	N/A*	
b	N/A*	

* Parameter values cannot be presented because they are based on the thrust coefficient of the specific wind turbine. Restrictions that are imposed on the non-disclosure agreement.

5.2.4 CFD WAKE MODEL CONFIGURATION

For the CFD simulations, the wind turbine rotor is modeled by a sponge rotor that consists in a permeable area, which is calculated by pressure gradient through the wind turbine generator, according to the *Fluent* CFD software formulation. CFD simulations used a student version of the *ANSYS Fluent* CFD available for downloading at *ANSYS*³ website (ANSYS, 2017). The CFD model configuration is detailed in the next sub-sections.

5.2.4.1 MESH AND BOUNDARY CONDITIONS

The mesh used in the CFD simulations consisted in 14 zones with 380265 nodes. The longitudinal length of the mesh is 2000 m and width of 700 m. There is a sponge zone that represents the wind turbine, which is defined to be a porous zone that is located at 500 m downstream the inflow, such sponge is 2 m wide in horizontal direction and 100 m long in vertical direction, with 2 m thick, yielding a 400 m³ volume.

Figure 24 illustrates the mesh implemented for this study.

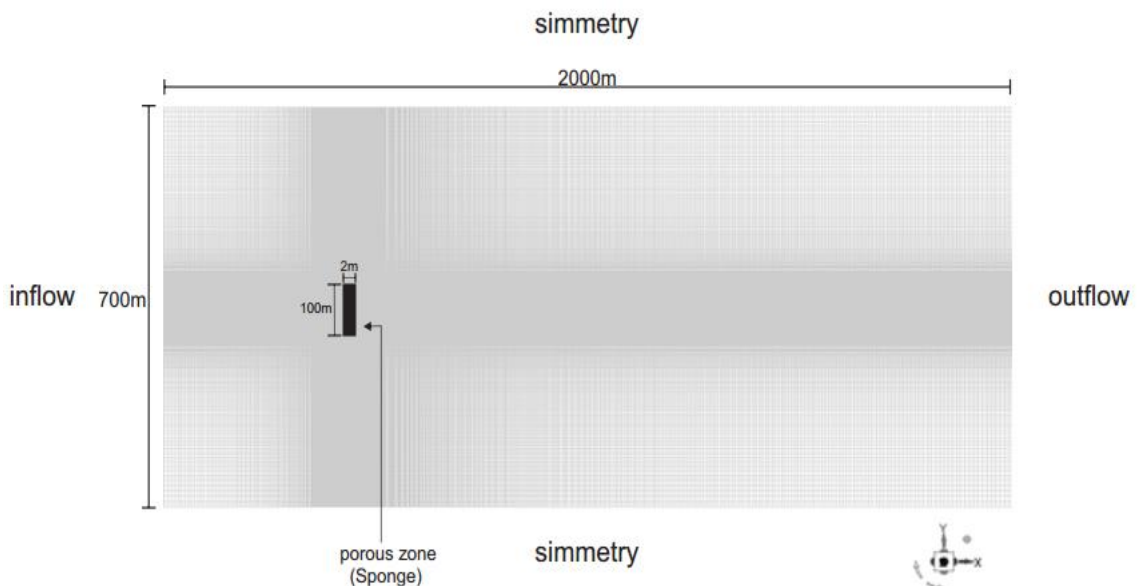


Figure 24: Mesh for CFD wake simulation

³ ANSYS *Fluent* CFD - <http://www.ansys.com/>

The solver parameters were chosen to be pressure-based, with absolute velocity formulation for a stationary flow. The reference values applied for air density, temperature and viscosity were 1.225 kgm^{-3} , $15 \text{ }^{\circ}\text{C}$, $1.789 \times 10^{-5} \text{ kg (m}\cdot\text{s)}^{-1}$.

Inflow velocity was the entrance boundary conditions, which was taken as the freestream velocity normal to the boundary. Turbulence specification method for the inflow was chosen to be Intensity and Length Scale, where the turbulence intensity parameter was defined as 13% (according to the meteorological mast results) and the turbulent length scale was defined as 1 m, equals to the computational node volume.

The sponge zone was assumed to be a porous zone for the CFD wake model implementation. Such boundary condition is based on three parameters: Ψ is the medium permeability, C_2 is the pressure-jump coefficient, v is the velocity normal to the porous face, and Δm is the medium thickness.

Porous jump method is commonly used to model an obstacle whose flow characteristics are known, presented by Malavasi *et al.*, (2012) and Özahi, (2015). The thin porous medium applies a finite thickness, where the pressure drop is designed as a relation of Darcy's Law and an additional inertial loss term according to the following equation (ANSYS, 2017):

$$\Delta p = - \left(\frac{\mu}{\Psi} v + C_2 \frac{1}{2} \rho v^2 \right) \Delta m, \quad (5.1)$$

where μ is the fluid viscosity, Ψ is the medium permeability, C_2 is the pressure-jump coefficient, v is the velocity normal to the porous face, and Δm is the medium thickness.

ANSYS Fluent manual provides a procedure to compute the permeability and the pressure-jump coefficients, based on pressure drop of the freestream wind through the sponge zone.

Table 6 summarizes the relation between pressure drop and wind freestream velocity. It must be noted that the pressure drop was based on the pressure gradient between the inflow and LiDAR wind speed, 100 m downstream. Therefore, the pressure drop assumes a second order equation dependent of the

inflow wind speed, where the pressure drop increases as the wind speed develops, except for the 12 ms^{-1} .

Table 6: Pressure drop related to freestream velocity

Freestream Velocity (ms^{-1})	Pressure Drop (Pa)
5	9.2
6	14.7
7	19.3
8	24.7
9	33.3
10	35.1
11	48.5
12	43.3

A second order polynomial was fitted to the data, yielding the empirical pressure drop function below:

$$\Delta p = 0.249v^2 + 1.102v, \quad (5.2)$$

where Δp is the pressure drop and v is the velocity.

The parameters for the porous zone, listed in Table 7, were obtained by comparing, equations (5.1) and (5.2).

Table 7: Sponge porous zone parameters

Porous Zone Parameter	Unit	Symbol	Value
Face Permeability	m^2	ψ	0.00003
Porous Medium Thickness	m	Δm	2
Pressure-Jump Coefficient	m^{-1}	C_2	0.203

5.2.4.2 TURBULENCE MODEL

The mathematical model for the CFD flow simulation is based on the steady state Navier-Stokes equations, for incompressible fluids. The standard " $k - \varepsilon$ " turbulence model was applied, which solves one differential equation for

turbulence kinetic energy, k , and another for turbulent dissipation rate, ε . This turbulence model allows the determination of a turbulent length and time scale. Proposed by Launder and Spalding (1974), the model produces a reasonable representation for a large range of turbulence. The mainly assumption is related to the idea that flow is fully turbulent. For details of the turbulence model see Launder and Spalding (1974).

The numerical solution method applied is the pressure-based solver with finite volume, which is applicable for a large range of flow and requires low computational capacity, granting flexibility for the solution process. Then the Semi-Implicit Method for Pressure-Linked Equations (SIMPLE) was applied, better detailed in Ferziger and Peric (2001), where the algorithm employs a relationship between wind speed and pressure adjustment to accomplish mass conservation and to simulate the pressure field (ANSYS, 2017). Moreover, gradients are necessary to compose values of a scalar at the cell faces, but also for estimating wind speed derivatives. Green Gauss Cell Based was chosen for being the least computationally demanding, which was a requirement for this study, the method is used to compute the gradient of the scalar at cell center, see section (25.3.3 Evaluation of Gradients and Derivatives) of (ANSYS, 2017) guide. The Standard Method was applied in treating interpolation schemes for calculating cell-face pressures. By the end, it was chosen a Second-Order Upwind Scheme to solve momentum, turbulent kinetic energy and dissipation rate with higher accuracy than the first order. For more details of upwind scheme see, Barth and Jespersen, (1989).

5.2.5 COMPARISON OF WAKE MODELS AND LIDAR MEASUREMENTS

In order to evaluate the performance of the wake modeling simulations, this sub-section presents the intercomparison of the freestream velocity recovery measured with LiDAR and the velocity recovery simulated with the five models for different locations in the wake. The velocity recovery locations were selected either along the centerline or along the cross section.

The intercomparison results were selected for streamflow velocities ranging from 5 ms^{-1} to 12 ms^{-1} . This range have been chosen due the low wind speed density during the sample period and also due the quality recovery of the

LiDAR. The results were discussed individually in order to understand the behavior of wake models for each streamflow velocity bin in the ensuing sub-sections.

5.2.5.1 5 ms⁻¹ WIND SPEED BIN

For the 5 ms⁻¹ wind speed bin, the velocity recovery values at the wake centerline were depicted in Figure 25.

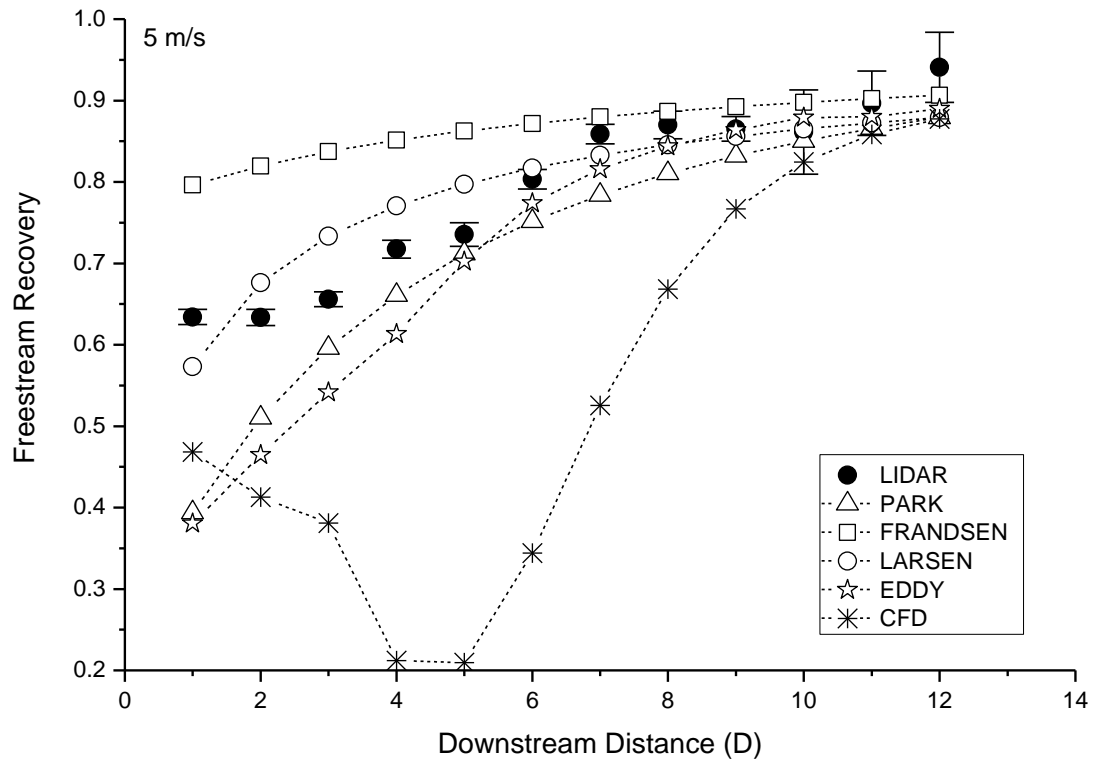


Figure 25: 5 ms⁻¹ velocity recovery along the wake centerline

For the 5 ms⁻¹ streamflow wind, the LARSEN model had the best overall agreement with the LiDAR data. The largest difference was a 12% overestimation at $x = 3D$ downstream of the hub. The PARK and EDDY VISCOSITY ranked second with respect to LiDAR data agreement. Both underestimate the velocity recovery from the beginning of the wake up to $x = 8D$, farther downstream ($x > 9D$) there is a fairly good agreement between measured and simulated velocity recovery along the wake centerline.

The FRANDSEN model wake simulation was fairly different than the measured wake. This model overestimates the centerline wind speed recovery

from the beginning up to $x = 9D$; farther downstream ($x > 10D$) the simulated velocity recovery values were within the error bars of the measured wake.

The CFD model had the lowest agreement of all models. There is significant discrepancy in the centerline velocity recovery from the beginning up to $x = 9D$. The largest discrepancy was close to 70% at $4D < x < 5D$. This could be attributed to the hypothesis to simulate the wind turbine, which could be causing the extraction of energy even downstream the swept area.

Figure 26 compares the velocity recovery shapes at three distinct cross sections downstream of the wind turbine. LARSEN, PARK and FRANDSEN models simulate self-similar shapes, whereas the CFD computes the function shape.

The measured wake for the 5 ms^{-1} inflow was asymmetric, with lower velocity recovery fraction on the left side than on the right side (and centerline). Such asymmetry could be attributed to some wake influences from lateral wind turbine.

The best model simulation for the three cross sections located 500 m, 700 m and 1000 m behind the hub was produced by the LARSEN wake model. About 50% of the points simulated velocity recovery fractions within $\pm 10\%$ difference with respect to the measured values, and 13% of the points with less than $\pm 1\%$ difference.

Regarding the velocity recovery cross-sectional shape simulation the models ranked: first LARSEN, second FRANDSEN, third PARK and fourth CFD.

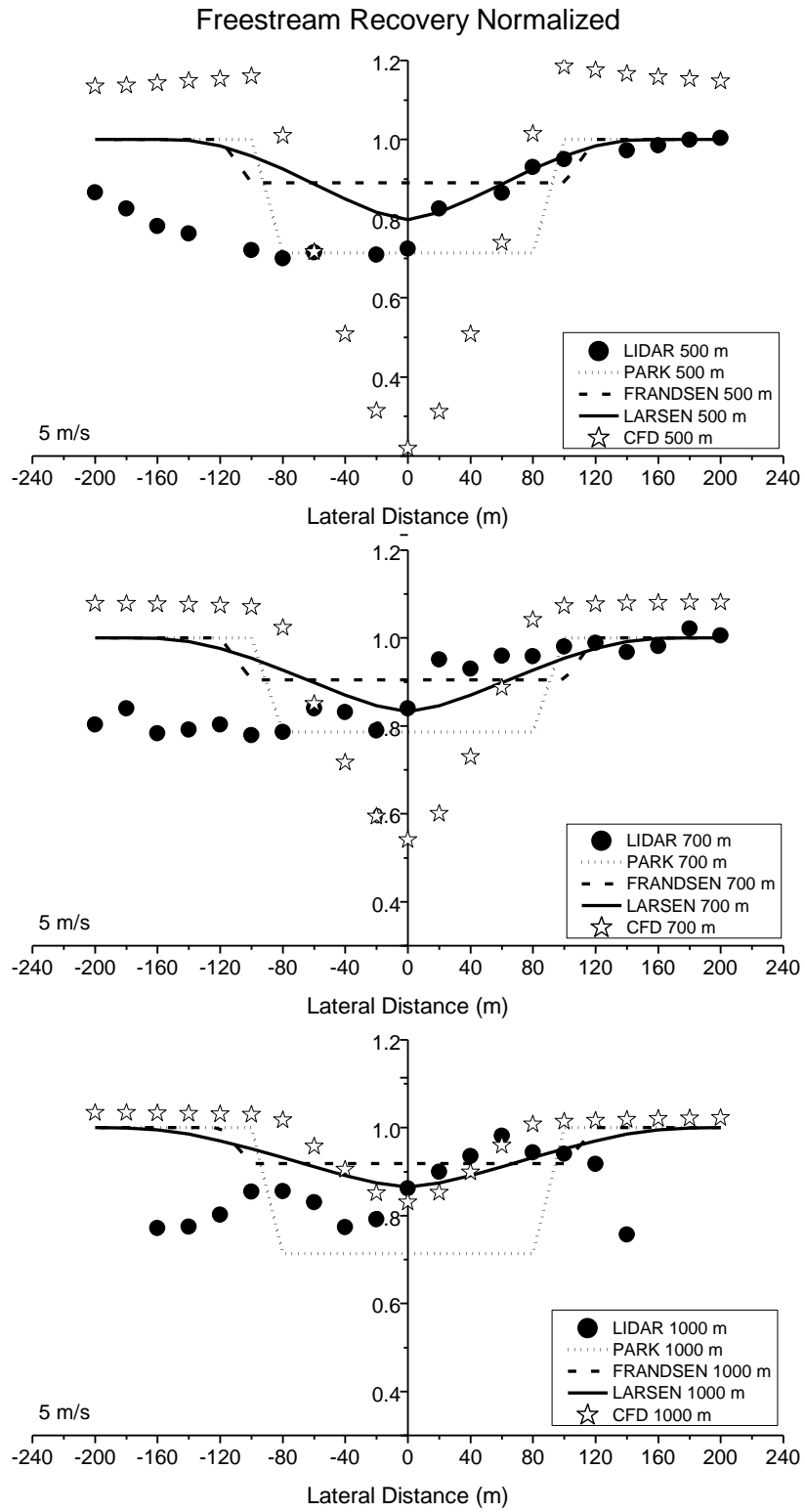


Figure 26: 5 ms^{-1} velocity recovery along the wake cross sections

5.2.5.2 6 ms⁻¹ WIND SPEED BIN

The centerline velocity recovery fractions for the 6 ms⁻¹ inflow wind are displayed on Figure 27, for the measured LiDAR data, and for the five models simulations.

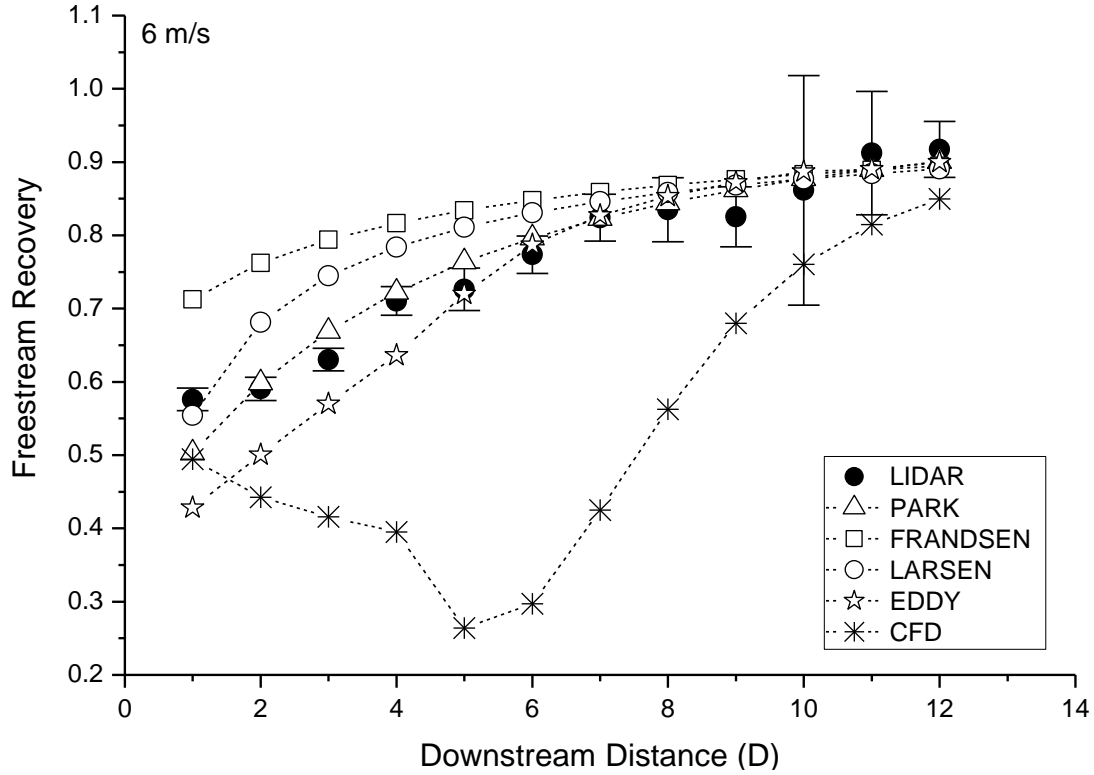


Figure 27: 6 ms⁻¹ velocity recovery along the wake centerline

PARK model had an excellent agreement to the LiDAR measurements, since almost all points of the simulation were within the range of LiDAR errors. The highest difference was 13% at the first rotor diameter downstream. LARSEN model presented four downstream distances are over than the validation rate of 10%, from $2D \leq x \leq 5D$ rotor diameters respectively. Meanwhile, EDDY VISCOSITY model demonstrated the highest difference to be 29% at $x = 2D$.

The rank of model accuracy for the centerline velocity recovery fraction for the 6 ms⁻¹ wind inflow is: first PARK, second LARSEN (overestimate), third EDDY VISCOSITY (underestimate), fourth FRANDSEN (overestimate) and fifth CFD (underestimate).

The complementary analysis for the 6 ms⁻¹ wind speed bin is the assessment of the wake cross section shapes which are shown in Figure 28.

The measured wake for the 6 ms^{-1} inflow was asymmetric up to 700 m behind the hub, with lower velocity recovery fraction on the left side than on the right side (and centerline). The measured shape for the wake cross section was almost symmetrical for the 1000 m downstream location.

The cross section shape simulations for PARK, LARSEN and FRANDSEN models were quite close to the measured wake shape. The best simulation was for the PARK model with 67% of the points having differences smaller than $\pm 10\%$ of the measured wake.

The CFD results were quite poor for both 500 m and 700 m cross sections. However the CFD simulation achieved an outstanding accuracy for the 1000 m cross section.

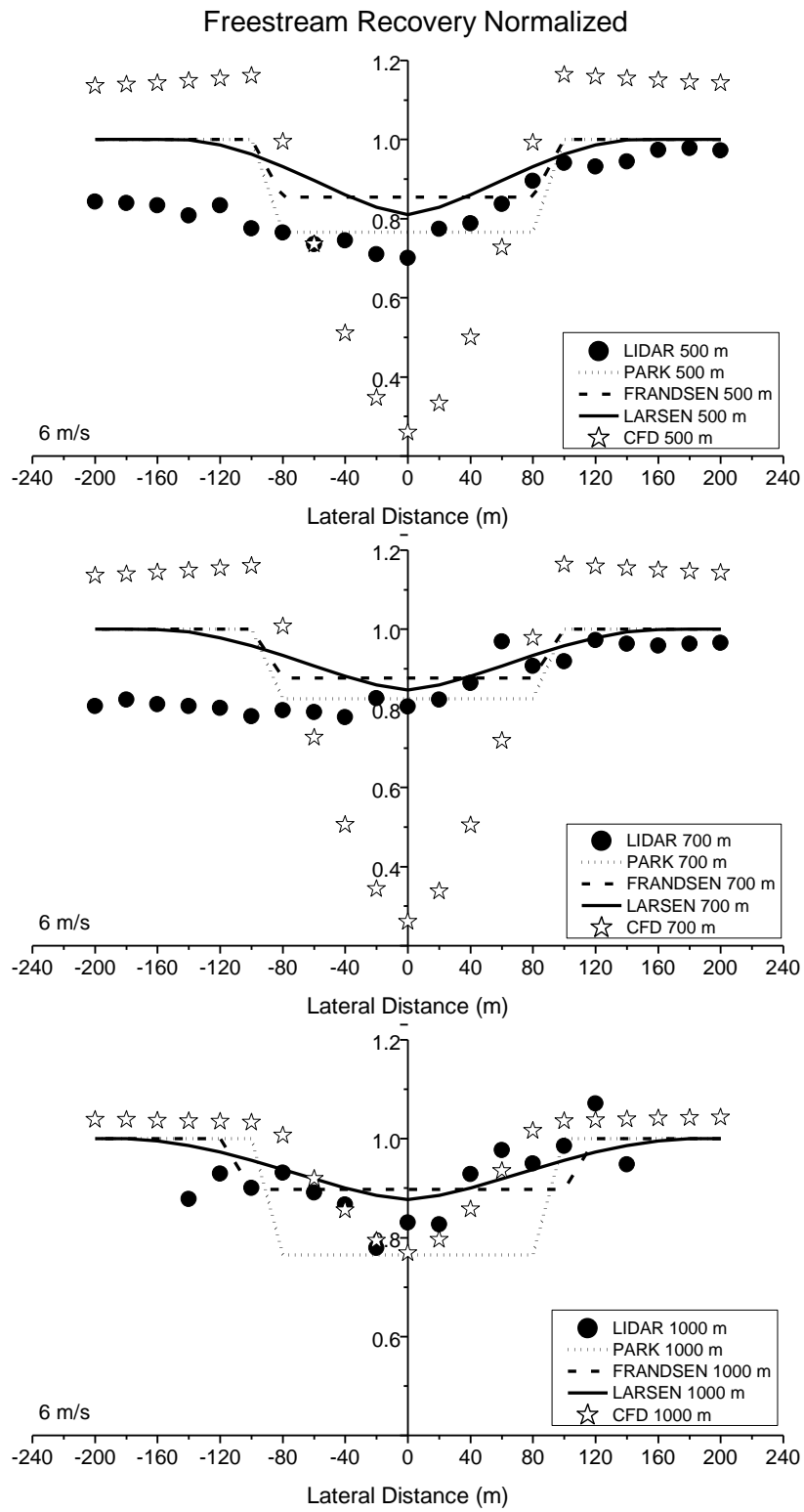


Figure 28: 6 ms^{-1} velocity recovery along the wake cross sections

5.2.5.3 7 ms⁻¹ WIND SPEED BIN

For the case of 7 ms⁻¹ inflow wind, the centerline velocity recovery fraction is illustrated in Figure 29, in which the measured fractions had smaller standard errors up to 10 D, due to the large wind data counts.

The PARK model presented excellent agreement with all the centerline points showing velocity recovery fractions with less than 10% of difference with respect to LiDAR measurements. The LARSEN model agreement with wake measurement was also very high, with 84% of the centerline points with less than 10% difference with respect to the measurements.

The EDDY VISCOSITY underestimated the velocity recovery fraction for the centerline region from the hub up to $x = 6D$, whereas the simulation was quite accurate for $x > 7D$.

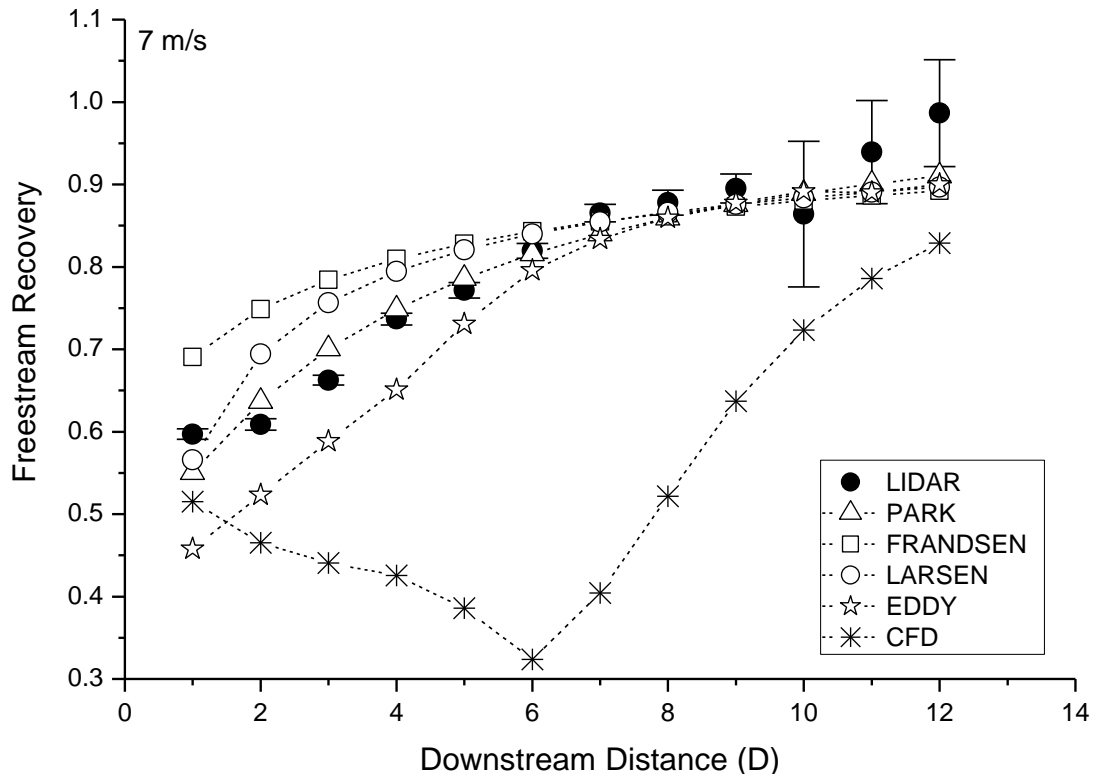


Figure 29: 7 ms⁻¹ velocity recovery along the wake centerline

The FRANDSEN model overestimated the velocity recovery fraction for the centerline wake between the hub and $x = 6D$. There was high agreement between the simulated and measured wake for the centerline region $x > 7D$.

The poorest results were for the CFD simulation. The CFD model underestimated the velocity recovery fraction throughout the centerline domain.

Figure 30 shows the cross section wake results for the 7 ms^{-1} inflow wind. The measured wake for the 7 ms^{-1} inflow was asymmetric for all three cross sections, with lower velocity recovery fraction on the left side than on the right side.

The simulation of the cross section shapes produced by PARK, LARSEN and FRANDSEN models were close to the measured wake for the cross section half between the centerline and the wake right edge. The PARK model was dominating at 500 m with 67% of its points lower than the limit validation. Nonetheless sections 700 and 1000 m were dominated by LARSEN model, which demonstrated 62% and 60% of its points to be lower than threshold validation.

The CFD model for the 7 ms^{-1} inflow produced the lowest accuracy among the models for the two cross sections closer to the hub (500 m and 700 m). However, the cross section shape agreed with the measurements for the 1000 m cross section.

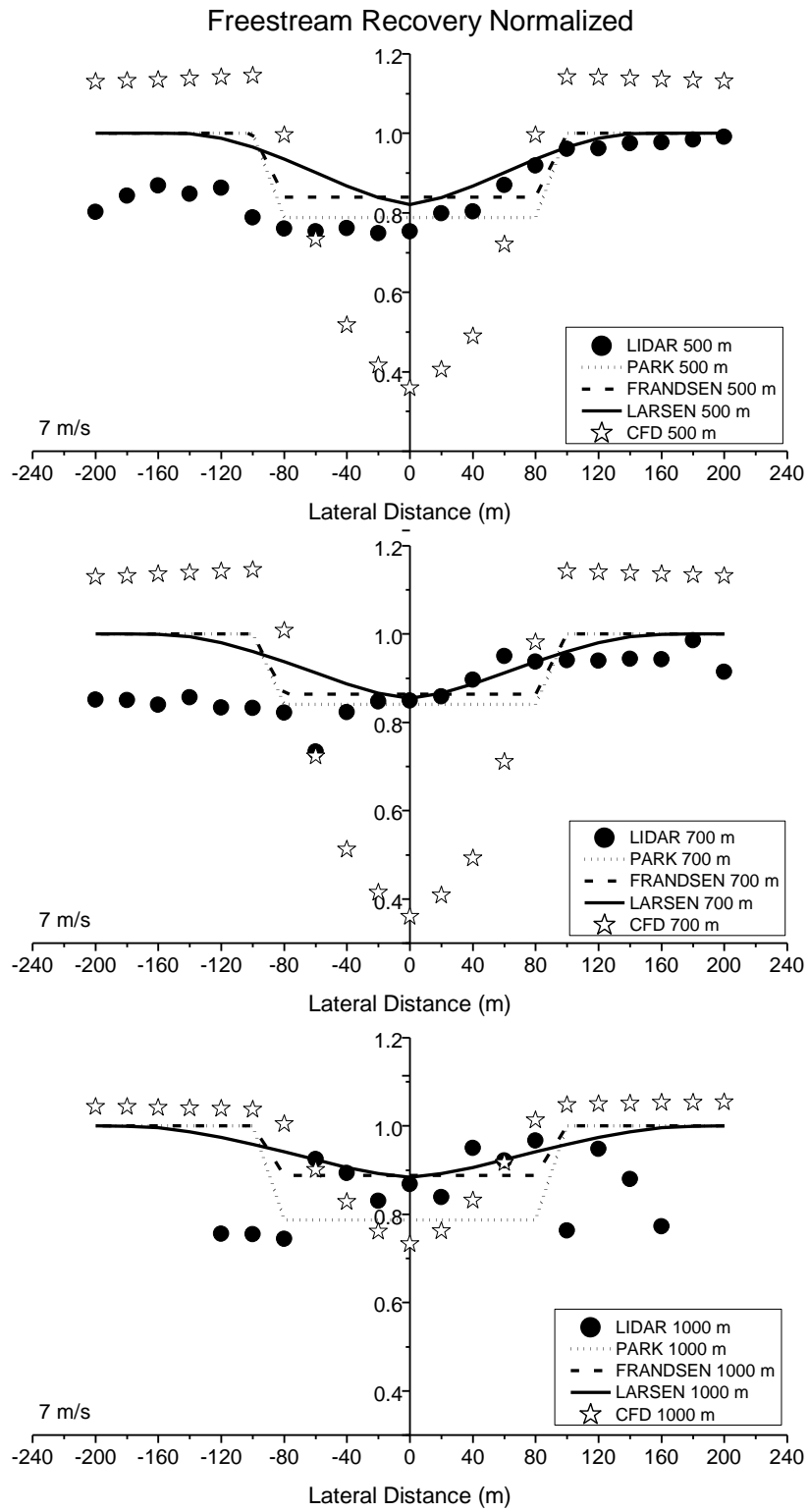


Figure 30: 7 ms^{-1} velocity recovery along the wake cross sections

5.2.5.4 8 ms⁻¹ WIND SPEED BIN

Figure 31 shows the centerline velocity recovery fraction for the 8 ms⁻¹ wind inflow condition, whose pattern is similar to the previous wind speed bin. The measured centerline wake presents smaller standard errors than the previous inflow bins, due to the larger wind data counts. The PARK model once again had the best agreement to the LiDAR data, with differences in the velocity recovery fractions smaller than 10% for all twelve centerline locations.

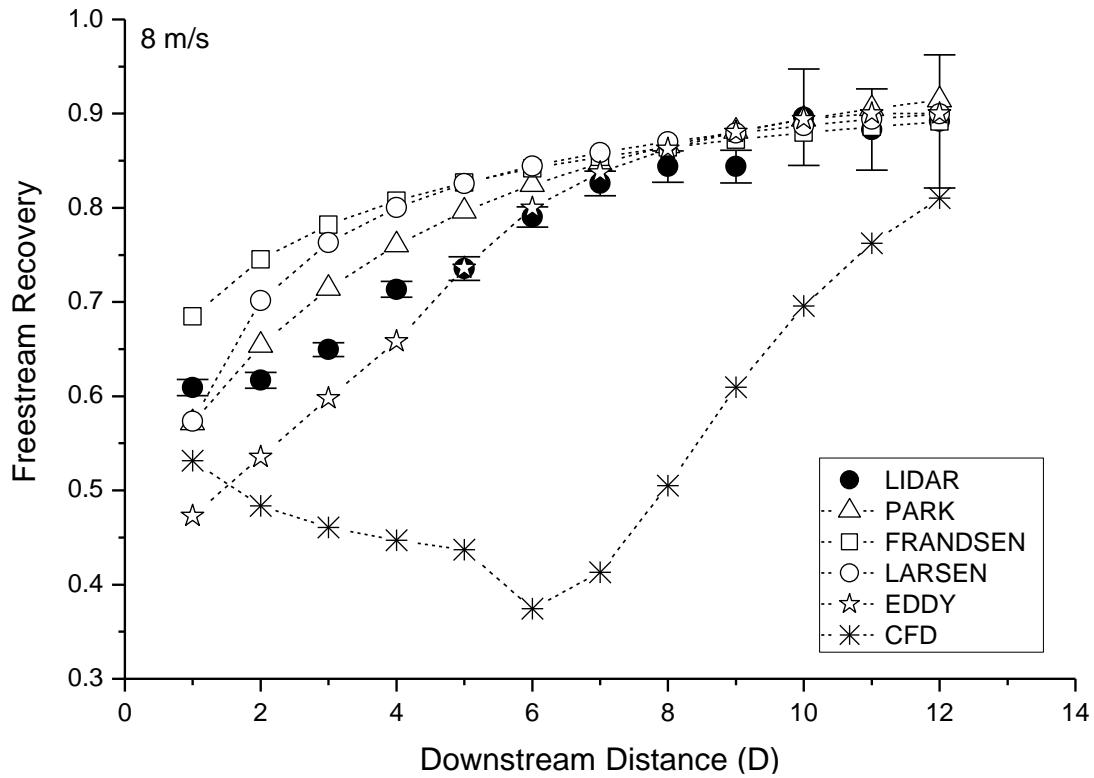


Figure 31: 8 ms⁻¹ velocity recovery along the wake centerline

The EDDY VISCOSITY model ranked second in accuracy. It underestimated the velocity recovery fraction for $x < 4D$, and matched the LiDAR measurements for $x > 5D$. The largest differences between simulation and measurements were 22% and 13%, for $x = 1D$ and $x = 2D$, respectively.

LARSEN and FRANDSEN models ranked third and four with respect to centerline wake accuracy. Both overestimated the velocity recovery fraction for $x < 8D$. The CFD model ranked last with respect to accuracy, underestimating the velocity recovery fraction throughout the wake.

Figure 32 depicts the wake transversal shape analysis for 8 ms^{-1} inflow wind.

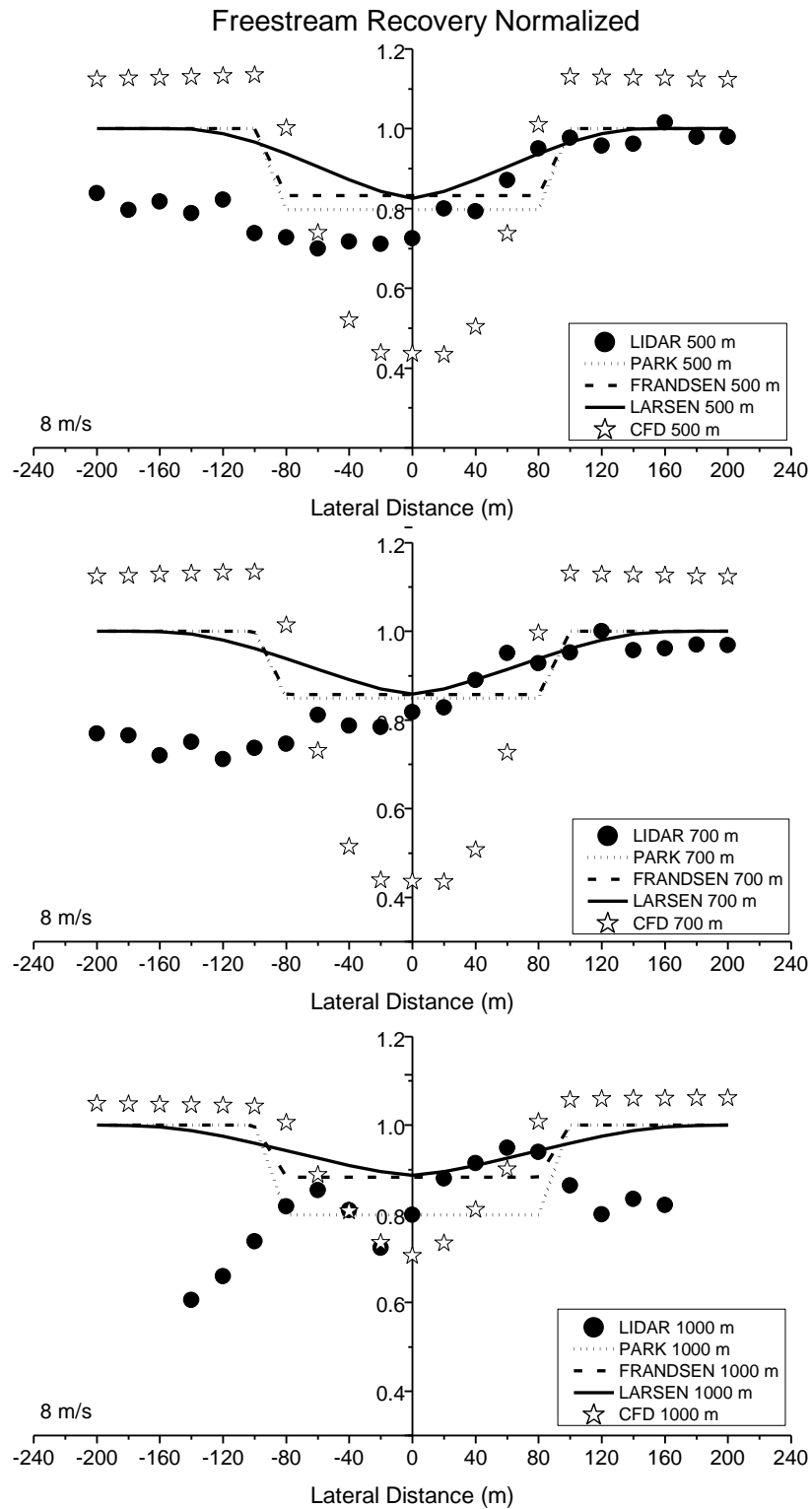


Figure 32: 8 ms^{-1} velocity recovery along the wake cross sections

As in previous inflow bins, the measured wake for the 8 ms^{-1} inflow was asymmetric for all three cross sections, with lower velocity recovery fraction on the left side than on the right side. Therefore, the simulated wakes, which are symmetric, showed a closer match to the measurements for the reach from centerline to the wake right edge.

The models of LARSEN, FRANDSEN and PARK had similar performances with respect to the velocity recovery fraction over the 500 m and 700 m cross sections. Although, PARK model dominated the 500 m, while LARSEN model exceeded at 700 m and 1000 m. The current implementation of the CFD model had the lowest agreement of all models for the three cross-sections.

5.2.5.5 9 ms^{-1} WIND SPEED BIN

Figure 33 and Figure 34 show the centerline and transversal velocity recovery fraction, respectively, for the 9 ms^{-1} wind inflow condition.

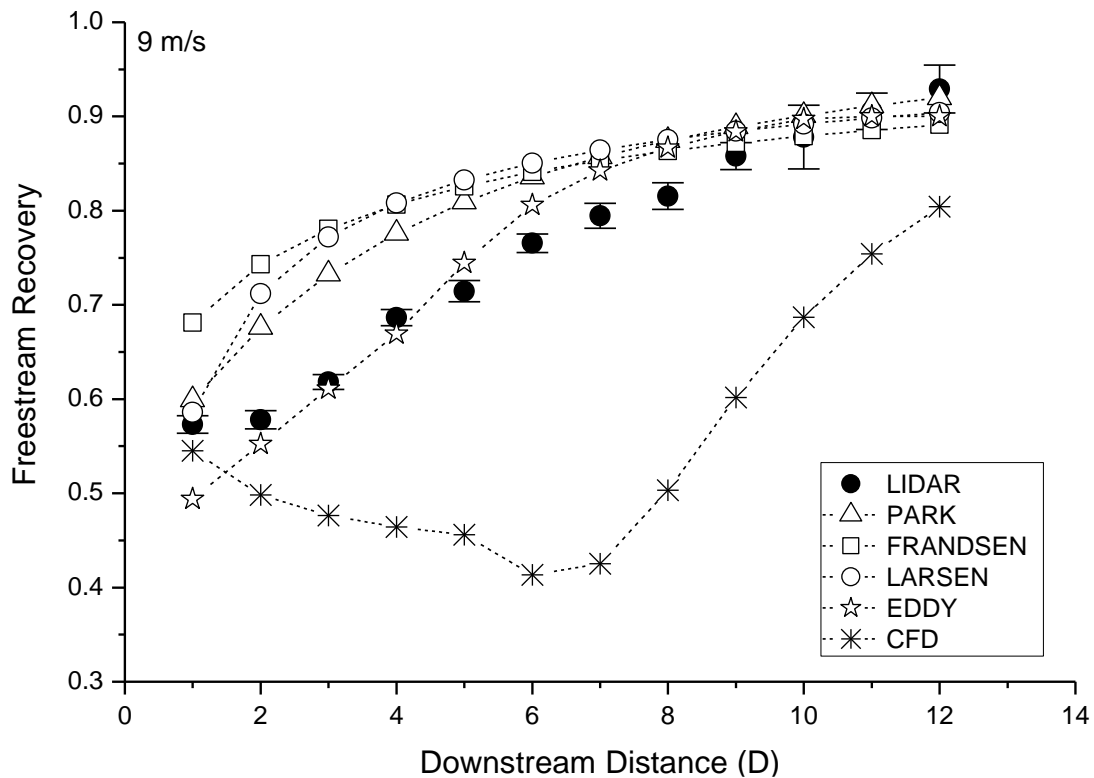


Figure 33: 9 ms^{-1} velocity recovery along the wake centerline

The EDDY VISCOSITY model produced the best agreement with the LiDAR data. The centerline velocity recovery fraction for all points, except at $x =$

$1D$, had less than 10% difference with respect to the measurement. Only for $x = 1D$ there was a 14% difference. The PARK model ranked second with four marks greater than 10 % difference related to LiDAR measurements data, from $2D \leq x \leq 5D$. The LARSEN model did not have the same accuracy as presented in the previous wind speed bins, ranking in third at 9 ms^{-1} . The model presented the highest difference of 25% at $x = 3D$. In fourth was characterized by FRANDSEN model, which demonstrated similar pattern to second and third, but lower accuracy. CFD model presented the poorest accuracy among the models even characterizing an improvement.

The cross section wake analysis for 9 ms^{-1} wind inflow has shown the same patterns of the previous wind inflow bins. PARK, FRANDSEN and LARSEN wake model simulations show a close agreement with measurements for the 500 m and 700 m cross-section, followed by a poorer agreement for the 1000 m cross section. The CFD model simulation ranked last with respect to accuracy, although it has shown an acceptable agreement for the 1000 m cross section.

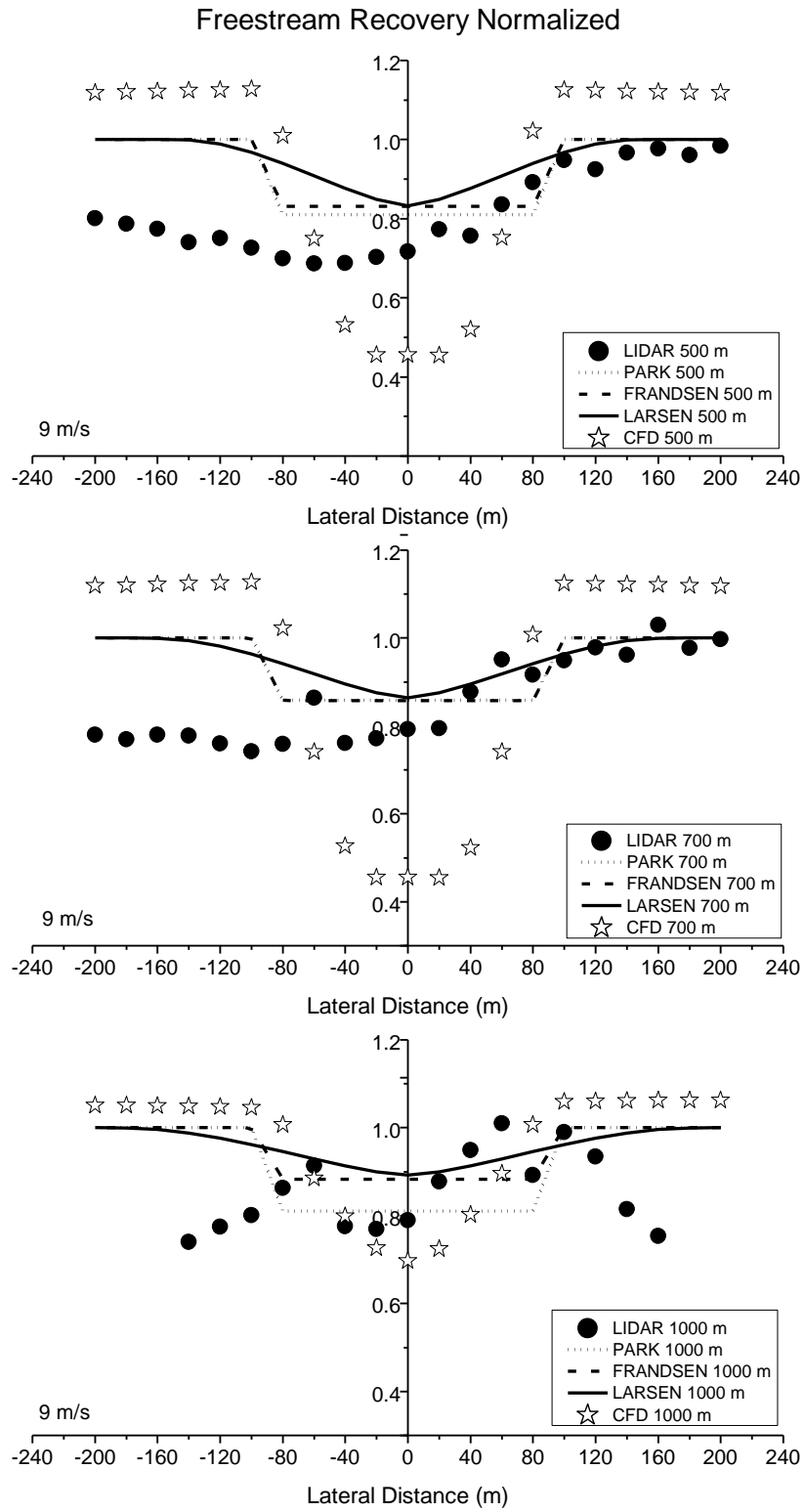


Figure 34: 9 ms⁻¹ velocity recovery along the wake cross sections

5.2.5.6 10 ms⁻¹ WIND SPEED BIN

Figure 35 and Figure 36 depict the centerline and transversal velocity recovery fraction, respectively, for 10 ms⁻¹ inflow wind.

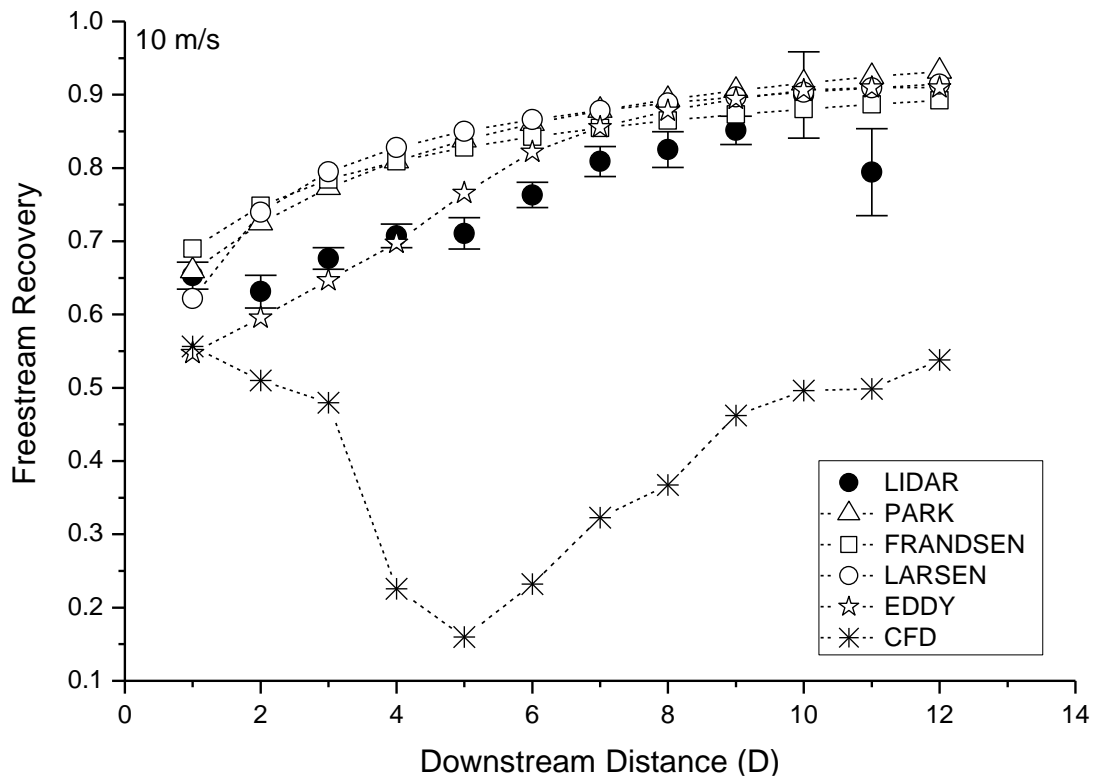


Figure 35: 10 ms⁻¹ velocity recovery along the wake centerline

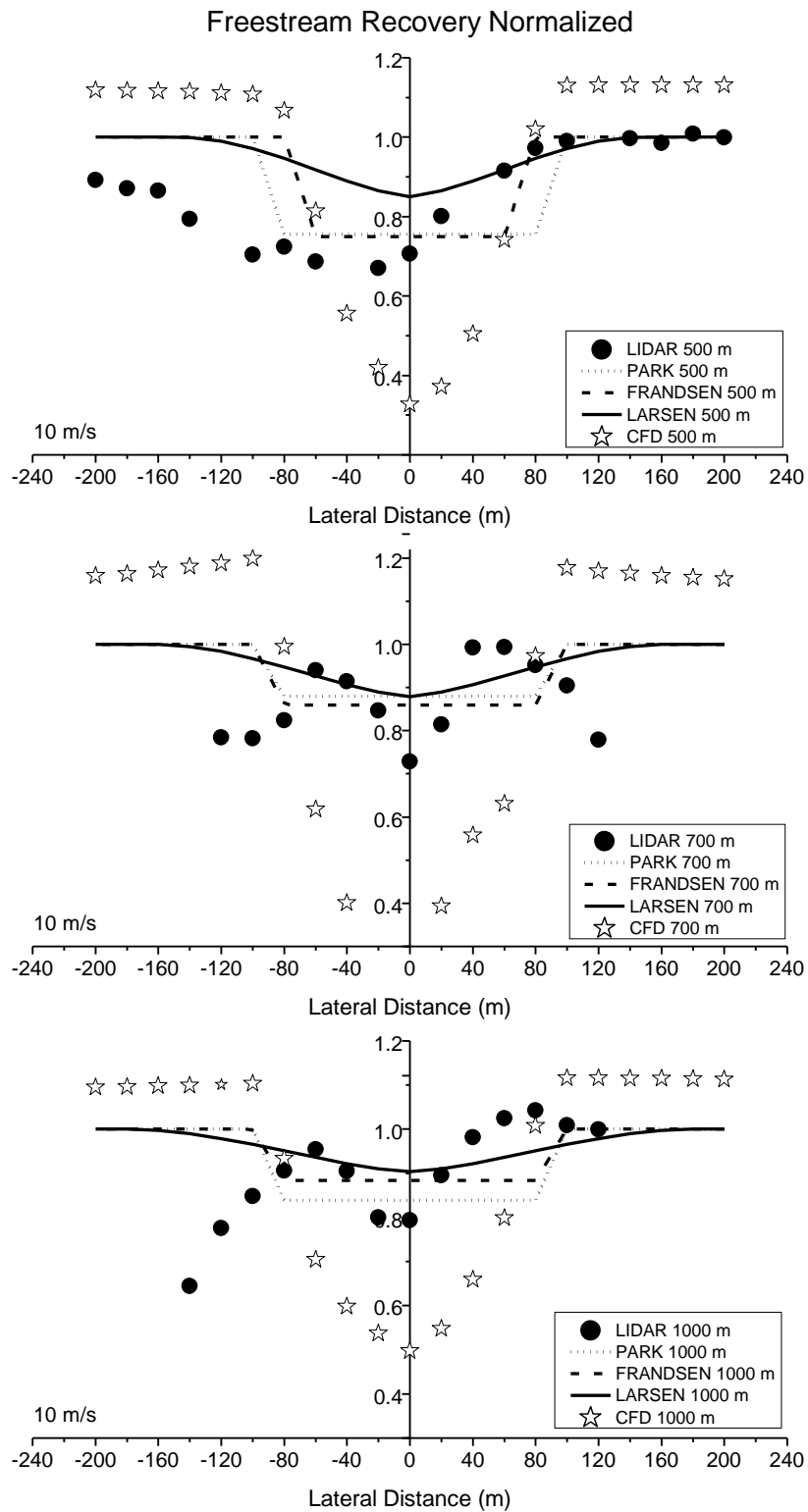


Figure 36: 10 ms^{-1} velocity recovery along the wake cross sections

For the wake centerline, the EDDY VISCOSITY model produced the best agreement with LiDAR data. The difference between simulated and measured

velocity recovery fraction was less than 10%, for all centerline points except at $x = 1D$ (16% underestimation) and at $x = 11D$ (15% overestimation).

FRANDSEN, PARK and LARSEN models overestimated the velocity recovery fraction for the centerline points, ranging from the hub to $x = 10D$. Ranking in second the FRANDSEN model present the highest value to be 19% at $x = 2D$. After the PARK model showed two points inside the error bar range while LAREN model only had one point. The current CFD model implementation ranked last with respect to agreement with measured data, having grossly underestimated the centerline velocity recovery.

Regarding the wake characteristics along the cross section, it is noted that the measured values varied significantly along the 700 m and 1000 m cross sections for the 10 ms^{-1} inflow wind. Nevertheless, FRANDSEN, PARK and LARSEN wake models have described the LiDAR measured pattern, for the 500 m cross section. The current implementation of the CFD model grossly underestimated the velocity recovery fraction for the 500 m cross section.

There was a significant discrepancy between simulated and measured wake for both the 700 m and 1000 m cross sections, for all models. Therefore, one may question whether those measurements truly describe the wake, considering that the wind counts get smaller when the inflow wind increases.

5.2.5.7 11 ms^{-1} WIND SPEED BIN

Figure 37 shows the simulated and measured velocity recovery fraction, at the wake centerline, for 11 ms^{-1} inflow wind. EDDY VISCOSITY, PARK, LARSEN and FRANDSEN models had overestimated the velocity recovery at the wake centerline, whereas the current implementation of the CFD model had underestimated the measured values.

The EDDY VISCOSITY model had the best agreement with the LiDAR data, where only presented one difference over 10% at $x = 2D$. The FRANDSEN model had the best agreement with measured velocities for $x > 6D$.

The LARSEN and PARK model wake simulations were very similar, and both overestimated the wake centerline velocity recovery. The CFD model ranked last with respect to agreement with measured data at the centerline, underestimating from $x > 2D$. Although, the model presented to match the LiDAR

data with difference of 4% and 6% at $x = 1D$ and $x = 2D$ respectively. Meanwhile, the high interval of the LiDAR error bars could be attributed to low data counts.

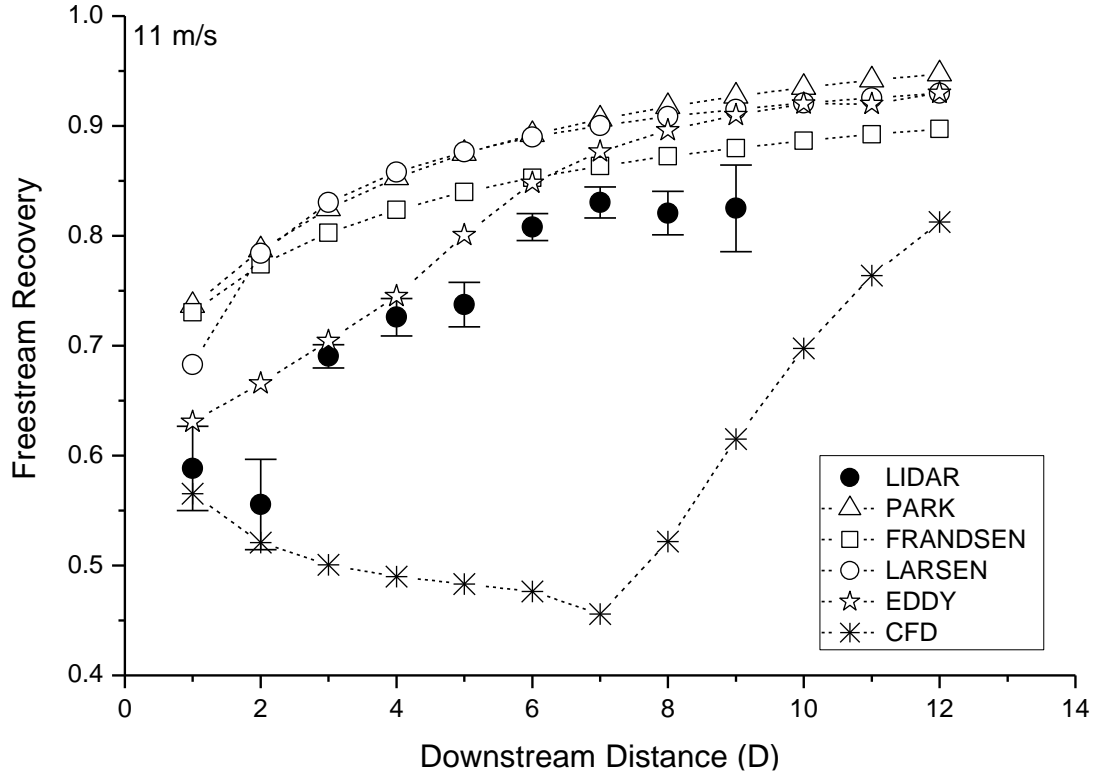


Figure 37: 11 ms^{-1} velocity recovery along the wake centerline

Regarding the wake characteristics along the cross section, it is noted that the measured values varied significantly along the 700 m and 1000 m cross sections for the 10 ms^{-1} inflow wind. Nevertheless, FRANDSEN, PARK and LARSEN wake models have described well the right side of the LiDAR measured pattern, for the 500 m cross section. The current implementation of the CFD model grossly underestimated the velocity recovery fraction for the 500 m cross section.

Figure 38 depicts the transversal velocity recovery fraction, at the 500 m, 700 m, and 1000 m cross sections, for 11 ms^{-1} inflow wind. There is significant variability in the LiDAR wake measurements, which sample sizes get smaller when the inflow wind increases.

There is some agreement between measured and simulated velocity recovery only along the 500 m cross section, where PARK was dominating. The LARSEN model exceed at 700 m, while FRANDSEN model ranks first at 1000 m. The CFD model underestimated the velocities for both 500 m and 700 m cross

sections. However, the CFD accurately simulated the velocity recovery for the 1000 m cross section.

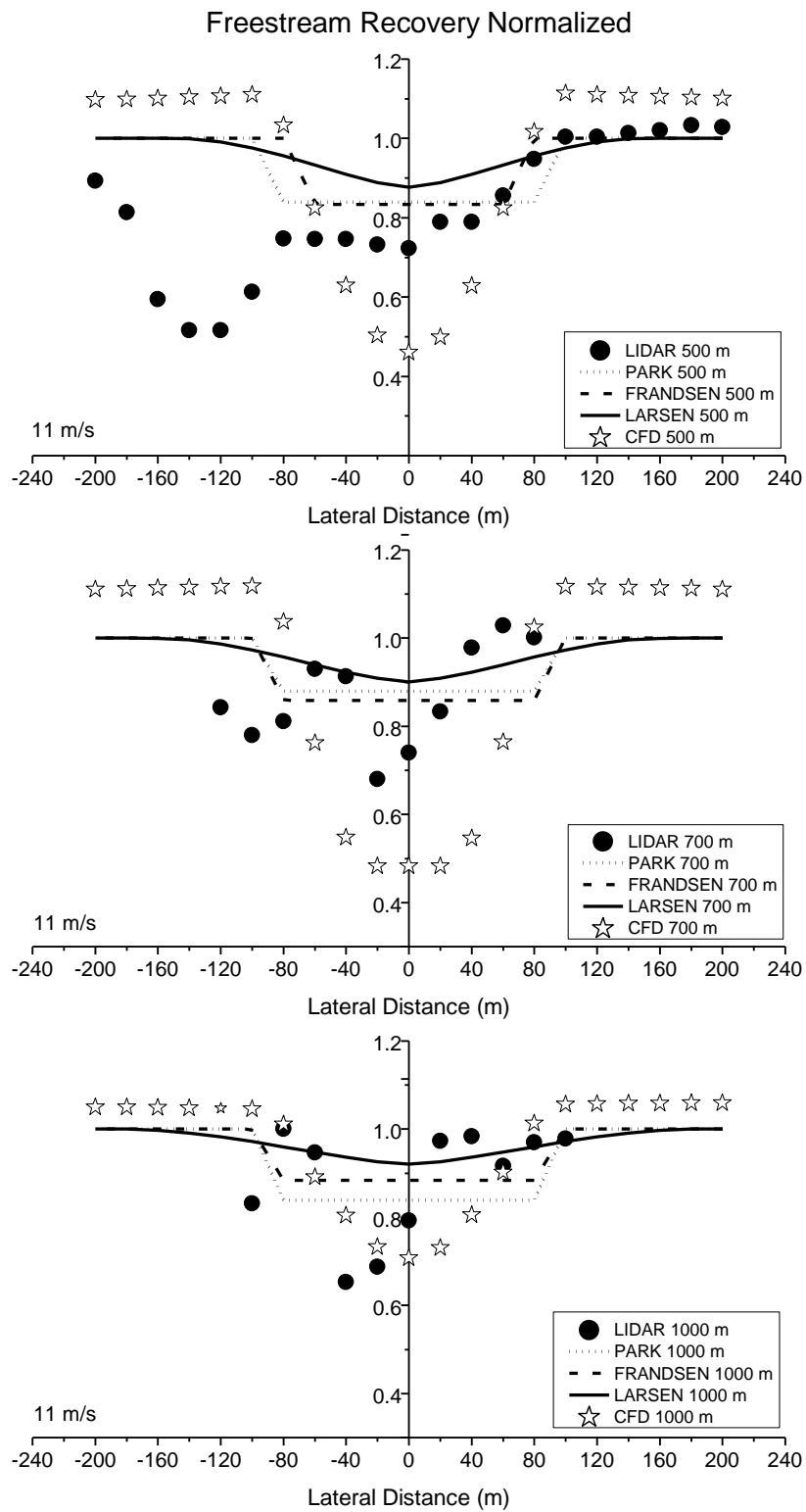


Figure 38: 11 ms⁻¹ velocity recovery along the wake cross sections

5.2.5.8 12 ms⁻¹ WIND SPEED BIN

Figure 39 and Figure 40 depict the centerline and transversal velocity recovery fraction, respectively, for 11 ms⁻¹ inflow wind.

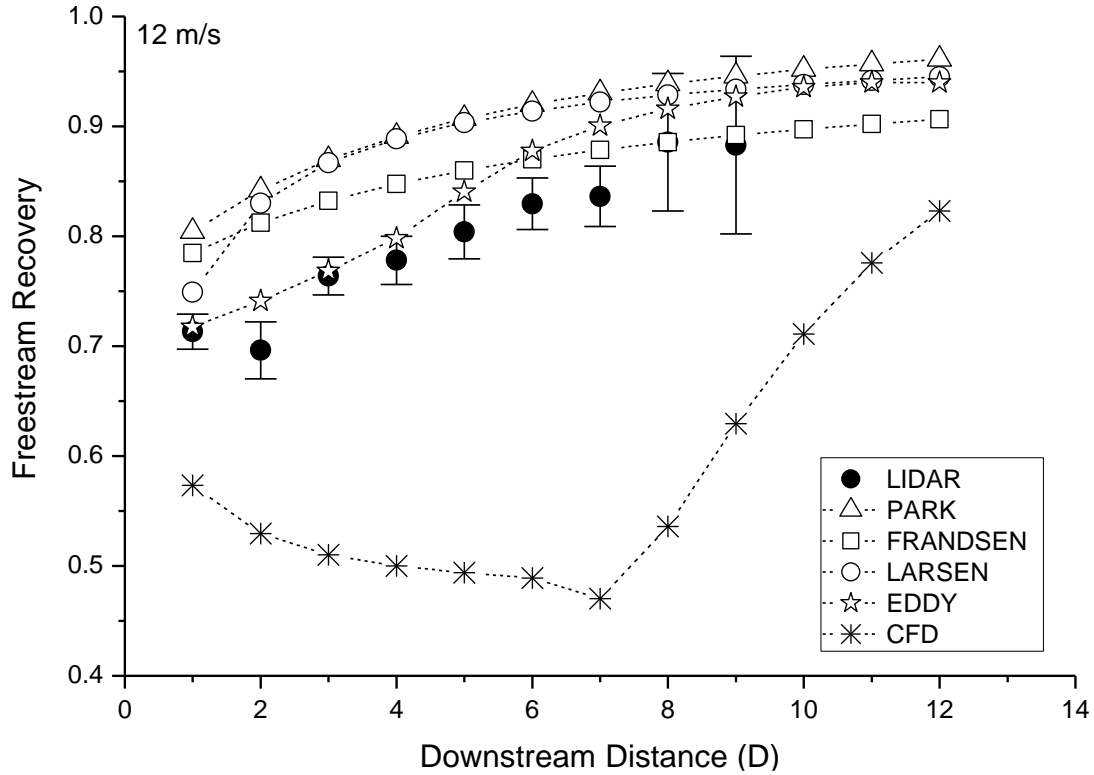


Figure 39: 12 ms⁻¹ velocity recovery along the wake centerline

The EDDY VISCOSITY model produced the highest accuracy with respect to the LiDAR data, mainly in the near wake. The difference between measured and simulated velocities were lower than 1% for the centerline points at $x = 1D$ and $x = 3D$. Even for the far wake, the differences between simulations and measurements were smaller than 10%.

Regarding centerline wake simulation accuracy, FRANDSEN model ranked second, LARSEN ranked third, PARK fourth, and CFD last. FRANDSEN overestimated LiDAR data for $x < 7D$, but only at $x = 1D$ and $x = 2D$ there were differences above 10% between the centerline wake simulation and measurement. For the far wake, at $x = 8D$ and $x = 9D$, the difference was smaller than 1%, which is impressive for a model that performed poorly for the previous cases of lower inflow winds. LARSEN and PARK models overestimated velocities throughout the wake centerline, both models showed the highest

difference at $x = 2D$, which are 19% and 21% respectively. Besides that, the CFD model underestimated the centerline velocities.

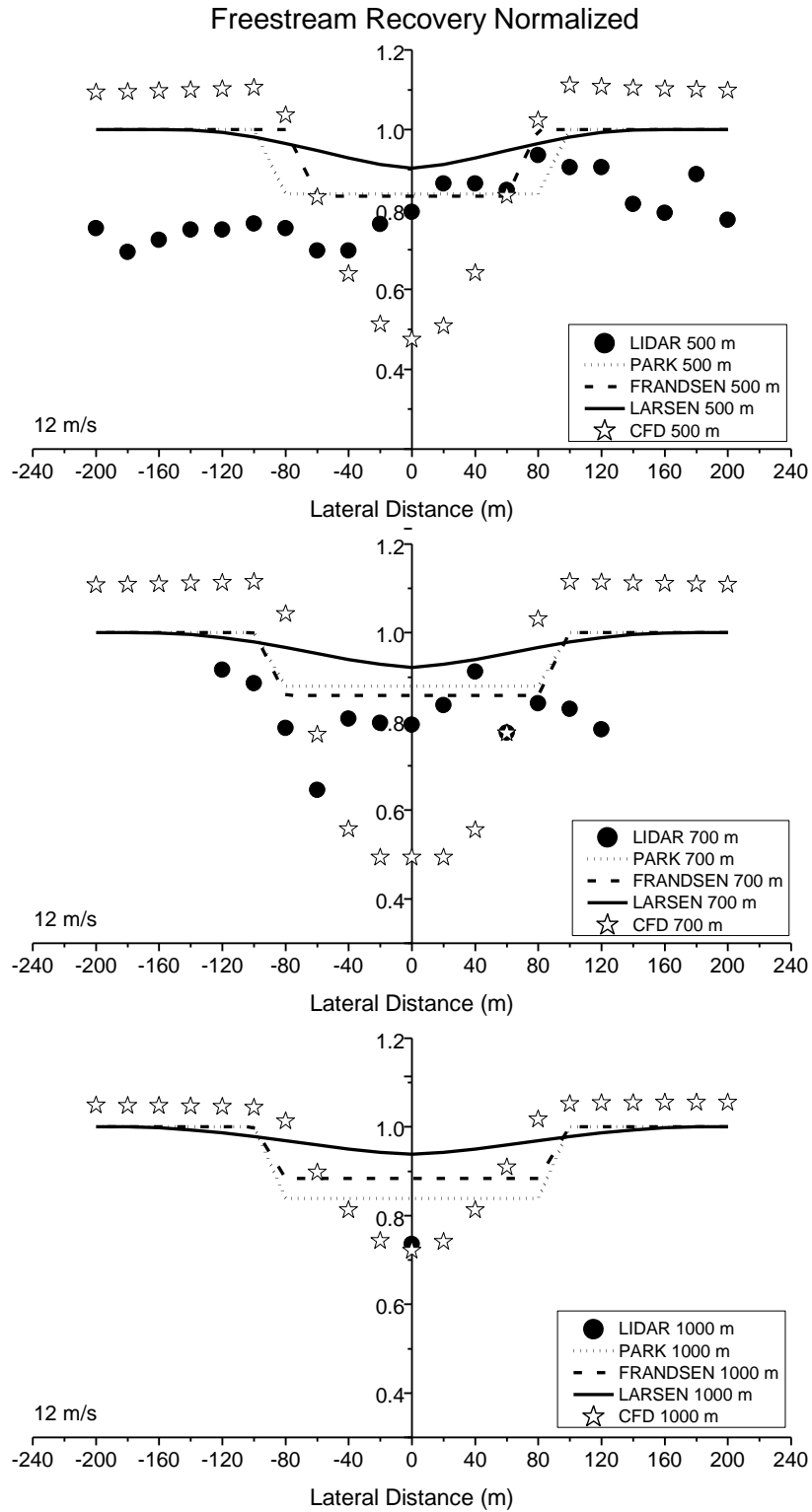


Figure 40: 12 ms^{-1} velocity recovery along the wake cross sections

The last wake analysis is for the three cross sections, which are 500 m, 700 m and 1000 m downstream the turbine, for the 12 ms^{-1} inflow wind. Since the relative frequency of inflow winds within the 12 ms^{-1} wind bin was only 1%, then the number of LiDAR data counts were small. The lower panel of Figure 40 shows only one measured location for the 21-point cross section located at 1000 m downstream the hub. PARK and FRANDSEN models simulated velocities for both the 500 m and 700 m cross sections, yielded the smaller differences with respect to LiDAR measurements. LARSEN model overestimated all cross sectional velocities and the CFD model underestimated the velocities for the 500 m and 700 m cross sections.

5.2.6 WAKE MODEL ACCURACY ASSESSMENT

In order to assess the accuracy of the wake models with respect to LiDAR velocity data, the root mean square error (RMSE) was computed for both centerline and cross-sections for every single wake model and all inflow wind boundary conditions. Wake velocity data is expressed in terms of velocity recovery fractions, i. e., each point value is normalized by the inflow wind. Therefore, the velocity recovery fraction values vary between 0.0 and 1.0.

5.2.6.1 RMSE ANALYSIS FOR THE WAKE CENTERLINE

Table 8 lists the RMSE for the velocity recovery fraction along the wake centerline, in which the lowest fraction for each inflow wind is highlighted. Therefore, presenting which wake model better described the LiDAR measurements.

Table 8: Root Mean Square Error along the wake centerline

Inflow Wind Speed Bin (ms^{-1})	PARK	FRANDSEN	LARSEN	EDDY VISCOSITY	CFD
5	0.0082	0.0114	0.0020	0.0121	0.0886
6	0.0010	0.0092	0.0035	0.0042	0.0745
7	0.0012	0.0054	0.0029	0.0044	0.0868
8	0.0015	0.0052	0.0036	0.0033	0.0662
9	0.0045	0.0088	0.0073	0.0016	0.0535
10	0.0160	0.0128	0.0161	0.0027	0.1444
11	0.0217	0.0152	0.0194	0.0038	0.0548
12	0.0098	0.0039	0.0079	0.0015	0.0802

Therefore, as highlighted on Table 8, the centerline wind velocity recovery fractions were better simulated by LARSEN and PARK wake models for inflow winds equal or smaller than 8 ms^{-1} . LARSEN model produced the most accurate centerline simulation for the 5 ms^{-1} inflow wind (sample average for site B). The PARK model produced the lowest RMSE values for inflow winds between 6 ms^{-1} and 8 ms^{-1} .

For inflow winds equal or higher than 8 ms^{-1} , the EDDY VISCOSITY model, produced the most accurate velocity recover fraction along the wake centerline.

5.2.6.2 RMSE ANALYSIS FOR THE WAKE CROSS

Table 9, Table 10 and Table 11 list the RMSE for the velocity recovery fraction along the 500 m, 700 m and 1000 m. cross sections, respectively. The lowest fraction for each inflow wind is highlighted.

Table 9: RMSE analysis along the cross section, 500 m behind the turbine

Wind Speed Bin (ms^{-1})	PARK	FRANDSEN	LARSEN	CFD
5	0.0187	0.0190	0.0181	0.0942
6	0.0113	0.0142	0.0137	0.0426
7	0.0096	0.0104	0.0113	0.0470
8	0.0150	0.0161	0.0179	0.0524
9	0.0204	0.0216	0.0253	0.0592
10	0.0168	0.0192	0.0193	0.0641
11	0.0428	0.0447	0.0471	0.0813
12	0.0304	0.0325	0.0366	0.0784

For the 500 m cross section, the best simulations were produced by the PARK model, which was also the best for centerline simulations. The LARSEN model obtained the lower value at 5 ms^{-1} velocity.

Along the 700 m cross section, the LARSEN wake model produced the lowest RMSE for the inflow winds between 5 ms^{-1} and 11 ms^{-1} . The FRANDSEN model was the most accurate for the 12 ms^{-1} inflow wind.

Table 10: RMSE analysis along the cross section, 700 m behind the turbine

Wind Speed Bin (ms^{-1})	PARK	FRANDSEN	LARSEN	CFD
5	0.0172	0.0127	0.0125	0.0419
6	0.0132	0.0137	0.0125	0.0964
7	0.0097	0.0096	0.0092	0.0821
8	0.0214	0.0215	0.0212	0.0871
9	0.0180	0.0180	0.0179	0.0726
10	0.0169	0.0175	0.0136	0.1686
11	0.0172	0.0176	0.0160	0.0806
12	0.0151	0.0131	0.0243	0.0684

Table 11: RMSE analysis along the cross section, 1000 m behind the turbine

Wind Speed Bin (ms^{-1})	PARK	FRANDSEN	LARSEN	CFD
5	0.0316	0.0169	0.0143	0.0234
6	0.0137	0.0047	0.0035	0.0059
7	0.0243	0.0190	0.0159	0.0318
8	0.0333	0.0320	0.0288	0.0459
9	0.0215	0.0195	0.0178	0.0319
10	0.0232	0.0197	0.0160	0.0710
11	0.0171	0.0157	0.0164	0.0164
12	0.0108	0.0220	0.0411	0.0002

For the 1000 m cross section, the LARSEN model produced the lowest RMSE values for inflow winds between 5 ms^{-1} and 10 ms^{-1} . For the 11 ms^{-1} inflow wind, FRANDSEN yielded the lowest RMSE. The CFD model produced the lowest RMSE for the 12 ms^{-1} inflow wind; in this case the LiDAR data count was very small, having a single measurement point in the centerline of the 21 points cross section.

6 CONCLUSIONS AND RECOMMENDATIONS

The conclusions and recommendations were organized in two parts: the first evaluated wind power performance through analysis of wind shear and turbulence intensity at site A; the second part, analyzed site B data, to assess the wake velocity field, specifically for the wake centerline and for three cross sections located at 500 m, 700 m and 1000 m behind turbine.

The investigation of the wind parameters that can influence the power performance at the wind farm in the United States of America, named as Site A, used a Galion LiDAR mounted near to the wind turbine. The mean inflow velocity for site A was 7.8 ms^{-1} . Inflow velocity variability was described by a fitted Weibull distribution, with the shape parameter $k=2.70$ and the scale parameter, $c= 8.63 \text{ ms}^{-1}$. The dominant wind direction was southeast. The mean temperature was around 21°C , which is within the range for the Galion LiDAR operation.

According to site A's data analysis, it is concluded that neglecting the turbulence intensity effect in the inflow wind speed that reaches the wind turbine might overestimate the power production approximately 900 MW for lower wind speeds up to 10 m/s, however for higher velocities could underestimated the power production close to 800 MW. Meanwhile, the wind shear coefficients were found to vary between 0 and 0.2 at higher inflow velocities. High wind shear values, close to 0.4, were recorded for lower inflow velocities. Therefore, when high turbulence intensity develops in conjunction with elevated values of wind shear, the power production can be remarkably overestimated and the wind turbine lifetime may be reduced due to turbulence-induced damages.

The site B analysis evaluated the wake of a single WTG in the United States of America. Where the wind resource assessment had been deployed using the PPI scan of Galion LiDAR mounted at the hub of a wind turbine. Therefore, the results from LiDAR delivered a great representation of the wake phenomenon. For site B, the mean wind speed that was 5.1 ms^{-1} , the inflow velocity variability was represented by a fitted Weibull distribution, with the shape parameter $k=1.30$, and the scale parameter $c=5.0 \text{ ms}^{-1}$. The dominant wind direction was the southern section. And the mean of the local air temperature was 15°C .

In terms of centerline wake analysis, the LiDAR wake measurements yielded low standard errors for the near wake, whereas the errors increased for the far wake region. The reason for the error increase with distance could be explained by the low data counts on the far wake. The PARK wake model yielded the best velocity simulations for inflow winds smaller than 8 ms^{-1} . The EDDY VISCOSITY wake model yielded the best performance for wind speed bins from 9 to 12 ms^{-1} . However the model also produced adequate wake simulations for lower inflow winds, with exception of the 5 ms^{-1} bin.

In this study, it was implemented a CFD model, which has a detailed representation of turbulence, and required high computational effort. The CFD model implemented in this study underestimated the velocities within the wake, with larger errors for the near wake region. It is not concluded that the CFD is less accurate than the other simplified models, because the current CFD implementation could have been improved, through sensitivity analysis. The hypothesis applied in the porous jump condition could have been effected the extension of the energy extraction, causing the velocity recovery begin after 6 to 7 rotor diameters downstream of the wind turbine. The conclusion is that the CFD implementation of a wake model is not a simple task.

The cross section wake analysis was carried out for three cross-sections, located at 500 m, 700 m and 1000 m behind the hub. For the 500 m cross section, the best simulations were produced by the PARK model, which was also the best for centerline simulations. Along the 700 m cross section, the LARSEN wake model produced the best simulation for the inflow winds between 5 ms^{-1} and 11 ms^{-1} .

The recommendations for future work are: (1) develop the relationship between the wake centerline velocity recovery and power production of the downstream turbine, in order to estimate the wake effect on power reduction; (2) understand better the CFD and its hypothesis with planned sensitivity analysis and calibration, in order to implement a model with high validation performance.

REFERENCES

- ABEEólica – Associação Brasileira de Energia Eólica. (2017). Available in <<http://www.portalabeeolica.org.br/>> accessed in 10/02/2017.
- Adaramola, M.S., Krogstad, P-A. (2011). Experimental Investigation of Wakes Effects on Wind Turbine Performance. *Renewable Energy*. 36, 2078-2086.
- Ainslie, J. F. (1988). Calculating the flowfield in the wake of wind turbines. *Journal of wind engineering and industrial aerodynamics*, 27.
- ANSYS® Academic Research. (2017). Release 17.2. Help System, Coupled Field Analysis Guide. ANSYS Inc. <http://www.ansys.com/>.
- Antoniou, I., Wagner, R., Pedersen, S. M., Paulsen, U., Madsen, H. A., Jørgensen, H. E., Thomsen, K., Enevoldsen, P., Thesbjerg, L. (2007). Influence of wind characteristics on turbine performance. In: Scientific proceedings. European Wind Energy Conference and Exhibition, Milan, ITA.
- Barth, T. J., Jespersen, D. (1989). The design and application of upwind schemes on unstructured meshes. Technical Report AIAA-89-0366, AIAA 27th Aerospace Sciences Meeting, Reno, Nevada USA.
- Barthelmie, R.J., Frandsen, S.T., Nielsen, M.N., Pryor, S.C., Rethore, P.E., Jorgensen, H.E., (2007). Modelling and Measurements of Power Losses and Turbulence Intensity in Wind Turbine Wakes at Middelgrunden Offshore Wind Farm. *Wind Energy*, 10, 517–528.
- Bastankhah, M., Porté-Agel, F. (2014). A new analytical model for wind-turbine wakes. *Renewable Energy*, 70, 116-123.
- Basu, S., Porté-Agel, F. (2006). Large-Eddy Simulation of Stably Stratified Atmospheric Boundary Layer Turbulence: A Scale-Dependent Dynamic Modeling Approach. *Journal of the Atmospheric Sciences*, 63, 2074-2090.
- Bhattacharyya, S. C., Timilsina, G. R. (2009). Energy demand models for policy formulation: A comparative study of energy demand models. Policy Research Working Paper 4866, The World Bank.
- Burton, T., Shape, D., Jenkins, N., Bossanyi, N. (2001). *Wind Energy Handbook*. Wiley.
- Carsewell, A.I. LIDAR measurements of the atmosphere. *Can. J. Phys.* 1983, 61, 378-393.
- Çengel, Y. A., Cimbala, J. M. (2006). *Fluid mechanics: Fundamentals and applications*. McGraw-Hill Higher Education, 2nd Ed, Boston, USA.

- Chehouri, A., Llinca, A, Perron, J., Younes, R. (2015). Review of Performance Optimization Techniques Applied to Wind Turbines. *Applied Energy*. 142, 361-388.
- Clive, P.J.M. (2011) Remote sensing standards: their current status and significance for offshore projects, EWEC.
- Clive, P.J.M. (2012). Remote Sensing Best Practice. European Wind Energy Offshore Conference. Copenhagen, DK.
- Clive, P.J.M. (2016). Offshore Power Performance Assessment for Onshore Costs. SgurrEnergy. Available in: <http://www.sgurrenergy.com/wp/wp-content/uploads/2016/05/Offshore-Power-Performance-Assessment-using-LiDAR1.pdf> . Accessed in: 01/02/2017.
- Crespo, A., Hernández, J., Frandsen, S. (1999). Survey of modelling methods for wind turbine wakes and wind farms. *Wind Energy* 2, 1–24.
- EWTSII, European Wind Turbine Standards II (1999). J.W.M. Dekker and J.T.G. Pierik, editors.
- Ferziger, J. H., Peric, M. (2001). *Computational Methods for Fluid Dynamics*. Springer-Verlag. 3rd , XIV, 426.
- Fox, R. W., McDonald, A. T., Pritchard, P.J. (2004). *Introduction to Fluid Mechanics*, 6th ed. United States: John Wiley & Sons, Inc.
- Frandsen, S. (1992). On the wind speed reduction in the center of large clusters of wind turbines. *J Wind Eng Ind Aerodyn*. 39, pp.251–265.
- Frandsen, S. Barthelmie, R., Pryor, S., Rathmann, O., Larsen, S., Hojstrup, J. (2006). Analytical modelling of wind speed deficit in large offshore wind farms. *Wind Energy*, 9(1-2), pp.39–53.
- Gottschall, J., Peinke, J. (2008). How to Improve the Estimation of Power Curves for Wind Turbines. *Environmental Research Letters*. 3, 1-7.
- GWEC, Global Wind Energy Council. (2014). *Global Wind Energy Outlook 2014*. Brussels, BE. Available in: < http://www.gwec.net/wp-content/uploads/2014/10/GWEO2014_WEB.pdf > accessed in 13/09/2015.
- Honrubia, A., Viguera-Rodríguez, A., Gómez , E., Rodríguez-Sánchez, D. (2009). The Influence of Wind Shear in Wind Turbine Power Estimation. *Proceeding of EWEA2009*, Stockholm.
- IEC - International Electrotechnical Commission - 61400-12-1. (2005). *Wind turbine – Part 12-1: Power performance measurements of electricity producing wind turbines*.

- Janssen, J. (2012). Development of a wind farm power forecast model. Master of Science Thesis. Sustainable Energy Technology. Eindhoven University of Technology, Netherlands.
- Jensen, N.O. (1983). A note on wind generator interaction. Risø-M-2411 Risø National Laboratory Roskilde, pp.1–16.
- Kaiser, K., Langreder, W., Hohlen, H., Højstrup, J. (2007). Turbulence Correction for Power Curves. In Wind Energy Proceedings of Euromech Colloquium. pp. 159–162.
- Katic, I., Højstrup, J., Jensen, N. (1986). A simple model for cluster efficiency. In: Proceedings of the European wind energy association conference and exhibition, Rome, Italy 1986. pp. 407-409.
- Kim, D., Kim, T., Oh, G., Huh, J., Ko, K. (2016). A comparison of ground-based LiDAR and met mast wind measurements for wind resource assessment over various terrain conditions. J Wind Eng Ind Aerodyn, 158, 109–121.
- Kim, S., Joo, Y., Kim, K., Shin, H. (2015). A Study of the Wake effects on the Wind Characteristics and Fatigue Loads for the Turbine in a Wind Farm. Renewable Energy. 74, 536-543.
- Kiranoudis, C. T., Maroulis, Z. B. (1997). Effective short-cut modelling of wind park efficiency. Renewable Energy, 11:439-457.
- Kress, C., Barber, S., Chokani, N., Abhari, R. S. (2012). A new kinematic model for improved modelling of wakes. In: Proceedings of the German Wind Energy Conference DEWEK. Bremen, Germany.
- Kumer, V-M., Reuder, J., Dörninger, M., Zauner, R., Grubišić, V. (2016). Turbulent kinetic energy estimates from profiling wind LiDAR measurements and their potential for wind energy applications. Renew Energy, 99, 898–910.
- Langreder, W., Hohlen, H., Højstrup, J., Kaiser, K. (2004). Turbulence Correction for Power. European Wind Energy Conference. London, UK.
- Larsen, G. C., Højstrup, J., & Aagaard Madsen, H. (1996). Wind fields in wakes. In A. Zervos, H. Ehmann, & P. Helm (Eds.), 1996 European Union wind energy conference. Proceedings. pp. 764-768.
- Larsen, G.C. (1988). A Simple Wake Calculation Procedure. , pp.1–53.
- Launder, B.E., Spalding, D.B., (1974). The numerical computation of turbulent flows. Computer Methods in Applied Mechanics and Engineering, 3(2), pp.269–289.

- Leishman, J. G. (2002). Challenges in Modelling the Unsteady Aerodynamics of Wind Turbines. 21st ASME Wind Energy Symposium and the 40th AIAA Aerospace Sciences Meeting, Reno, NV.
- Leung, D.Y.C., Yang, Y. (2012). Wind Energy Development and its Environmental Impact: A Review. *Renewable and Sustainable Energy Reviews*. 16, 1031-1039.
- Malavasi, S., Gianandrea, M., Umberto, F., Alessandro, P. (2012). On the pressure losses through perforated plates. *Flow Measurement and Instrumentation*, 28 ,57–66.
- Manwell, J., McGowan, J., Rodgers A. L. (2009). *Wind Energy Explained-Theory, Design and Application*. John Wiley & Sons. Chichester, UK.
- McLaughlin, D., (2012). *Wind Shear and its Effect on Wind Turbine Noise Assessment*. Glasgow (United Kingdom), Sgurr Energy.
- Mo, J.O., Choudhry, A., Arjomandi, M., Kelso, R., Lee, Y.H. (2013). Effects of wind speed changes on wake instability of a wind turbine in a virtual wind tunnel using large eddy simulation. *Journal of Wind Engineering and Industrial Aerodynamics* 117, 38-56.
- Moore, K.E. (2010) Recommended practices to achieve bankable data from SODAR, AWEA Wind Resource Assessment Workshop.
- Nedjari, H. D., Guerri, O., Saighi, M. (2017). CFD wind turbines wake assessment in complex topography. *Energy Conversion and Management*, 138, 224–236.
- Özahi, E. (2015). An analysis on the pressure loss through perforated plates at moderate Reynolds numbers in turbulent flow regime. *Flow Measurement and Instrumentation*, 43, 6–13.
- Peña, A., Rathmann, O. (2014). Atmospheric stability-dependent infinite wind-farm models and the wake-decay coefficient. , pp.1269–1285.
- Politis, E. S., Prospathopoulos, J., Cabezon, D., Hansen, K. S., Chaviaropoulos, P. K., & Barthelmie, R. J. (2015). Modelling wake effects in large wind farms in complex terrain: the problem, the methods and the issues. *Wind Energy*, 15, 161-182.
- Pope, S. B. (2001). *Turbulent Flows*. Cambridge University Press: Cambridge, UK.
- Prospathopoulos, J. M., Politis, E. S., Chaviaropoulos, P. K., Rados, K. G., Schepers, J. G., Cabezón, D., Hansen, K., Barthelmie, R.J. (2010). CFD modelling of wind farms in complex terrain. In: *EWEC 2010*, Warsaw, Poland.

- Prospathopoulos, J. M., Politis, E. S., Rados, K. G., Chaviaropoulos, P. K. (2011). Evaluation of the effects of turbulence model enhancements on wind turbine wake predictions. *Wind Energy*, v. 14, n. 2, p. 285–300.
- Rapaka, N. R., Sarkar, S. (2016) An immersed boundary method for direct and large eddy simulation of stratified flows in complex geometry. *Journal of Computational Physics*, 322, 511–534.
- Rehman, S., Al-Abbadi, N. M. (2005). Wind Shear Coefficients and their effect on Energy Production. *Energy Conversion and Management*, v. 46(15-16), p. 2578-2591.
- Renkema, D. J., (2007). Validation of Wind Turbine Wake Models. Master of Science Thesis. Faculty of Aerospace Engineering. Delft University of Technology, Netherlands.
- Réthoré, P-E. M. (2009). Wind Turbine Wake in Atmospheric Turbulence. Roskilde: Risø National Laboratory for Sustainable Energy. (Risø-PhD; No. 53(EN)).
- Rohatgi, J., Barbezier, G. (1999). Wind Turbulence and Atmospheric Stability – Their Effect on Wind Turbine Output. *Renewable Energy*, 16, 908-911.
- Roy, S. B., Sharp, J. (2013). Why Atmospheric Stability Matters in Wind Assessment. *North American Wind Power*, Vol. 9, 12.
- Sanderse, B. (2009). Aerodynamics of wind turbine wakes. Technical Report, ECN-E- 09-016.
- Sanderse, B., van der Pijl, S. P., Koren, B. (2011). Review of computational fluid dynamics for wind turbine wake aerodynamics. *Wind Energy*, 14, 799-819.
- Sathe, A., Mann, J., Barlas, T., Bierbooms, W. A. A. M., van Bussel, G. J. W. (2013). Influence of Atmospheric Stability on Wind Turbine Loads. *Wind Energy*, DOI: 10.1002/we.1528.
- Sathe, A., Mann, J., Gottschall, J., Courtney, M. S. (2011). Can Wind LiDARs Measure Turbulence? *Journal of Atmospheric and Oceanic Technology*. 28 (7), 853-868.
- SgurrEnergy (2012). Investigation of Wakes using 2nd Generation Wind LiDAR at Milford Wind Farm. Technical Limited Report.
- SgurrEnergy (2015). Industry Papers. Available in: < <http://www.sgurrenergy.com/about-sgurr-energy/download-centre/industry-papers/>> accessed in: 20/10/2015.
- Sheinman, Y., Rosen, A. (1992). A Dynamic Model of the Influence of Turbulence on the Power Output of a Wind Turbine. *J. Wind Eng. Ind. Aerodyn.* 39, 329-341.

- Spera, D.A. (1998). Wind Turbine Technology, Fundamental Concepts of Wind Turbine Engineering. ASME Press, USA, (May), pp.1–46.
- Sumner, J., Watters, C. S., Masson, C. (2010). CFD in Wind Energy: The Virtual, Multiscale Wind Tunnel. *Energies*, 3, 989-1013.
- Troldborg, N., Sørensen, J. N., Mikkelsen, R. (2007). Actuator line simulation of wake of wind turbine operating in turbulent inflow. In *The Science of Making Torque from Wind. Journal of Physics: Conference Series*, vol. 75. Technical University of Denmark, Lyngby, Denmark.
- Tsalicoglou, C. (2012) Numerical Study of Wind Turbine Wake Aerodynamics in Uniform and Yawed Inflow. Master Thesis. Laboratory for Energy Conversion, Swiss Federal Institute of Technology (ETH) Zurich.
- VanLuvanee, D. R. (2006). Investigation of Observed and Modeled Wake Effects at Horns Rev using WindPRO. Master Thesis in Wind Energy. Technical University of Denmark, Denmark.
- Vermeer, L., Sørensen, J., Crespo, A. (2003). Wind Turbine Wake Aerodynamics. *Progress in Aerospace Sciences*. 39, 467–510.
- Vogt, S., Thomas, P. SODAR—A useful remote sounder to measure wind and turbulence. *J. Wind Eng. Ind. Aerodyn.* 1995, 54-55, 163-172.
- Wagner, R., Antoniou, I., Pedersen, S. M., Courtney, M. S., Jørgensen, H. E. (2009). The influence of the wind speed profile on wind turbine performance measurements. *Wind Energy*, 12, 348- 362.
- Wandinger, U. Introduction to Lidar. In *Lidar: Range-Resolved Optical Remote Sensing of the Atmosphere*; Weitkamp, C., Ed.; Springer: New York, NY, USA, 2005; pp. 6-11.
- Wang H., Barthelmie R. J., Pryor S. C., Brown G. (2016). LiDAR arc scan uncertainty reduction through scanning geometry optimization. *Atmos. Meas. Tech.*, 9, 1653 – 1669.
- Werner, C. Doppler Wind Lidar. In *Lidar: Range-Resolved Optical Remote Sensing of the Atmosphere*; Weitkamp, C., Ed.; Springer: New York, NY, USA, 2005; pp. 326-354.
- Wharton, S., Lundquist, J. K. (2010). Assessing atmospheric stability and its impacts on wind characteristics at an onshore wind farm. 19th Symposium on Boundary Layers and Turbulence Keystone, CO, United States.
- Wharton, S., Lundquist, J. K. (2012). Atmospheric stability affects wind turbine power collection. *Environmental Research Letters*, 7, 014005.
- WMO, World Meteorological Organization, 2008. Guide to Meteorological Instruments and Methods of Observation, No. 8 pp. 1.5-12.

Wu, Y., Port'e-Agel, F. (2012). Atmospheric Turbulence Effects on Wind-Turbine Wakes: An LES Study. *Energies*. 5, 5340-5362.

Yildirim, B., Sun Lin, S., Mathur, S., Murthy, J. Y. (2013) A parallel implementation of fluid–solid interaction solver using an immersed boundary method. *Comput. Fluids*, 86, 251-274.